Measurement of Charge Asymmetry in Top Quark Pair Production at the Large Hadron Collider

by

Burton Andrew Betchart

Submitted in Partial Fulfillment

of the

Requirements for the Degree

Doctor of Philosophy

Supervised by

Professor Regina Demina

Department of Physics and Astronomy
Arts, Sciences and Engineering
School of Arts and Sciences

University of Rochester
Rochester, New York

2013

Biographical Sketch

The author was born in Denver, Colorado. He attended Oberlin College, and graduated with a Bachelor of Arts degree in Physics, achieving the distinction of High Honors. He taught high school physics at Colegio Menor San Francisco de Quito, in Quito, Ecuador for two years subsequently. He began doctoral studies in Physics at the University of Rochester in 2006. He joined the group of Professor Regina Demina in 2007 to pursue his research in High Energy Physics under her direction. He received the Master of Arts degree in Physics from the University of Rochester in 2008, and relocated to the European Center for Nuclear Research (CERN) near Geneva, Switzerland, to continue his research as a member of the CMS collaboration. He returned to Rochester in 2010.

The following publications result from work conducted during doctoral study:

1. Burton A. Betchart, Regina Demina, and Amnon Harel. "Analytic solutions for neutrino momenta in decay of top quarks". In: *Nucl.Instrum.Meth* 736.0 (2014), pp. 169 –178. ISSN: 0168-9002. DOI: `10.1016/j.nima.2013.10.039`.

2. T. Maenpaa et al. "Silicon beam telescope for LHC upgrade tests". In: *Nucl.Instrum.Meth.* A593 (2008), pp. 523–529. DOI: `10.1016/j.nima.2008.05.012`

3. P. Luukka et al. “TCT and test beam results of irradiated magnetic Czochralski silicon (MCz-Si) detectors”. In: *Nucl.Instrum.Meth.* A604 (2009), pp. 254–257. DOI: 10.1016/j.nima.2009.01.071

4. Serguei Chatrchyan et al. “Search for Supersymmetry at the LHC in Events with Jets and Missing Transverse Energy”. In: *Phys.Rev.Lett.* 107 (2011), p. 221804. DOI: 10.1103/PhysRevLett.107.221804. arXiv: 1109.2352 [hep-ex]

5. Vardan Khachatryan et al. “Search for Supersymmetry in pp Collisions at 7 TeV in Events with Jets and Missing Transverse Energy”. In: *Phys.Lett.* B698 (2011), pp. 196–218. DOI: 10.1016/j.physletb.2011.03.021. arXiv: 1101.1628 [hep-ex]

Acknowledgments

I would like to acknowledge the many kind individuals who have invested significant professional and emotional resources to help me to complete this work. I convey my deepest gratitude to my advisor Regina Demina, for training me in research methods, for ensuring I had every opportunity to succeed, and for allowing me to choose my path. My thanks are also extended to Amnon Harel for his readiness to engage in details and to offer constructive criticism. It has been my pleasure to collaborate with Edward Laird, whose great enthusiasm and skill are matched by his impartiality in evaluating solutions. I am grateful for the many colleagues who have shared the experience and effort of these years with me, among them Douglas Orbaker, Daniel Miner, Sergey Korjinevski, Yuri Gotra, Henning Flaecher, and Roberto Covarelli. I would also like to recognize the wider LHC and CMS collaborations for their extensive long term efforts, and congratulate them on the excellent performance of the machine and the detector. The support of my family has been invaluable in the journey to complete my doctoral studies. I would like to thank my parents for their endless love and encouragement, as well as my brother, grandparents, and extended family in the United States and Ecuador. Lastly, I would like to express my love and appreciation for my wife Paola Betchart, whose unfailing patience and love have made setbacks softer and successes sweeter.

Burton A. Betchart
University of Rochester
October 2013

Abstract

We present a measurement of charge asymmetry in the production of top and antitop quark pairs in proton-proton collisions, in a sample of $19.6\,\mathrm{fb}^{-1}$ of data collected by the CMS experiment at 8 TeV center of mass energy in 2012. Selected events have a single isolated electron or muon, and at least four jets, at least one of which is likely due to a bottom quark. A template technique is employed to measure top-antitop asymmetry in two kinematic observables simultaneously, which allows attribution of contributions to the observed forward-central asymmetry from distinct Standard Model production mechanisms. An asymmetry $A_c^y = (0.15 \pm 0.42)\%$ is measured in the difference of absolute rapidities of top-antitop pairs, of which $(0.00 \pm 0.43)\%$ is attributable to quark-antiquark initial states, and $(0.18 \pm 0.15)\%$ is attributable to quark-gluon initial states. The first measurement of the transverse top quark charge asymmetry is also presented, with the result $A_c^\phi = (0.44 \pm 0.50)\%$. Measurements of the inclusive asymmetry on selections with high and low top system mass and absolute rapidity are consistent with the main result. The results are compared to Standard Model predictions and measurements from the LHC and the Tevatron.

Contributors and Funding Sources

This work was supervised by a dissertation committee consisting of Professors Regina Demina (advisor), Aran Garcia-Bellido, and Lynne Orr of the Department of Physics and Astronomy, and Professor Miguel Alonso of the Institute of Optics. A variety of problems related to high energy physics analysis were solved in collaboration with Edward Laird, which led to the development of the `supy` tool set used extensively in analysis for this work. Amnon Harel, Peter Skands, and Efe Yazgan each provided valuable insight and feedback during numerous discussions, which helped to shape the design of this analysis. The author's contributions to the design, construction, commissioning, operation, and analysis infrastructure of the Large Hadron Collider (LHC) and the Compact Muon Solenoid (CMS) were a small part of the total effort of many thousands of physicists, and centered around the Silicon Strip Tracker subsystem of CMS. Several important components of the analysis where carried out by other members of the CMS Collaboration, including: luminosity measurement; trigger efficiency measurement; lepton identification and isolation efficiency measurements; jet energy scale measurement; jet resolution measurement. Event selection criteria are based on recommendations of the CMS Collaboration. All other work for the dissertation was completed by the author independently.

This work has been enabled by a wide variety of independent software projects, including: event generator and simulation packages Pythia, MadGraph, Powheg, Geant; the analysis libraries Root, RooFit, and `SciPy`; free and open source software like the GNU/Linux system and the Python programming language. Computing facilities utilized for this analysis are located at Fermi National Accelerator Laboratory (Fermilab), the European Center for Nuclear Research (CERN), Imperial College London, and other locations participating in the Worldwide LHC Computing Grid. Graduate study was supported by Department of Energy grants DE-FG02-91ER40685 and DE-SC00008475, by Department of Education grants from the Graduate Assistance in Areas of National Need (GAANN) program, and by teaching asistantships in the University of Rochester Department of Physics and Astronomy.

Table of Contents

List of Tables

List of Figures

1 The Standard Model

The modern understanding of fundamental particles and their interactions is known as the Standard Model. The development of the theory spans more than a century, beginning with breakthroughs in understanding around 1900, and concluding only presently with the likely observation of the most elusive particle included in its description. While the Standard Model provides a more precise description of natural phenomena than any other theory in history, it relies on many empirical parameters, some of which remain loosely constrained, and leaves unexplained many observations about the universe. Theoretical physicists have proposed a wealth of theories in their attempts to reduce the number of parameters necessary for a fundamental description of natural processes, and to incorporate observations which are not explained by the Standard Model. The role of the experimental physicist in the continuing pursuit of a complete description of fundamental particles is to test theories by observation, and to crosscheck the Standard Model with new observations in search of statistical tension which could signify new physics. Crosschecks of the Standard Model, which has withstood the tests of many observations, frequently involve precision measurements like the one presented in this work.

This chapter begins with a brief historical survey of the development of the Standard Model in Section 1.1. It continues in Section 1.2 with an overview of the fundamental particles, their properties, and their interactions. Sections 1.3 and 1.4 offer a more detailed discussion of the Standard Model Lagrangian density, and the procedures of predictive calculation. The chapter concludes with discussions of three topics: the internal structure of hadrons, in Section 1.5; methods of numerical calculation, in Section 1.6; and points of interest related to the top quark, in Section 1.7.

1.1 History

It is appropriate to emphasize that the Standard Model is the work of many individuals and collaborations over more than a century. This can be done by highlighting some of the important contributions to its development, without necessarily aspiring to a comprehensive history, available elsewhere [1–4].

Many new results in the early twentieth century laid the foundations of quantum mechanics. Radioactivity and the electron where discovered in quick succession in 1896 and 1897, by Becquerel and by Thomson, respectively. In 1900, Planck explained black body radiation spectra as due to many independent quantized radiators, whose ratio of energy to frequency is given by a constant h. Einstein explained the photoelectric effect in 1905 as due to quanta of light, each with energy and frequency related by Planck's constant. Perhaps even more important to the foundations of the Standard Model, Einstein also postulated special relativity in 1905. Millikan's experiments showed in 1909 that electric charge is quantized, and in 1911 Rutherford's experiments showed that atoms have internal structure, with a dense positively charged nucleus. By 1913, Bohr had developed a model which was able to predict the spectral lines of hydrogen. In his 1924 PhD thesis, de Broglie used concepts from special relativity to extend the Planck energy-frequency relationship of light to massive particles, arguing that they can exhibit wave characteristics. Wave behavior of scattering electrons consistent with de Broglie's hypothesis was observed by Davisson and Germer in 1927.

The mathematical mechanics of quantum interactions was first developed in the 1920s by Heisenberg and collaborators in Germany, and by Schrödinger in Austria. Dirac extended their work to a form compatible with the postulates of special relativity, which resulted in the prediction of the positron in 1928. Positrons were discovered in 1932 by Anderson, who observed the tracks that cosmic rays deposited on photographic plates in a magnetic field. The existence of the neutrino was proposed in 1930 by Pauli, based on the hypothesis of conservation of energy, momentum, and angular momentum in beta decay. After the discovery of the neutron in 1932 by Chadwick, Pauli's idea became the basis for Fermi's theory of the weak interaction. In 1955, neutrinos were definitively detected by Reines and collaborators.

The quantum field theory of electromagnetic interactions was pioneered by Dirac and others in the 1930s, but problems with divergent series in their calculations stalled the advancement. A scheme for overcoming divergent calculations was proposed by Bethe in 1947, which allowed progress to continue on the development of a complete theory of quantum electrodynamics; Tomonaga, Schwinger, and Feynman were awarded the Nobel prize in 1965 for their contributions. The concepts of gauge invariance in quantum electrodynamics were generalized by Yang and Mills in the 1950s to larger symmetry groups [5], which later became the basis for theories of the weak and strong interactions.

The quark model of strong interactions was developed in the early 1960s by Gell-Mann and collaborators to explain the underlying order in the proliferation of particles observed in cosmic rays [6, 7]. The theory predicted the existence of a previously unobserved particle, which was later discovered by a particle accelerator collaboration at Brookhaven National Laboratory [8]. The formalization of quantum chromodynamics, the gauge theory of the strong force, was completed in 1975, with contributions from Politzer, Gross, Wilczek, Gell-Mann and others

[9–13].

A mechanism for generating massive gauge bosons via spontaneous symmetry breaking in Yang-Mills theories was published in 1964 by three independent groups: Brout and Englert [14]; Higgs [15]; and Guralnik, Hagen, and Kibble [16]. In 1967 this mechanism was incorporated independently by Weinberg [17] and Salam [18] with earlier work by Glashow [19] on a unified theory of electromagnetic and weak interactions. The electroweak theory predicted precise masses for the W and Z gauge bosons responsible for the weak interactions, and postulated an additional scalar boson H^0. The electroweak gauge bosons were confirmed to exist in 1983 by experimental collaborations at the European Center for Nuclear Research (CERN), through observations of high energy proton-antiproton collisions of the Super Proton Synchrotron [20, 21].

In the years since the discovery of W and Z, experiments at colliding beam accelerators have dominated particle discovery and precision tests of the Standard Model. The bottom and top quarks were discovered at Fermi National Laboratory [22–24], and the number of particle generations was confirmed to be three by precision measurements of the Z decay width at the Large Electron–Positron collider at CERN [25, 26]. A scalar boson consistent with H^0 has only recently been discovered, in proton-proton collisions at the Large Hadron Collider at CERN [27, 28].

The development of the Standard Model has been characterized by the interplay of new experimental results with new theoretical ideas. Despite the success of the Standard Model, there are many observations which remain unexplained. It seems reasonable to hope that further mechanisms can be discovered, which will explain the abundance of matter relative to antimatter, the nature of dark matter which affects the rotations of galaxies, and the periodicity and multiplicity of the generations of matter, to mention several. Future developments will continue to rely on exchanges between experiment and theory, each in support of the other.

1.2 Overview

The matter of our everyday experience consists of electrons (e^-), protons (p), and neutrons (n), mostly configured as atoms held together by the electromagnetic force. The interaction strength of these particles with the electromagnetic force is proportional to their electric charges, which are -1, +1, and zero for the electron, proton, and neutron, respectively, in units of the elementary charge $e = 1.6 \cdot 10^{-19}$ C. Measurements of the electron show no discernable substructure, and indicate that its radius must be smaller than 10^{-22} m [29], so it is modeled as a point particle and called elementary. Protons and neutrons are composite particles since they have a substructure of quarks, which are considered to be elementary point particles like the electron. The proton gets its net electric charge of +1 from two up quarks (u), each with an electric charge of +2/3, and one down quark (d), with an electric charge of of -1/3. The neutron gets its net electric charge of zero from two down quarks and one up quark.

Such composite particles with quark substructure are known as hadrons, and are held together by the strong force. The strong charge carried by quarks is more complicated than electric charge because it comes in three kinds, or colors, rather than one, but the total strong charge carried by every hadron is zero. Residual effects of the strong force are responsible for binding protons and neutrons together to make atomic nuclei, which would otherwise disintegrate under the influence of the repulsive electromagnetic forces of the positively charged protons.

Elementary particles like the electron which do not participate in the strong force are known as leptons. The electron neutrino (ν_e) is another type of lepton, which lacks electromagnetic charge in addition to lacking strong charge, so we experience it less commonly and less directly. An example of a reaction involving neutrinos is the spontaneous decay of a neutron to a proton, an electron, and an electron neutrino, which is mediated by the weak force. Weak charge (weak isospin) is carried by left-chiral particles, but not by their mirror images, which are right-chiral. Left-chiral versions of the electron, electron neutrino, down quark, and up quark have weak isospin of -1/2, +1/2, -1/2, and +1/2, respectively. These four elementary particles each have mass, the charge of the gravitational force, although the mass of the neutrino is vanishingly small, and the mass eigenstates are not quite the same as the weak isospin eigenstates.

Each of these four particles is also a fermion, which means it has half integer intrinsic angular momentum (spin, in units of $\hbar = h/2\pi$) along any axis of measurement, obeys the Pauli exclusion principle, and follows Fermi-Dirac statistics when grouped with identical particles. Particles with integer spin are called bosons, do not obey the Pauli exclusion principle, and follow Bose-Einstein statistics when grouped with identical particles. The mediating particles of the four fundamental forces are all bosons. The electromagnetic force is mediated by the photon (γ), which has spin 1, no mass, and no charge. The strong force is mediated by eight gluons (g), which carry spin 1, two colors of strong charge, and no mass. The weak force is mediated by the Z, W^+, and W^- bosons, which all have mass, spin 1, and respectively carry 0, +1, and -1 electromagnetic charge and 0, +1, and -1 weak isospin. The gravitational force is thought to be mediated by the graviton, which would have spin 2 and no mass, but a description of gravitation is not included in the Standard Model. Since the photon and graviton are massless and do not themselves carry the charge to which they couple, they can be exchanged over arbitrarily large distances; electromagnetism and gravity have infinite range. Since the Z and W have mass around $m = 80\,\mathrm{GeV/c^2}$ [30], virtual particles which carry the weak force are limited by the Heisenberg uncertainty principle to lifetimes on the order of $\Delta t = \hbar/2m \approx 5 \times 10^{-27}\,\mathrm{s}$, and the range of the weak force is consequently limited to approximately $c\Delta t = 10^{-18}\,\mathrm{m}$. Gluons are confined to within hadrons since they carry color charge and consequently couple to each other. Residual effects of the strong force act to create an attractive

Yukawa potential among protons and neutrons through exchange of intermediate massive spin 1 hadrons (π). One additional fundamental boson (H^0) is introduced into the Standard Model by the mechanism which allows particles to be massive without destroying symmetries of the weak interaction. This boson has spin zero and is massive, but is without electromagnetic, weak, or strong charge.

For every elementary particle type there is a corresponding elementary particle type with some quantum numbers identical, like mass and spin, and others inverted, like electromagnetic charge. For example, the charge conjugate, or anti-particle, of the electron is the positron (e^+). Those of the electron neutrino, and down and up quarks, are the electron anti-neutrino ($\bar{\nu}_e$), and the anti-down ($\bar{\mathrm{d}}$) and anti-up ($\bar{\mathrm{u}}$) quarks, respectively. Some elementary particles with no charge, like the photon, Z, and H^0, are their own anti-particles. It may be the case that neutrinos are their own antiparticles. A particle and its anti-particle can annihilate upon meeting at a point in space-time, and create new groups of particles like a different particle-antiparticle pair. The electromagnetic and strong forces are both symmetric under charge conjugation ($\mathcal{C}$), which means that the dynamics of those forces are unchanged by swapping every particle for its anti-particle. Since the weak force couples only to left-chiral particles and right-chiral anti-particles, and since chirality is invariant under charge conjugation, the weak force is not charge symmetric. However, chirality is inverted under parity ($\mathcal{P}$), the mirror image of the system, and the weak force is nearly $\mathcal{CP}$-symmetric. One of the most pressing unexplained observations in physics is that, while matter and anti-matter are expected to have been created in equal amounts, anti-matter is mostly absent from the universe today, while matter abounds. The Standard Model mechanisms for $\mathcal{CP}$ violation cannot account for the disparity.

The electron, electron neutrino, down quark, and up quark, along with their anti-particles, comprise the first generation of fermions. There are three generations, the next two each consisting of analogous particles to the first generation, with identical quantum numbers except with consecutively greater masses. The analogs of the electron, down quark, and up quark in the second (third) generation are the muon (tau), strange (bottom) quark, and charm (top) quark, symbolized by μ (τ), s (b), and c (t) [30]. Since the particle mass eigenstates are quantum superpositions of the weak isospin eigenstates, the weak interaction provides a mechanism for particles to transform from one generation to another. In particular, second and third generation particles are unstable and decay weakly to lower mass first generation particles, with the exception of neutrinos, which seem to oscillate among generations [31–33].

1.3 Lagrangian Density

A description of Standard Model electromagnetic interactions can be generated by requiring the free Dirac fermion Lagrangian density to be invariant to adjustment of the wave-function by a locally independent phase $\theta(x)$ [34], such that $\psi(x) \to \psi'(x) = e^{iQ\theta(x)}\psi(x)$, which is also known as a gauge transformation in the symmetry group $U(1)_Q$. The necessary addition to the Lagrangian density in order to ensure local $U(1)_Q$ gauge invariance is a spin 1 field which couples with the Dirac fermion field. An additional term can be added to the Lagrangian density to describe propagation of momentum and energy via this spin 1 field, without breaking local gauge invariance. The resulting Lagrangian density describes the interactions of photons and Dirac fermions in a way which is explicitly calculable. Local $U(1)_Q$ gauge invariance is a continuous symmetry, and the associated conserved quantity Q ensured by Nöether's Theorem is consistent with electromagnetic charge.

A similar strategy can be followed to generate a description of strong interactions in the Standard Model. In order for the Lagrangian density of a free quark field with triplet (color) charge to be invariant under local gauge transformations in the symmetry group $SU(3)_C$, another spin 1 field must be incorporated, with the same terms as the electromagnetic force, plus additional terms due to the non-commutation of the eight $SU(3)_C$ generators. The resulting Lagrangian density describes the interactions of gluons and quarks. The additional terms, not included in the analogous electromagnetic Lagrangian density, describe interactions of three gluons, and of four gluons. Gluons couple to each other because they carry color charge, which is notably different than photons, which do not carry electromagnetic charge. The non-commutation of the $SU(3)_C$ generators also restricts strong coupling strength to a single value α_s for all interactions, in contrast to the arbitrary coupling strength of the electromagnetic force.

Local gauge invariance is not compatible with mass terms for the boson fields in the Lagrangian density, which is unproblematic for the massless photons and gluons of the electromagnetic and strong forces. A description of weak interactions generated by analogous imposition of local gauge invariance to rotations in weak isospin space, described by $SU(2)_L$, leads to an unrealistic theory with massless mediating bosons. Furthermore, fermions in such a theory of weak interactions must also be unrealistically massless in order to preserve the chiral structure. Both problems are resolved by requiring local gauge invariance for the larger symmetry group $SU(2)_L \otimes U(1)_Y$, while including a gauge invariant term in the Lagrangian density for a doublet of complex scalar fields, one of which has a vacuum expectation value. The resulting $SU(2)_L$ singlet field has different couplings to left- and right-chiral fermions, so it cannot represent the achiral photon field, and Y is not electromagnetic charge. The singlet field is orthogonal to the neutral component of the $SU(2)_L$ triplet field, and since both are neutral they can be projected into a different basis where one field, the photon, is achiral, and the orthogonal field is the Z. The charged components of the $SU(2)_L$ triplet describe the $\mathrm{W}^{\pm}$ fields. The complex scalar field with the vacuum expectation value gives rise to a continuum of degenerate minimum energy states. While the potential is gauge symmetric, the ground state of the system relaxes asymmetrically to just one of the possible minima, a result known as spontaneous symmetry breaking. As a result of spontaneous symmetry breaking, mass-like terms for the W and Z fields appear in the Lagrangian density, and the only physically apparent symmetry remaining is $U(1)_Q$. Three of the four degrees of freedom in the doublet of complex scalar fields can be parametrized as rotations in $SU(2)_L$, which are arbitrary due to the local gauge invariance. The only physically meaningful degree of freedom in the doublet of complex scalar fields manifests as a single real scalar field, which corresponds to the particle H^0. The Lagrangian density includes terms for coupling one or two H^0 particles with two Z or a $W^{\pm}$ pair, as well as a H^0 mass term. Spontaneous symmetry breaking also provides a mechanism for adding mass-like terms for fermions to the Lagrangian density by coupling left- and right-chiral fields via the complex scalar doublet, which preserves the chiral properties of the theory. If such mass terms are added, the H^0 also couples to particle-antiparticle fermion pairs.

To summarize, the Standard Model consists of fermionic and bosonic fields, the interactions of which are described by a Lagrangian density which is locally gauge symmetric in the space $SU(3)_C \otimes SU(2)_L \otimes U(1)_Y$. Masses are incorporated into the theory by the spontaneous symmetry breaking mechanism, which results in the physically apparent symmetry $SU(3)_C \otimes U(1)_Q$.

1.4 Calculations

The probability of a system to undergo a transition can in principle be calculated from the initial and final states, and the Lagrangian density $\mathcal{L}$ describing the system. In the path integral formulation of quantum field theory [35], the probability of a transition is proportional to $|\mathcal{M}_{if}|^2$, where the matrix element $\mathcal{M}_{if}$ is a sum of contributions from each possible pathway of the transition. The contribution of a particular path P to the matrix element is given by $\exp\{\frac{i}{\hbar}\int \mathcal{L}\mathrm{d}x\}$, where the integral is taken along P between initial and final states. The exponentiated integral can be written as a series expansion in successively higher powers of the action. It is often the case that the series is convergent and can be well-ordered into groups of terms which contribute successively less to the total matrix element. In such cases it can be convenient to approximate the full matrix element by the most significant groups of terms in the ordering.

Individual terms in the expansion of the matrix element can more easily be communicated pictorially than algebraically, with what are known as Feynman diagrams [36]. Multiplicative factors of an individual term are explicitly associated to graphical elements of its associated Feynman diagram. Every interaction term in the Lagrangian density can be drawn as a vertex joining line segments which represent the associated fields, with straight lines representing fermion fields and wavy lines representing boson fields. Lines segments which join with only one vertex represent initial state or final state fields. A line represents the field when its arrow points toward a vertex, and the conjugate field when it points away from a vertex. The remaining fields, which join two vertices, are known as propagators, and are not physically observable. Feynman diagram representing the leading order terms of electron-positron scattering are shown in Figure 1.1.

Scattering processes, in which initial state particles converge on a point and transition to any of a large continuum of divergent final state particles, are particularly relevant to the discussion of experiments which probe the Standard Model. The scattering rate is the product of the instantaneous luminosity, or effective flux of incident particles, and the cross section (σ), or effective area of the colliding particles. The transition rate to a particular final state is proportional to the absolute square of the matrix element of the transition and to the density of final states available to a particular final state particle, which is known as Fermi's Second Golden Rule. Differential cross sections for scattering processes can be

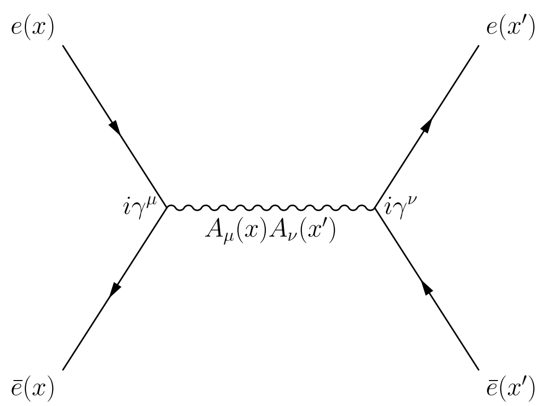

Figure 1.1: Feynman diagram for the matrix element term $\bar{e}(x)\gamma^\mu e(x)\bar{e}(x')\gamma^\nu e(x')A_\mu(x)A_\nu(x')$, in electron-positron s-channel scattering. An electron field, $e(x)$, and a positron field, $\bar{e}(x')$, are incident from the left before interacting with the photon field $A_\mu(x)$, which propagates from x to x' before decaying from $A_\nu(x')$ to the scattered electron and positron fields $e(x')$ and $\bar{e}(x')$. The diagram is a valid representation of other processes when read with a different time sense. For example, with initial states at the bottom and final states at the top, the diagram represents electron-positron scattering in the t-channel.

calculated from the density of final states and the matrix element. For two initial state particles a and b scattering to two final state particles c and d in the center of momentum reference frame, the differential cross section per solid angle $\mathrm{d}\Omega$ of one of the final state particles is

$$\frac{\mathrm{d}\sigma}{\mathrm{d}\Omega}(a+b \to c+d) = \frac{1}{4\pi^2} \left|\mathcal{M}_{if}\right|^2 \left[\frac{E_a E_b E_c E_d}{(\hbar c)^4 (E_a + E_b)^2}\right] \left(\frac{p_f}{p_i}\right) \left(\frac{g_f}{g_i}\right). \tag{1.1}$$

where p_i (p_f) is the momentum magnitude of initial (final) state particles, E_k is the energy of particle k, and g_i (g_f) is the initial (final) state spin phase space factor [37, 38]. The total cross section for a process can be found by integrating $\mathrm{d}\sigma/\mathrm{d}\Omega$ over angular coordinates.

1.5 Hadron Substructure

At low energies, hadrons behave like single particles, with localized charge and mass, and scatter incident particles according to Equation 1.1. Unlike the leptons they have a measurable finite volume; the proton's charge radius for example is approximately 10^{-15} m. Scattering at higher energy corresponds to a reduced de Broglie wavelength of the probe particle, allowing hadron structure to be probed with greater resolution. Experiments colliding high energy electrons, muons, or neutrinos with protons or other hadrons, for example at the Stanford Linear Accelerator, reveal a substructure consistent with the quark model. While the net electromagnetic charge and spin of a hadron are properties fixed by two quarks (meson) or three quarks (baryon), the bulk of the hadron's mass is due to the binding energy of the strong force, transmitted among the quarks by many transient gluons which can themselves transiently split to quark-antiquark pairs. The quarks within a hadron which are unpaired to a charge conjugate quark and fix the hadron's charge and spin are known as 'valence' quarks, but it is not useful to distinguish which particular quarks in the 'sea' are valence quarks, since all are transient. The structure of hadrons is recursive and fractal, with each quark radiating virtual gluons which communicate its color charge, and each gluon splitting to quark-antiquark pairs on small enough scales of time and distance. Collectively, the constituent gluons, quarks, and anti-quarks of a hadron are called ‘partons’.

When a parton is scattered from within a hadron in a high energy collision, the internal structure of the hadron is pulled out with it. As pieces of this structure spread out in space, the strong force rebinds neighboring elements into new color-neutral hadrons, all of which are correlated in direction, forming what is known as a jet. This process of hadronization by the strong force is akin to the process by which surface tension breaks a divergent flow of liquid into successively smaller drops, until the surface tension overcomes the divergence at a characteristic size.

In high energy collisions of hadrons, partons of one hadron can scatter with those of the other. Calculations of cross-sections for hadron-hadron collisions must take into account the density of initial states as well as the density of final states. Initial state densities are typically quantified with parton density (or distribution) functions (PDFs), each of which describes the expectation value of the number of a particular parton type within the hadron, at a particular resolution scale, carrying a particular fraction of the total hadron longitudinal momentum. The PDFs are determined experimentally for a variety of resolution scales by scattering of various types of particles at various energies, and these data points constrain the PDFs at unprobed resolution scales. Since gluons are massless, their expected number diverges in the limit as the momentum fraction approaches zero. Non-valence-type quark PDFs usually have a single mode at zero momentum fraction, while valence-type quarks PDFs have a mode at a non-zero momentum fraction.

1.6 Numerical Methods

The calculations discussed in Section 1.4 can involve integrations over many dimensions in phase space. Even when analytic solutions are not available, numerical methods often yield useful results. One of the most efficient and general techniques for performing numerical integrations in high-dimensional phase space is the Monte Carlo method, which relies on random numbers to probabilistically sample the phase space [39]. According to the problem, each sampled point in phase space contributes a deterministic amount to the result, the precision of which increases with the sample size. For example, the area of the unit circle which falls within the unit square can be found with a Monte Carlo calculation: for N pairs of random numbers (x, y), each on the interval $[0, 1]$, some number N_{in} fall within the unit circle, $x^2 + y^2 < 1$, and the area is given by N_{in}/N with a relative precision of $1/\sqrt{N_{in}}$.

The Monte Carlo method is suitable for calculations of differential cross sections. In particular, calculations of high energy hadron scattering involve high-dimensional integrals over initial and final state phase space with complicated dependence between them and on the parton density functions. Conveniently, Monte Carlo calculations are naturally event based and statistics limited in exactly the same way as the measurements of counting experiments, including observations of scattering probability. The parallel between Monte Carlo calculations and statistical measurements of repeated experimentation suggests the further use of similar numerical techniques to simulate detector effects, such as acceptance, efficiency, and resolution. Modern high energy scattering experiments rely on such simulations to compare calculations with observations.

The Monte Carlo method is also frequently employed in a method known as Ensemble Testing, which is a means to verify the behavior of statistical measurement models. Such methods frequently incorporate various statistics into a parametrized model, and use minimization to estimate the parameters which best describe the observations. The verification technique is to generate an ensemble of pseudo-experiments, each with statistics sampled randomly according to the probability distribution of a model of particular parameter values. Each pseudo-experiment is measured as if it were data, and the properties of the aggregate results are studied for bias and the accuracy of reported uncertainty. Ensemble testing is typically performed for several likely parameter sets.

1.7 Top Quark

The top quark is the most massive of all the Standard Model fermions, with a mass of 173 GeV/c^2 [30]. For comparison, the next most massive bottom quark has a mass of only 4.2 GeV/c^2 [30]. The top quark is unstable, decaying via weak interaction to a W and a down-type quark after an extremely short lifetime of the order 10^{-24} s [30]. It is not directly observable, and is not found outside of special conditions.

In 1973, Kobayashi and Maskawa pointed out that a third generation of quarks would provide a mechanism to explain observations of broken $\mathcal{CP}$ symmetry in kaon oscillations [40], and after the discovery of the bottom quark in 1977 [22], the top quark was expected. Enough concentrated energy to produce top quark pairs was not available at any facility until the advent of Tevatron proton-antiproton collisions at Fermi National Accelerator Laboratory in 1986. Even there the cross section (~ 6 pb) and luminosity ($\sim 10^{-5}\,\mathrm{pb}^{-1}\,\mathrm{s}^{-1}$) imply a small production rate of only a few pairs per experiment per day. The top quark was discovered in 1995 by the Tevatron experiments DØ and CDF jointly, last of all the Standard Model fermions [23, 24].

Since the lifetime of the top quark is shorter than typical hadronization times, there are no hadrons with valence top quarks. For this reason, in contrast to other quark flavors, top quark properties like invariant mass and decay width can be measured from the summed energy and momenta of its decay products, without the convoluting effects of hadronization. The down-type quark in at least ninety percent of top decays is a bottom quark [30], which is statistically distinguishable from other quark flavors due to effects of its relatively long lifetime. The W boson decays to each kinematically accessible weak doublet with about the same probability [30]: three modes of charged lepton with neutrino; and 6 modes of quark pairs (first two generations, in three colors each). These possibilities result in a variety of rich signatures for the decay of top quark pairs from high energy collisions, which are typically classified into three channels according to the modes of W decay.

When both $W^{\pm}$ decay to quarks, the signature of the event is six or more jets (extra jets arising from radiated gluons or the underlying collision event), two of which are likely to exhibit characteristics of bottom quark jets. These 'all hadronic' events constitute about half of all top pair decays, but the combinatorial possibilities of Lorentz vector reconstruction are numerous, making this a difficult channel to study.

When both $W^{\pm}$ decay to leptons, the signature of the event is two jets with bottom quark characteristics, two charged leptons of opposite charge, and momentum imbalance of the debris, due to two unobserved neutrinos. These 'dilepton' events constitute about one ninth of top pair decays, but since about half of them include tau particles which themselves decay into jets difficult to distinguish from those of quarks, the dilepton channel measurements usually only include candidates with a positively charged electron or muon and a negatively charged electron or muon. This channel offers the advantages of reduced combinatorial possibilities and typically better resolution of charged lepton momenta than of jet momenta, but suffers from a relatively low branching ratio and neutrino momenta which are not fully constrained.

In about one third of top quark pair decays, one W boson decays to a neutrino and a charged electron or muon, while the other decays to hadrons, for a signature of two bottom-like jets, at least two additional jets, a charged electron or muon, and momentum imbalance from the unmeasured neutrino. This 'semi-leptonic' decay channel offers a compromise between the advantages and drawbacks of the dilepton channel compared to the all hadronic channel: fully measured decay kinematics and a better branching fraction than the dilepton channel, with reduced combinatorial possibilities compared to the all hadronic channel.

Top quarks have been the focus of intense study since their discovery, with tens of thousands of pairs produced by the Tevatron, and several million pairs produced recently in proton-proton collisions at the Large Hadron Collider, where the cross section and luminosity are higher. The focus on top quarks is due in part to the possibility of studying their properties without the interference of hadronization, and in part due to the particular capacity of top quark measurements to probe the Standard Model and extensions of the Standard Model. Precision measurement of the spectacularly large top quark mass, when combined with W mass measurements, until recently offered the best constraints on the mass of the Standard Model H^0. With the recent direct measurement of the mass of a new scalar boson consistent with H^0 [27, 28], the precision mass measurements constitute a test of the Standard Model. Decays of the very massive particles predicted by supersymmetric extensions of the Standard Model could involve top quarks, and could share event signatures with top quark pairs. Top pair production is a major background to searches for supersymmetry, and so must be well understood in order to search for evidence of processes with much smaller cross sections. Observations of top quark pairs can also be used to probe the Standard Model description of strong interactions, as will be discussed in the next chapter.

2 Charge Asymmetry

The prevalence of matter and relative absence of antimatter in the universe implies $\mathcal{CP}$ symmetry violation, or differences in the interactions of matter and antimatter, at a scale unexplained by mechanisms of the Standard Model. Weak interactions in the Standard Model admit $\mathcal{CP}$ violations through a complex phase in the CKM matrix [41]. Strong interactions in the Standard Model admit $\mathcal{CP}$ violating terms in the Lagrangian density, but those terms must be suppressed by fine-tuning of parameters in order to match experimental results which show no strong $\mathcal{CP}$ violation at low energy. Consistent with an experimental strategy of probing the Standard Model comprehensively and precisely in search of observations it fails to explain, the purpose of this work is to probe the differences in behavior of top quarks and top antiquarks in proton-proton collisions, in the process $\mathrm{pp} \to \mathrm{t\bar{t}}$.

There are several reasons to expect that this measurement could be sensitive to mechanisms not included in the Standard Model. First, top quarks are the only particles with color charge for which the kinematics can be observed without the convoluting effects of hadronization, due to their very brief lifetime, so they offer a unique channel for observations of the strong force. Second, it is natural to expect an additional $\mathcal{CP}$ violating mechanism to be more significant at the higher energies in which top quarks are produced, since it would resolve the mismatched observations of the nearly $\mathcal{CP}$ symmetric low energy Standard Model and the large matter-antimatter asymmetry, which would have developed at a time when the universe had much higher ambient energy. Third, similar measurements of top quarks in proton-antiproton collisions at the Tevatron have indicated interesting deviations from Standard Model predictions [42, 43].

Let X be an observable which negates under the exchange $\mathrm{t} \leftrightarrow \bar{\mathrm{t}}$, and $\mathrm{d}\sigma/\mathrm{d}X$ be its differential cross section. The probability density of X is

$$\rho(X) = \frac{1}{\sigma}\frac{\mathrm{d}\sigma}{\mathrm{d}X}. \tag{2.1}$$

The difference in behavior of top quarks and top antiquarks can be summarized by the $\mathrm{t\bar{t}}$ charge asymmetry,

$$A_c^X = \int_0 \rho(X)\mathrm{d}X - \int^0 \rho(X)\mathrm{d}X. \tag{2.2}$$

Equation 2.2 is equivalent to

$$A_c^X = 2\int_0 \rho^-(X)\mathrm{d}X, \tag{2.3}$$

where the symmetric (+) and antisymmetric (−) components of $\rho(X)$ are

$$\rho^{\pm}(X) = \left[\rho(X) \pm \rho(-X)\right]/2. \tag{2.4}$$

A non-zero value of A_c^X does not itself imply broken $\mathcal{C}$ symmetry, since $X \to -X$ is a conjugation of only top and anti-top quarks, rather than all particles in the system. However, a measured value of A_c^X significantly different from the value predicted by the Standard Model would hint strongly at a new mechanism which could be relevant to the wider problem of $\mathcal{CP}$ asymmetry.

2.1 In the Standard Model

The process

$$\mathrm{Q}_1 + \bar{\mathrm{Q}}_2 \to \mathrm{q}_3 + \bar{\mathrm{q}}_4 + \mathrm{g}_5, \tag{2.5}$$

in which a pair of massive quarks $(\mathrm{Q}_1, \bar{\mathrm{Q}}_2)$ annihilate via the strong interaction to produce two negligible mass quarks $(\mathrm{q}_3, \bar{\mathrm{q}}_4)$ and a gluon (g_5), has a $SU(3)_C$ next-to-leading order matrix element $\mathcal{M}(1,2,3,4,5)$ given by Reference [44]. This matrix element is $\mathcal{C}$ symmetric, since $|\mathcal{M}(1,2,3,4,5)|^2 - |\mathcal{M}(2,1,4,3,5)|^2$ is identically zero. However, the antisymmetric component of the absolute square matrix element under exchange of only the heavy quarks is not symmetric, since $|\mathcal{M}(1,2,3,4,5)|^2 - |\mathcal{M}(2,1,3,4,5)|^2$ is not generally zero. The processes

$$\mathrm{q} + \bar{\mathrm{q}} \rightarrow \mathrm{Q} + \bar{\mathrm{Q}} + \mathrm{g} \tag{2.6}$$

$$\mathrm{q} + \mathrm{g} \rightarrow \mathrm{Q} + \bar{\mathrm{Q}} + \mathrm{q} \tag{2.7}$$

$$\bar{\mathrm{q}} + \mathrm{g} \rightarrow \mathrm{Q} + \bar{\mathrm{Q}} + \bar{\mathrm{q}} \tag{2.8}$$

have the same absolute square matrix elements as process (2.5), but for swapping and negating of some momenta. The Standard Model generally predicts non-zero A_c^X for observables $\{X\}$ which negate under the exchange $\mathrm{Q} \leftrightarrow \bar{\mathrm{Q}}$ for the processes (2.6, 2.7, 2.8), since the antisymmetric (under $\mathrm{Q} \leftrightarrow \bar{\mathrm{Q}}$) component of the absolute square matrix element is proportional to the differential cross section and is not zero. The process

$$\mathrm{Q}_1 + \bar{\mathrm{Q}}_2 \rightarrow \mathrm{g}_3 + \mathrm{g}_4 + \mathrm{g}_5 \tag{2.9}$$

also has a $\mathcal{C}$ symmetric $SU(3)_C$ absolute square matrix element [44]. In this case, charge conjugation is equivalent to $\mathrm{Q} \leftrightarrow \bar{\mathrm{Q}}$, since the heavy quarks are the only particles in the process with charge. The related process

$$\mathrm{g} + \mathrm{g} \rightarrow \mathrm{Q} + \bar{\mathrm{Q}} + \mathrm{g} \tag{2.10}$$

is therefore predicted by the Standard Model to have $A_c^X = 0$, for observables $\{X\}$ which negate under the exchange $\mathrm{Q} \leftrightarrow \bar{\mathrm{Q}}$. Corrections to the next-to-leading order calculation due to higher orders and coherent gluon radiation have been investigated extensively [45–49].

The production of top quark pairs at hadron colliders occurs via the processes (2.6, 2.7, 2.8, 2.10), with t and $\bar{\mathrm{t}}$ filling the role of the massive quarks. These

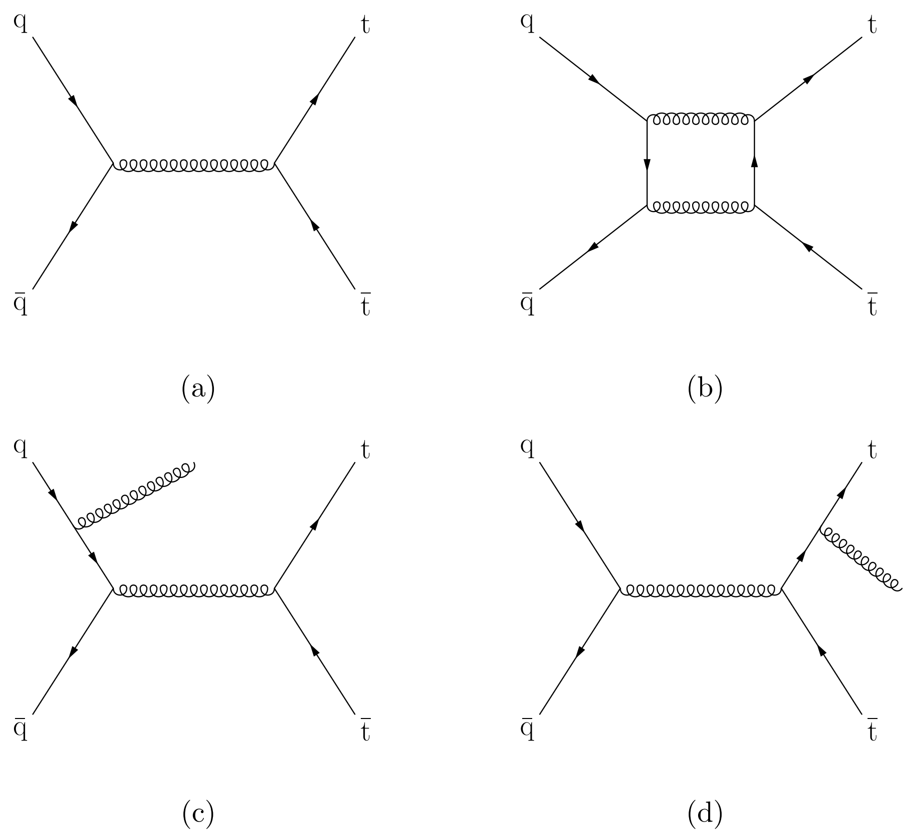

Figure 2.1: Example Feynman diagrams for $t\bar{t}$ production from quark-antiquark annihilation, $q\bar{q} \rightarrow t\bar{t}$. Diagrams with initial and final state gluon radiation are shown in (c) and (d).

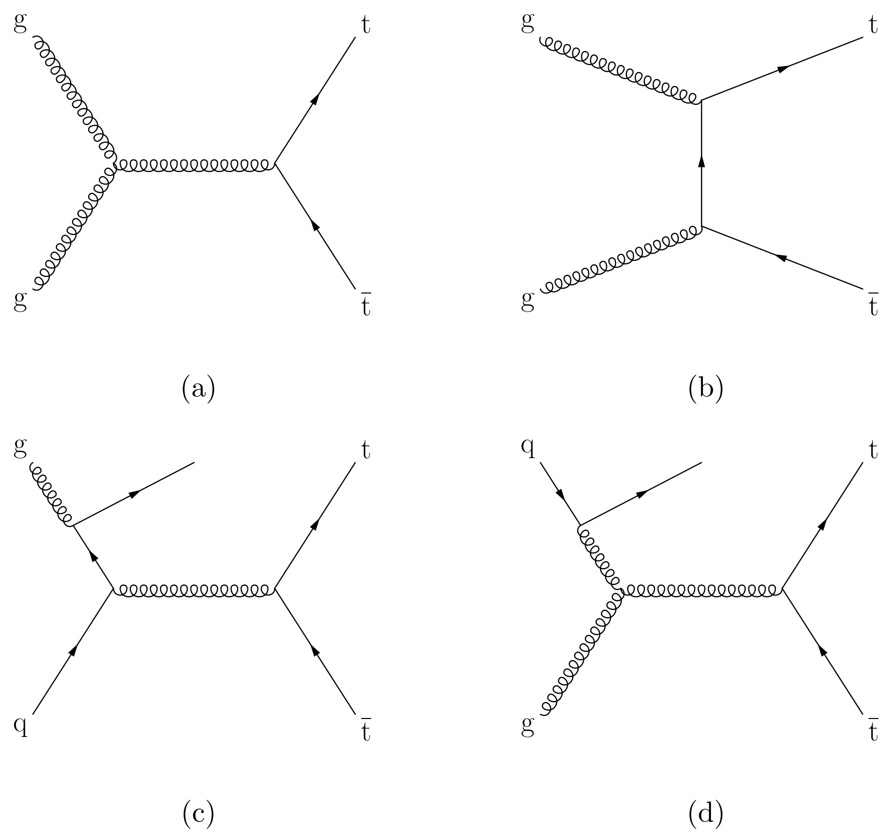

Figure 2.2: Example Feynman diagrams for $t\bar{t}$ production processes involving gluons, $gg \to t\bar{t}$ (a,b) and $qg \to t\bar{t}q$ (c,d). Diagrams for $\bar{q}g$ are identical to those for qg, substituting $q \to \bar{q}$.

processes are more easily referred to by their initial states, respectively $\mathrm{q\bar{q}}$, qg, $\mathrm{\bar{q}g}$, and gg. Selected leading order Feynman diagrams are shown for the $\mathrm{q\bar{q}}$ process in Figure 2.1, and for the gg and qg processes in Figure 2.2. The final state gluon in $\mathrm{q\bar{q}}$ or gg processes can have arbitrarily low energy in the center of mass system, approximating its absence. Similarly in processes qg or $\mathrm{\bar{q}g}$, the momentum transfer to the final state (anti)quark from the initial state (anti)quark or gluon can be arbitrarily small, in which case the process approximates $\mathrm{q\bar{q}}$ or gg. Additional $\mathrm{t\bar{t}}$ production processes with the same initial states exist in which more gluons accompany the final state, but each additional gluon vertex suppresses the magnitude of a process by a factor of the strong coupling.

The $\mathrm{t\bar{t}}$ differential cross section arising from these processes, and in particular the antisymmetric probability density, depends on the density of initial states available in the particular colliding hadrons [50]. The initial state densities are charge antisymmetric in proton-antiproton collisions at the Tevatron, while they are charge symmetric in proton-proton collisions at the Large Hadron Collider (LHC). Tevatron collisions are consequently dominated by the $\mathrm{q\bar{q}}$ process, which contributes more than 85% of the $\mathrm{t\bar{t}}$ cross section [51]. At the LHC, greater gluon densities at higher collision energy and the symmetric initial states, with no valence antiquarks, ensure the dominance of the gg process, as well as unequal contributions from the qg and $\mathrm{\bar{q}g}$ processes.

At the Tevatron, the charge asymmetry of initial states makes it convenient to define a $\mathrm{t\bar{t}}$ charge asymmetry observable with respect to the direction of the colliding proton. Particle rapidity, defined from the particle energy (E), longitudinal momentum (p_z), and speed of light (c) as

$$y = \frac{1}{2} \ln \frac{E + cp_z}{E - cp_z}, \tag{2.11}$$

changes additively under boosts along the proton axis, so rapidity differences like $\Delta y_{\mathrm{t\bar{t}}} = y_{\mathrm{t}} - y_{\mathrm{\bar{t}}}$ between top and anti-top have the advantageous property of independence from the unconstrained longitudinal momentum of the colliding system.

The observable $\Delta y_{\mathrm{t\bar{t}}}$ also negates under the exchange $\mathrm{t} \leftrightarrow \bar{\mathrm{t}}$, as well as under the exchange $\mathrm{p} \leftrightarrow \bar{\mathrm{p}}$, so it is a good candidate for observations of $\mathrm{t\bar{t}}$ charge asymmetry relative to the proton direction, sometimes referred to as forward-backward asymmetry, $A_{FB}^{\mathrm{t\bar{t}}}$. It has been measured by the DØ and CDF collaborations to be of the same sign as the Standard Model prediction (positive), but with a magnitude several times greater, with a significance of about three standard deviations [42, 43]. There are also indications the excess asymmetry is greater at higher $\mathrm{t\bar{t}}$ invariant mass.

Due to the symmetry of initial states in pp collisions, it is not possible to define forward-backward asymmetry at the LHC. However, since valence type quarks tend to carry a greater portion of the hadron's longitudinal momentum than antiquarks from the sea, $\mathrm{q\bar{q}}$ process events tend to be boosted in the direction of the initial state quark, and the same physics that leads to a positive Tevatron $A_{FB}^{\mathrm{t\bar{t}}}$ gives rise to a forward-central $\mathrm{t\bar{t}}$ charge asymmetry in pp collisions. The qg process contributes to the forward-central $\mathrm{t\bar{t}}$ charge asymmetry with the same sign, since the valence quarks also carry statistically more longitudinal momentum than gluons, and the underlying asymmetry in the matrix element has the same sign. Contributions to the cross section from $\mathrm{\bar{q}g}$ initial states is small, since there are no valence anti-quarks, and the forward-central asymmetry of these events is negligible anyway, since valence quarks and gluons are more balanced in initial momentum. The observable $\Delta\,|y|_{\mathrm{t\bar{t}}} = |y_{\mathrm{t}}| - |y_{\mathrm{\bar{t}}}|$ negates under the exchange $\mathrm{t} \leftrightarrow \bar{\mathrm{t}}$ and obtains an asymmetric differential cross section from the same underlying relationships that give rise to the Tevatron forward-backward asymmetry. It has been employed by CMS and ATLAS collaborations to measure the forward-central $\mathrm{t\bar{t}}$ charge asymmetry A_c^y [52–54]. The precision of these measurements has not yet been great enough to confirm the sign of A_c^y, which is predicted by the Standard Model to be positive [55, 56].

LHC collisions yield diluted information about asymmetry of the absolute square matrix elements compared to Tevatron collisions, due to the inefficiency of determining the initial quark direction via the longitudinal boost of the colliding system, and due to the large contribution of the symmetric gg process to the total cross section. Two advantages of the LHC are a greater luminosity and a much greater $\mathrm{t\bar{t}}$ cross section, which together guarantee the availability of many more top quark pairs for analysis. An additional interesting feature of pp collisions is the possibility to observe a $\mathrm{t\bar{t}}$ charge asymmetry based on an axis defined by the third final state particle, rather than the initial state particles. The Standard Model predicts symmetric $\mathrm{t\bar{t}}$ kinematics relative to final state gluons, but a non-zero $\mathrm{t\bar{t}}$ charge asymmetry relative to final state (anti)quarks. For pp collisions this $\mathrm{t\bar{t}}$ charge asymmetry may be observable, since the qg process has a much greater cross section than the $\mathrm{\bar{q}g}$ process.

2.2 Beyond the Standard Model

One of the leading candidate mechanisms to explain observations of forward-backward asymmetry in Tevatron proton-antiproton collisions is the chiral color model. Although there are several variations of the model, the common idea is to replace the $SU(3)_C$ gauge symmetry of the Standard Model with the larger symmetry group $SU(3)_L \otimes SU(3)_R$, plus a scalar field component to enable recovery of the observed $SU(3)_C$ symmetry via spontaneous symmetry breaking similar to that of electroweak theory [57]. In addition to the eight vector boson gluons, the extended gauge group has eight axial vector bosons, which couple to color charge and acquire mass via spontaneous symmetry breaking. Massive, colored, axial vector bosons are known as axigluons. Interference between gluon and axigluon contributions to the differential cross section can result in significant forward-backward or forward-central $\mathrm{t\bar{t}}$ asymmetry at the leading order.

Direct searches for narrow resonances in dijet invariant mass distributions constrain axigluon models [58–61]. Models in which axigluons couple with universal strength to all quark flavors and decay with narrow resonances have been ruled out for axigluon mass less than several $\mathrm{TeV/c^2}$, but flavor dependent coupling models are not yet ruled out for axigluon mass around $2\,\mathrm{TeV/c^2}$ [62]. Flavor dependent models require a fourth quark generation. Alternatively, flavor independent models with light axigluons have not yet been ruled out in the case that axigluons decay with a wide resonance, or to multijets via intermediate resonances [63]. In particular, the latter reference finds that a flavor independent axigluon model with intermediate resonances and axigluon mass between $100\,\mathrm{GeV/c^2}$ and $400\,\mathrm{GeV/c^2}$ is consistent with Tevatron and LHC observations.

While the present analysis seeks to measure forward-central $\mathrm{t\bar{t}}$ asymmetry only in the context of the Standard Model, the technique is general, and can be adapted to measure the asymmetry in alternative models like chiral color.

3 Experimental Apparatus

Data for this analysis was collected by the Compact Muon Solenoid experiment in 2012, from observations of proton-proton collisions at the Large Hadron Collider.

3.1 Large Hadron Collider

The Large Hadron Collider (LHC) is an accelerator and storage ring for counter-circulating beams of protons or heavy ions [64], operated by the European Center for Nuclear Research (CERN). The ring circles the 27 km tunnel previously occupied by the Large Electron Positron collider, located at a depth of about 100 m underground in the border region of France and Switzerland. The hadron beams are allowed to intersect at four distinct tangents, shown schematically in Figure 3.1a, and the resulting high energy collisions are observed with detectors of four corresponding experimental collaborations: ATLAS[1]; CMS; LHCb[2]; and ALICE[3]. The ATLAS and CMS detectors are located at high luminosity points and are used for a wide variety measurements and have a similar symmetric design, while the LHCb and ALICE detectors are more specialized and located at lower luminos-

[1] A Toroidal LHC Apparatus

[2] LHC beauty experiment

[3] A Large Ion Collider Experiment

ity points. The purpose of the LHC is to extend high energy particle physics research to new frontiers in energy and luminosity with its design parameters of 14 TeV center of mass proton-proton collisions at an instantaneous luminosity of $10^{34}\,\mathrm{cm}^{-2}\,\mathrm{s}^{-1}$, which are orders of magnitude greater than those of the previous state of the art collider, Fermilab's Tevatron.

LHC proton beams begin with ionization of hydrogen atoms and linear acceleration to 50 MeV. In successive stages through the Proton Synchrotron Booster (PSB), the Proton Synchrotron (PS), and the Super Proton Synchrotron (SPS), the protons are accelerated in bunches of up to 10^{11}, to 1.4 GeV, 26 GeV, and 450 GeV, respectively, in circling many times past radio frequency cavities before injection into the next stage, as shown in in Figure 3.1b. Bunches are injected into the LHC about 80 at a time, accumulating to as many as 2808 per beam. Upon completion of the fill, the circulating beams are accelerated, stabilized, focused, and intersected at the four points. Collisions occur with a minimum period of 25 ns for the duration of the fill, which can last from an hour to more than a day.

The LHC overcomes many technical challenges to produce high energy, high luminosity proton collisions, of which it is worth mentioning several. To turn 7 TeV beams in the LHC radius, 8 Tesla magnetic fields are required. This capability is satisfied by more than 1200 superconducting NbTi dipole magnets cooled to below 2K with superfluid helium around the entire circumference of the machine, which in turn requires an extensive cryogenic system. Further complicating the arrangement, space limitations in the tunnel require the bending magnets for each beam to be mechanically joined, sharing a cold mass and cryostat. Beam control is supplied by similar superconducting magnets of higher moments, and the radio frequency acceleration system also utilizes superconductivity and the cryogenic system. The beams must circulate in high vacuum (10^{-10} mbar) over the entire circuit in order to maintain long beam lifetime and to prevent background events at the experiments.

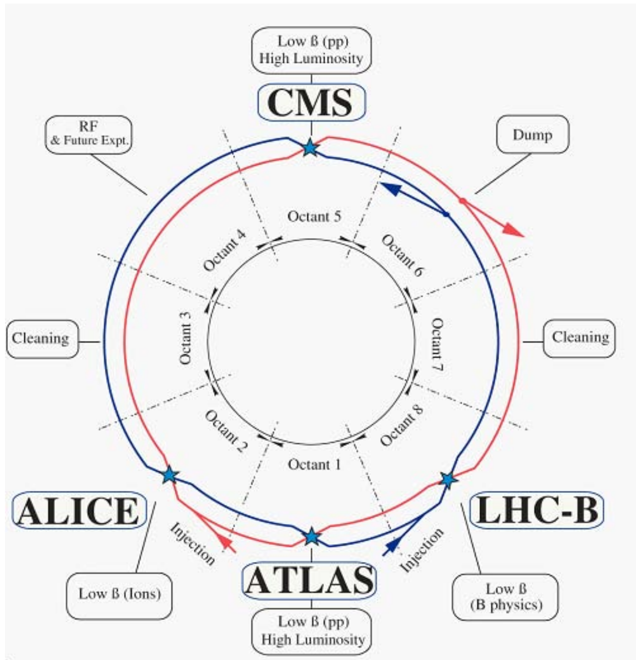

(a) Schematic layout of the LHC (Beam 1–clockwise, Beam 2–anticlockwise).

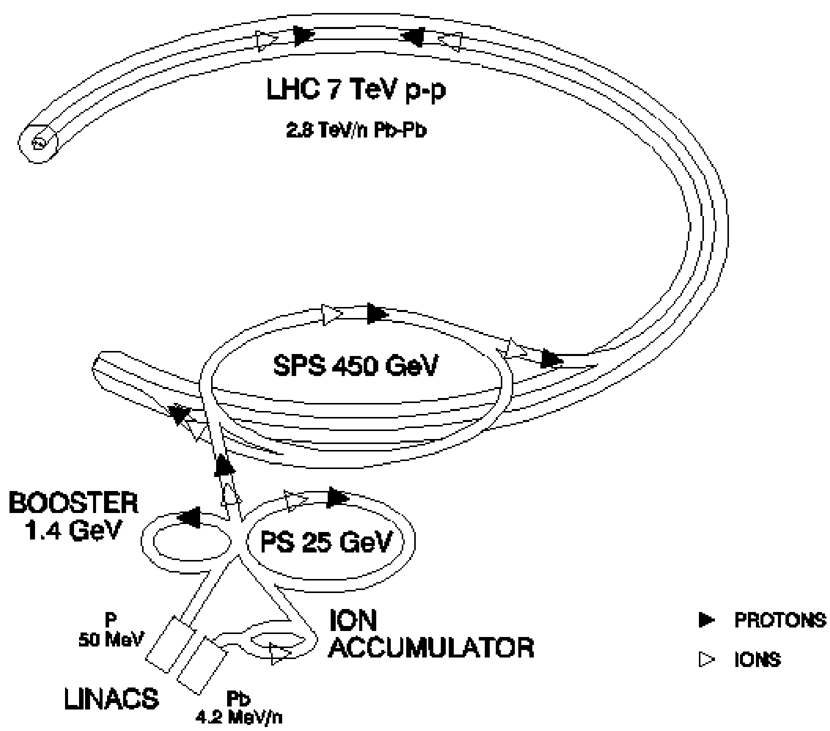

(b) The LHC injector complex.

Figure 3.1: LHC diagrams and captions, courtesy of CERN.

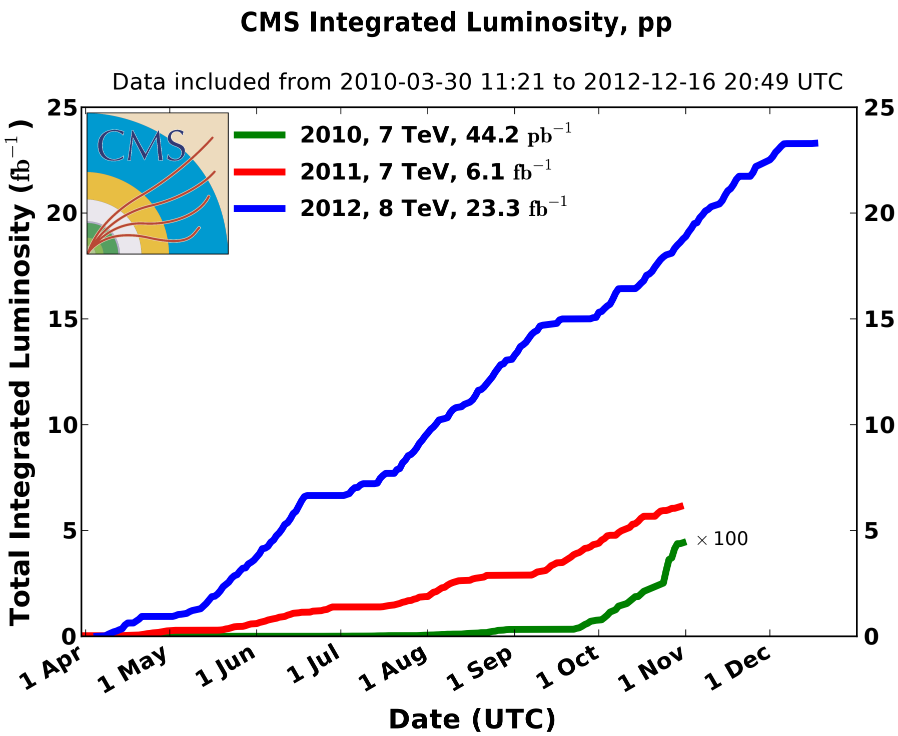

Figure 3.2: LHC integrated luminosity 2010-2012, courtesy of CERN.

In 2008, shortly after circulating inaugural beams, the LHC machine suffered a serious setback when about 100 bending magnets in octants 3 and 4 lost superconductivity, causing their windings to resistively heat and explosively vaporize their liquid helium coolant. The accident caused a delay of more than a year during which collaborators cleaned up the debris, evaluated and corrected the design flaws, and rebuilt and commissioned the machine.

As a result of vulnerabilities in the bending magnets, it was decided to accelerate the beams to a maximum of 3.5 TeV each in 2010 and 2011, and to 4.0 TeV each in 2012. Instantaneous luminosity in 2012 was frequently near $6 \cdot 10^{33}\,\mathrm{cm}^{-1}\,\mathrm{s}^{-1}$, with about 1000 colliding bunches per beam spaced at 50 ns. Integrated luminosity curves for all three years are shown in Figure 3.2. Despite not yet reaching its design parameters as of 2013, the LHC has delivered enough integrated luminosity for the experiments to conduct extensive research programs.

3.2 Compact Muon Solenoid

The Compact Muon Solenoid (CMS) collaboration takes its name from the general-purpose particle detector located at intersection point five (P5) on the LHC ring underneath Cessy, France. The collaboration consists of more than 3000 members from 40 countries, including 900 from the United States. About half are physicists, and a quarter each are graduate students or engineers. The collaboration was founded in the early 1990s, and approval of the experiment followed in 1993. The CMS collaboration constructed the eponymously named detector between 1998 and 2008, and used it to record data from LHC collisions in 2010, 2011, and 2012. Notable collaboration results include the discovery of a boson consistent with the Standard Model H^0 [27], and the extension of lower limits on the lightest possible masses of supersymmetric particles [65, 66]. The detector is described extensively elsewhere [67], but an overview is appropriate here.

The CMS detector is a cylindrically symmetric construction around the LHC beamline, centered on the intersection point, for the purpose of precisely measuring the energy and momenta of debris particles from the hadron collisions. It consists of several nested tracking and calorimetry subdetectors, supported by a superconducting solenoid magnet with a bore radius of 3 m and an operating field strength of 3.8 Tesla. The magnetic field deflects charged debris particles along spiral paths parallel to the field and beamline, each with a radius proportional to its transverse momentum and circulation according to its charge. The debris particles most relevant to physics analysis are those with high transverse momentum, corresponding to path radii large enough that revolution is interrupted upon reaching the calorimeters, or in the case of muons, upon escaping the magnet's bore. Muons are not stopped by the calorimeters, and can escape the bore with a transverse momentum of about 2 GeV/c. Once outside the bore, muons paths follow opposite circulation in the diminishing return field.

The coordinate system convention for CMS orients the x-axis radially inward toward the LHC center and the y-axis vertically upward from the nominal interaction point. The z-axis is defined by their cross product, and is directed tangent to the LHC beams. The azimuthal angle ϕ is measured into $+y$ from the x-axis, and the polar angle θ runs from 0 in the $+z$ direction to π on the $-z$ direction. The pseudorapidity is a practical alternative to the polar coordinate, defined as $\eta = -\ln\left(\tan\left(\frac{\theta}{2}\right)\right)$. Projections of momenta onto the x–y plane, transverse to the beamline, are denoted p_{T}, and the negative sum of all transverse momenta in an event is labeled $E_{\mathrm{T}}^{\mathrm{miss}}$. As shown in Figure 3.3, CMS is instrumented over most of the solid angle around the interaction point, longitudinally over an absolute pseudorapidity $|\eta| < 5.0$, and azimuthally over the full 2π.

The innermost detector is the Pixel Silicon Tracker, one meter long with three barrel layers at radii of 4.4, 7.3, and 10.2 cm from the beamline, and two endcap layers on each end. The purpose of its 66 million $100 \times 150\,\mu$m pixels, is to precisely pinpoint collision vertices by constraining measurements of charged particle tracks near the beamline, while operating in an environment of intense radiation. The Silicon Strip Tracker complements the Pixel detector with 10 barrel layers of strip modules (5×10 cm) to a radius of 1.2 m, and 12×2 endcap wheels, which detect passing charged particles with $100\,\mu$m scale azimuthal and 10 cm scale longitudinal resolution. Several layers and wheels are doubly instrumented with modules at a slight angle to provide high longitudinal precision. In each silicon module, the n-doped bulk is fully depleted of space charge under reverse bias from the back-plane, so that passing charged particles separate charge carriers which are sensed capacitively as they drift toward the p-doped strips. Analog signals from strip channels are integrated locally on each module, and those that pass a threshold are converted to laser pulses, and sent over fiber optic connections to digitizing and data acquisition equipment in rooms adjacent to the collision hall. There are about 9 million strip channels instrumenting more than $200\,\mathrm{m}^2$

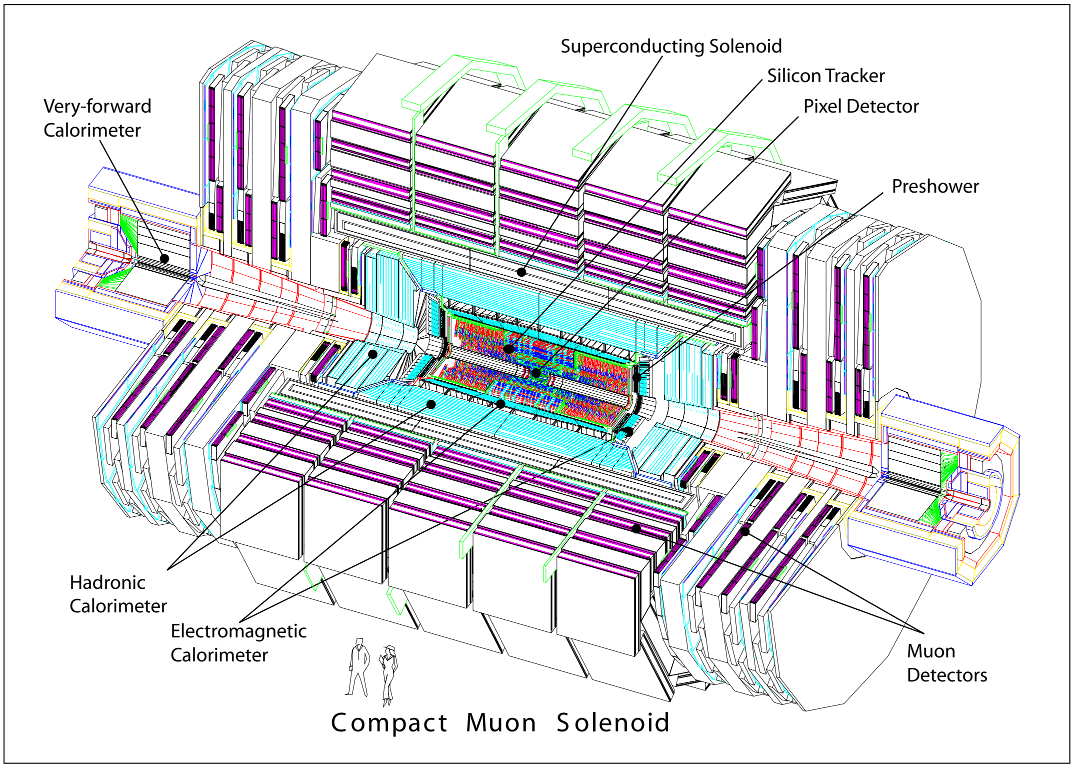

(a) Perspective view of the CMS detector.

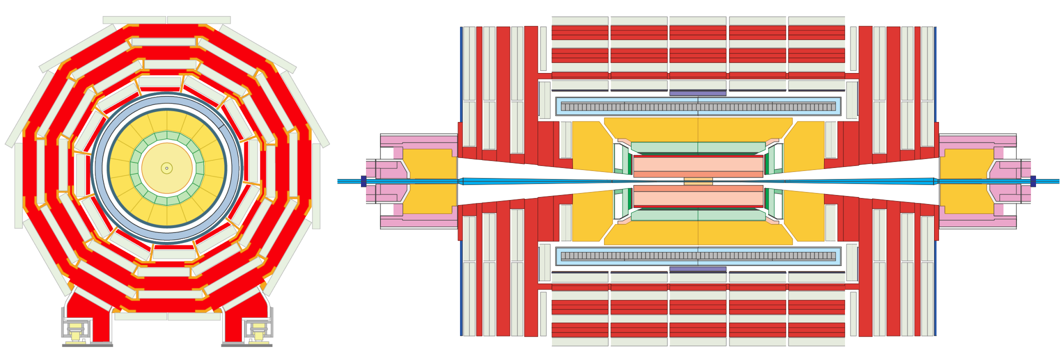

(b) Radial (left) and longitudinal schematic cross sections of the CMS detector.

Figure 3.3: Diagrams of the CMS detector, courtesy of CERN.

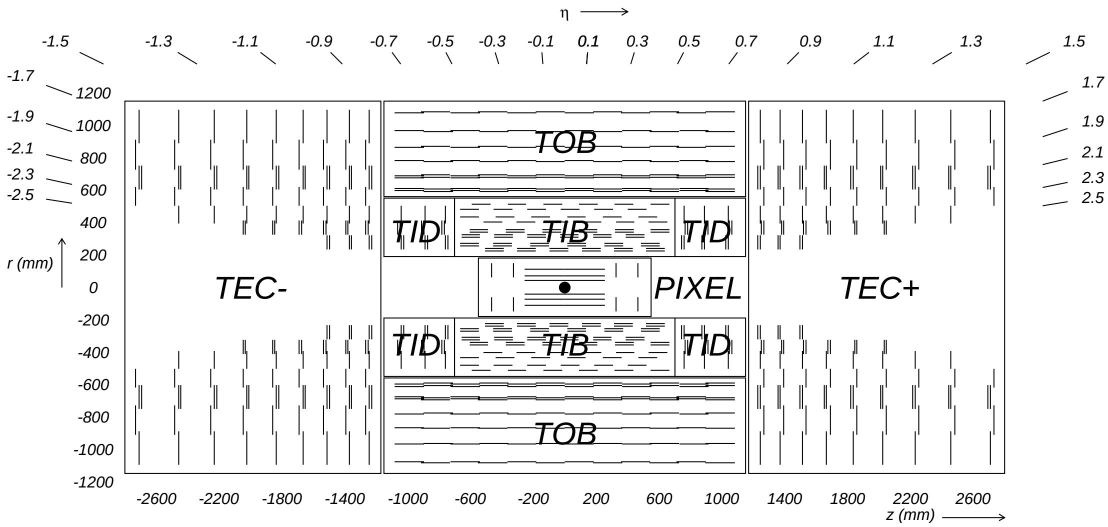

Figure 3.4: Schematic cross section through the CMS tracker, as originally published by CMS [67]. Each line represents a detector module. Double lines indicate back-to-back modules which deliver stereo hits.

of silicon. The combined tracking system is able to perform under the extreme LHC conditions of intense radiation and 25 ns period collisions, and with the very high occupancy of charged particles in heavy ion collisions. It enables the reconstruction of charged particle tracks with efficiency greater than 90%, and with transverse momentum resolution of about 1%, at the cost of a relatively high material budget which causes an acceptable amount of undesirable energy loss as the particles traverse. As shown in Figure 3.4, the tracking detectors inside the magnet bore are instrumented over an absolute pseudorapidity $|\eta| < 2.5$.

The calorimetry system surrounds the silicon tracker, but is still contained within the magnet bore. Its purpose is to measure the energy of debris particles from the collision by inducing each one into a cascading shower of material interactions such that all of the kinetic energy is absorbed. Muons and neutrinos are excepted, since muons are much more massive than the constituents of the calorimeter materials and they leave behind only the minimum ionizing radiation, while neutrinos essentially do not interact with the detector at all. Two subdetectors compose the calorimetry system, the Electromagnetic Calorimeter (ECAL) over radius range from 1.29 m to 1.53 m, and behind it the Hadronic Calorimeter (HCAL), which fills the remainder of the bore. The endcaps of the main calorimeters are instrumented to absolute pseudorapidity 3.0, while special forward calorimeters extend the range to $|\eta| = 5.0$. The ECAL is a homogeneous calorimeter built of lead-tungstate crystals, which are about 26 times longer than the characteristic radiation length of electrons and photons in the material. The crystals are transparent, and when electrons or photons are stopped, light from the shower propagates outward where it is measured by avalanche photodiodes (barrel), or vacuum phototriodes (endcaps). The ECAL measures photon and electron energies with a resolution on the order of 0.5%. Preceding the ECAL endcap crystals are 3 radiation lengths of lead instrumented with two orthogonal layers of silicon strip detectors, with the goal of measuring the profiles of developing showers, which are more eccentric for neutral pions than for single photons or electrons. The HCAL is a sampling calorimeter with a minimum of 6 hadronic radiation lengths (plus $\sim$1 from the ECAL), composed of towers of brass plates interleaved with scintillating plastic embedded with wavelength shifting fibers. While most of an incident hadron's energy is absorbed in the brass, the scintillating plastic converts some of the shower into light, which finds its way out through the embedded fibers to photodiodes for measurement.

Outside the magnet bore, muon tracking chambers are interleaved with an iron return yoke for the field. In the barrel region, the muon tracking chambers consist of four layers of gas-filled drift tubes (DT), with longitudinally oriented wires held at high potential. Traversing muons ionize the gas, and the loosened electrons cascade towards the wire, causing a measurable electric signal. The location of the passing track is calculated from the integrated signal on neighboring wires. The drift tubes have high azimuthal and radial resolution ($\sim$100 μm), and very coarse longitudinal resolution ($\sim$ meter). There are 4 layers of muon cathode strip chambers (CSC) in each endcap. These contain a gas, azimuthially oriented anode wires, and radially oriented cathode strips. Traversing muons ionize the gas, and the electrons cascade to the anode wires, allowing the radial position to be measured, similarly to the drift tubes. The positive ions cascade to the cathode strips, allowing the azimuthal position to be interpolated as well. The CSC system measures all three spatial coordinates with $\sim 100\,\mu$m resolution, and is instrumented to absolute pseudorapidity 2.4. In the interest of making triggering decisions in a timely manner, the CMS muon system is also instrumented throughout with resistive plate chambers (RPC). An RPC consists of a large high-voltage plate sandwiched with gas and grounding plates. They take less time to integrate a signal than the DT system, but provide coarser spatial resolution.

To summarize the detection capabilities of CMS, it is useful to catalog the different signatures of various particles. A muon leaves a curved track in the tracker, minimum ionizing energy in the calorimeters, and a track with the opposite curvature in the muon system, with the charge and momentum measurable from the direction and radius of track curvature. An electron leaves a curved track in the tracker, and deposits all of its energy in the ECAL, never reaching the HCAL or muon system. A photon deposits all its energy in the ECAL like an electron, but leaves no track in the tracker unless it converts into a positron-electron pair, which then leave opposite curvature tracks with a vertex displaced from the primary collision point. Neutral pions, which decay immediately to two photons, can be discriminated from photons in the Preshower by their eccentric shower shape. Longer-lived neutral hadrons leave some energy in the ECAL, but most of it in the HCAL. Charged hadrons interact with the calorimetry like neutral hadrons but leave tracks in the tracking system as well. Neutrinos are not detected directly, but the sum of their momenta transverse to the beam axis can be estimated by the imbalance in the total measured momentum of the colliding system.

The CMS data acquisition system can only record about 300 events per second, many orders of magnitude below the design collision rate of 40MHz. In order to record events of interest, CMS employs a complicated triggering system to decide in real-time whether to record or ignore an event. It is sufficient to note here that triggering occurs at two consecutive levels: a low level hardware system, and a high level software system; and that the triggers used to collect the data for the present analysis require the identification of a single electron or a single muon, with high transverse momentum.

3.2.1 Role of the author in the CMS collaboration

The author first spent time at CERN in the summer of 2007, when he worked with a test beam collaboration for experimental silicon detectors, and began taking shifts to monitor the CMS Silicon Strip Tracker (SST), then in the Tracker Integration Facility (TIF) at the CERN Meyrin site. He returned to CERN in July of 2008 for a two year period, initially continuing with SST monitoring at P5, and becoming involved with SST commissioning based on cosmic muon tracks.

After the LHC magnet quench accident in September 2008, with proton collisions delayed for more than a year, CMS subdetector groups including the SST group continued planned commissioning activities with cosmic ray muons, rather than with collision events. The author was intimately involved with data analysis to characterize SST performance and determine the accuracy of the SST simulation. In particular, he was responsible for measuring signal coupling on neighboring strips, and collaborated in the measurement of strip signal to noise ratios, the Lorentz drift angle within the silicon modules, and the tuning of the simulation. Beginning in 2009, the author substituted SST monitoring service with responsibilities as the Local Reconstruction contact, which involved ensuring fast, reliable, and clear algorithms and implementations for reconstructing raw data into positions for later use by the tracking algorithms. Most of the Local Reconstruction software code needed revision in addition to a contact knowledgeable about the design. In particular there were two different algorithms in use for identifying groups of strips with signal, one in the High Level Trigger, and another offline, which the author replaced with a single implementation which served both cases.

Midway through 2009, in anticipation of the first proton collisions of unaccelerated LHC beams, the author became involved in a commissioning group specifically concerned with the performance of the detector with regards to supersymmetry searches. Most of this commissioning work involved understanding the features of various jet reconstruction algorithms and transverse momentum imbalance, and in developing tool chains for data analysis. This involvement naturally led to the author's participation in the initial searches for supersymmetric event signatures in the 2010 data, which resulted in the first published lower limits on supersymmetric particle masses from the LHC, greatly extending previous limits [66].

The author began developing the present analysis in 2011.

4 Analysis Strategy

Charge asymmetry associated with $\mathrm{t\bar{t}}$ production, defined in Equation 2.2, can only be measured by extrapolation from observations based on a model. Past measurements have extrapolated with an unfolding technique, which relies on a model for selection efficiencies and reconstruction effects [52–54]. In contrast to unfolding, this analysis uses an alternative extrapolation technique based on templates, in which the base model supplies reconstruction effects and the probability density function over the relevant observable, defined in Equation 2.1. Symmetric and antisymmetric components of the probability density, defined in Equation 2.4, serve as linear templates which are fit to the data.

In addition to measuring the inclusive forward-central asymmetry of $\mathrm{pp} \to \mathrm{t\bar{t}}$, this analysis will also attribute portions of it to the various partonic processes in pp collisions which produce $\mathrm{t\bar{t}}$ pairs. Subsequent references to the probability density of the $\mathrm{t\bar{t}}$ charge asymmetry observable will be as a symmetrically binned probability distribution $\vec{x}$, where the dimensionality of the vector is equal to the number of bins.

4.1 Template Parametrization

The base model predicts a probability distribution $\vec{x}$ for observable X, which implies a $t\bar{t}$ charge asymmetry $\hat{A}_c^X$ as defined in Equation 2.2. An extended model can be constructed from a linear combination of the symmetric and antisymmetric components of the base model probability distribution using a single parameter α

$$\vec{x}^{\alpha} = \vec{x}^{+} + \alpha\vec{x}^{-}. \tag{4.1}$$

From Equation 2.3, the parametrized charge asymmetry is

$$A_c^X(\alpha) = \alpha\hat{A}_c^X, \tag{4.2}$$

and the base model is described by $\alpha = 1$.

The inclusive $t\bar{t}$ charge asymmetry A_c^X is a sum of contributions from the set of processes $k \in \{\mathrm{gg}, \mathrm{q\bar{q}}, \mathrm{qg}, \mathrm{\bar{q}g}\}$ which compose $\mathrm{pp} \to t\bar{t}\times$,

$$A_c^X = \sum_k A_c^{X(k)}. \tag{4.3}$$

The contribution of each process k is the product of its intrinsic $t\bar{t}$ charge asymmetry $A_c^{X[k]}$ and its fractional contribution to the total $\mathrm{pp} \to t\bar{t}\times$ cross section,

$$A_c^{X(k)} = f_k A_c^{X[k]}, \qquad f_k = \frac{\sigma(k \to t\bar{t}\times)}{\sigma(\mathrm{pp} \to t\bar{t}\times)}. \tag{4.4}$$

The intrinsic $t\bar{t}$ charge asymmetry of each process can potentially be parametrized with its own α_k. Note that the asymmetry contribution of each process is a function of the product $f_k\alpha_k$.

The measurement strategy is to find the set of values $\{f_k\alpha_k\}$ which best fits observations. In practice, this will be a 2-dimensional measurement, from which charge asymmetry contributions of two processes and the inclusive $t\bar{t}$ charge asymmetry will be extracted.

4.1.1 Parameter propagation

The parametrized probability distribution $\vec{x}^{\alpha}$ of Equation 4.1 is not directly observable in data, due to sculpting from selection criteria, blurring from imperfect reconstruction of the observable, and background process contamination. Considered below are the effects of selection and reconstruction.

Selection

The probability distribution $\vec{x}^{\alpha}$ is composed of selected and unselected events, each with their own respective probability distributions $\vec{x}^{\alpha}_{s}$ and $\vec{x}^{\alpha}_{\not s}$, weighted according to the efficiency of selection ϵ,

$$\vec{x}^{\alpha} = \epsilon \vec{x}^{\alpha}_{s} + (1-\epsilon)\vec{x}^{\alpha}_{\not s}. \tag{4.5}$$

The distributions of selected and unselected events can each be written as a sum of symmetric and antisymmetric components. Since the components of the base model are

$$\vec{x}^{\pm} = \epsilon \vec{x}^{\pm}_{s} + (1-\epsilon)\vec{x}^{\pm}_{\not s},$$

and since the sum of two (anti)symmetric distributions is (anti)symmetric, it must be the case that

$$\vec{x}^{\alpha}_{s} = \vec{x}^{+}_{s} + \alpha \vec{x}^{-}_{s}. \tag{4.6}$$

The parameter α can therefore be found by comparing observations to the base model templates for any selection of events, and used with Equation 4.2 to extrapolate the total $t\bar{t}$ charge asymmetry.

Reconstruction

An observable distribution $\vec{x}^{\alpha}$, perhaps of only selected events, is reconstructed imperfectly as $\vec{x}^{\alpha}_{\mathrm{rec}}$ according to some migration matrix M^{α},

$$\vec{x}^{\alpha}_{\mathrm{rec}} = M^{\alpha}\vec{x}^{\alpha}. \tag{4.7}$$

The migration matrix M in the base model is found from the joint distribution (X, X_{rec}). It can be decomposed into symmetrizing and antisymmetrizing components, $M^{\pm}$, which respectively produce completely symmetric or antisymmetric distributions in operating on a completely symmetric distribution. A non-zero antisymmetrizing component M^- implies a bias in the reconstruction. If a reconstruction bias M_0^- is intrinsic, independent of the fundamental asymmetry of the observable, then it is constant. If a reconstruction bias M_1^- is due to the fundamental asymmetry, the bias would reverse with reversal of the fundamental asymmetry, and would vanish for a model with no asymmetry. The migration matrix from the parametrized model must be

$$M^{\alpha} = M^{+} + M_0^{-} + \alpha M_1^{-}. \tag{4.8}$$

Matrices are linear operators, so Equation 4.7 reduces to

$$\vec{x}^{\alpha}_{\text{rec}} = M^{+}\vec{x}^{+} + \alpha\left(M^{+}\vec{x}^{-} + M_1^{-}\vec{x}^{+}\right) + \alpha^2 M_1^{-}\vec{x}^{-} + M_0^{-}\left(\vec{x}^{+} + \alpha\vec{x}^{-}\right). \tag{4.9}$$

In the case that the constant bias M_0^- and the quadratic component $M_1^-\vec{x}^-$ are negligible, the model reduces to the linear form

$$\vec{x}^{\alpha}_{\text{rec}} = \vec{x}^{+}_{\text{rec}} + \alpha\vec{x}^{-}_{\text{rec}}. \tag{4.10}$$

That this is the case for reconstruction in the present analysis is shown in Section 6.1. The parameter α can then be found by using an imperfectly reconstructed observable to compare observations to base model templates, and used with Equation 4.2 to extrapolate the total $\mathrm{t\bar{t}}$ charge asymmetry.

4.2 Classification of $\mathrm{t\bar{t}}$ Production Processes

The majority of top quark pairs at the LHC are expected to be produced through gluon-gluon fusion, in the process $\mathrm{gg} \to \mathrm{t\bar{t}}\times$, while a smaller portion are expected to be produced through quark-antiquark annihilation, in the process $q\bar{q} \rightarrow t\bar{t}\times$. In addition, some top quark pairs are produced in association with a final state (anti)quark with high transverse momentum, in the processes $qg \rightarrow t\bar{t}q$ and $\bar{q}g \rightarrow t\bar{t}\bar{q}$. Feynman diagrams for these $t\bar{t}$ production processes are shown in Figures 2.1 and 2.2.

Since gluon fusion (gg) and quark-antiquark annihilation ($q\bar{q}$) do not have interfering matrix elements, their contributions to the $t\bar{t}$ cross section can be calculated separately. Calculations of (anti)quark-gluon scattering (qg or $\bar{q}g$) require an explicit threshold on the momentum transfer from the final state light quark, since the process is the same as a $q\bar{q}$ or qg in the limit as the momentum transfer goes to zero. The transverse momentum of the final state light quark is an observable quantity which sets a lower bound on its momentum transfer, so it is convenient to define the qg and $\bar{q}g$ classification thresholds in terms of a minimum transverse momentum of the recoiling light quark. Events in the simulation which have a final state (anti)quark with transverse momentum less than the threshold are classified as either $q\bar{q}$ or gg by comparing the momentum transfer between the recoiling quark and the initial state partons q and g. If the magnitude of the momentum difference is smaller with g than with q, the process is classified as quark-antiquark annihilation, $q\bar{q}$, with the expectation of a process more like Figure 2.2c. If the magnitude of the momentum difference is smaller with q than with g, the process is classified as gluon fusion, with the expectation of a process more like Figure 2.2d.

While there is no theoretical motivation for the value of the classification threshold, in practice the choice is motivated by two competing interests. The first is the wish to avoid reliance of the classification scheme on implementation details of a specific calculation scheme, which can occur if the threshold is lower than that used in the calculation for handling infrared divergence at a particular order. The second is the wish to keep the threshold low enough to prevent the

$q\bar{q}$ category from carrying an appreciable $t\bar{t}$ charge asymmetry related an axis defined by the transverse momentum of the $t\bar{t}$ system (see Section 4.4). For the generator used in this analysis, discussed further in Section 4.5.1, a threshold of 20 GeV/c for (anti)quark transverse momentum balances these two interests.

4.3 Background Processes

This analysis will select $t\bar{t}$ events (signal) with a lepton+jets signature: a single electron or muon and at least four jets, as discussed in Section 1.7. Several other Standard Model processes can mimic the $t\bar{t}$ lepton+jets signature. Their contributions to the data sample can be minimized with careful selection criteria, but not avoided entirely, so they constitute a background on top of which the signal distribution must be evaluated.

The largest background contributions to $t\bar{t}$ lepton+jets selection are from processes which produce a W boson in conjunction with several jets (W+jets). These processes have a much greater cross section than $t\bar{t}$ processes, and an indistinguishable lepton signature when the W decays to a muon or electron. The transverse momenta of jets in W+jets events are typically less than those associated with top quark decay, so selection of W+jets events is significantly reduced relative to selection of $t\bar{t}$ events by requiring at least 4 jets with transverse momentum above thresholds. Requiring one or two jets which exhibit bottom-flavor properties also reduces the W+jets background significantly.

The next most significant background contribution is due to events which produce multiple jets (Multijet), particularly $pp \rightarrow b\bar{b}\times$. The charged lepton in selected multijet events is often due to the weak decay of a B meson within the hadronization products of a b-quark, so it is correlated with the jet direction. A requirement that the lepton be found in relative isolation, defined as the sum of neighboring particles' momenta relative to its own, allows significant reduction of selected multijet events relative to $\mathrm{t\bar{t}}$ events. Conversely, inverting the isolation requirement selects a control sample with an increased contribution from multijet events.

Processes which produce several jets in conjunction with an e^+e^- or $\mu^+\mu^-$ pair near the Z boson invariant mass resonance (Drell–Yan) have a large cross section but a low efficiency to pass the lepton+jets selection, which can happen when one lepton is not identified. Processes which produce a single top quark or antiquark (Single Top), especially in conjunction with a W boson, are difficult to filter from the $\mathrm{t\bar{t}}$ lepton+jets selection, but their cross section is much smaller than that of $\mathrm{t\bar{t}}$ production. Other Standard Model processes have a small enough product of selection efficiency and cross section that their contributions to the sample are negligible.

4.4 Observables

For the $\mathrm{t\bar{t}}$ charge asymmetry (2.2) to be defined, the observable on which it is based must negate under the exchange $\mathrm{t} \leftrightarrow \mathrm{\bar{t}}$. For use with the template technique, it is also desirable that the observables be bounded.

The $\mathrm{t\bar{t}}$ charge asymmetry related to the initial state partons has been measured by previous LHC analyses [52–54] using the difference in absolute rapidities of top (y_t) and antitop ($y_\mathrm{\bar{t}}$) quarks,

$$\Delta\left|y\right|_{\mathrm{t\bar{t}}} = \left|y_\mathrm{t}\right| - \left|y_\mathrm{\bar{t}}\right|. \tag{4.11}$$

Since the valence-type quarks carry on average a higher fraction of the proton momentum than antiquarks (gluons) from the hadron sea, any asymmetry in a top pair produced from initial state $\mathrm{q\bar{q}}$ (qg) can be expected to produce a difference in the widths of the rapidity distributions of the top and antitop quarks, and consequently an asymmetry A_c^y in the observable (4.11). A positive value of A_c^y

indicates an affinity of the top quark for the direction of the initial state quark, rather than antiquark (in $\mathrm{q\bar{q}}$) or gluon (in qg). The gg initial state is symmetric under exchange of $\mathrm{t} \leftrightarrow \bar{\mathrm{t}}$, so it cannot contribute to A_c^y. The contribution to A_c^y from the $\mathrm{\bar{q}g}$ initial state is small to negligible, since antiquarks and gluons are less differentiated in the fraction of the proton momentum they carry, and since the portion of $\mathrm{t\bar{t}}$ events with this initial state is small. In order to use a bounded observable, (4.11) is transformed with the hyperbolic tangent,

$$X_L = \tanh \Delta \left|y\right|_{\mathrm{t\bar{t}}} . \tag{4.12}$$

The hyperbolic tangent is a monotonic transformation symmetric about zero, so the asymmetry in X_L is also A_c^y. Standard Model values of A_c^y for inclusive $\mathrm{t\bar{t}}$ production have been calculated recently by Kühn and Rodrigo, and by Bernreuther and Si, for LHC running conditions [55, 56].

The $\mathrm{t\bar{t}}$ charge asymmetry related to a final state recoiling (anti)quark or gluon can be measured using the observable

$$X_T = -1 + \frac{2}{\pi}\phi_{\pm}, \tag{4.13}$$

where $\phi_{\pm}$ is the azimuthal opening angle (on $[0,\pi]$) between the momentum sum and difference of the top and antitop quarks, as shown in Figure 4.1. Both X_T and $-\cos\phi_{\pm}$ negate under $\mathrm{t\bar{t}}$ exchange, are bounded on [-1,1], and indicate the affinity of the top quark for the direction of the recoiling quark or gluon. Since their signs always match they have the same value of asymmetry A_c^ϕ, but X_T is preferable since it is more uniformly distributed than $-\cos\phi_{\pm}$. Note that asymmetry in X_T at the LHC is due almost entirely to the qg initial state, while at the Tevatron contributions to X_T asymmetry from qg and $\mathrm{\bar{q}g}$ initial states are equal and opposite, mostly canceling.

The transverse $\mathrm{t\bar{t}}$ charge asymmetry A_c^ϕ at the LHC is due mostly to the qg initial state while the forward-central $\mathrm{t\bar{t}}$ charge asymmetry A_c^y is due to both qg

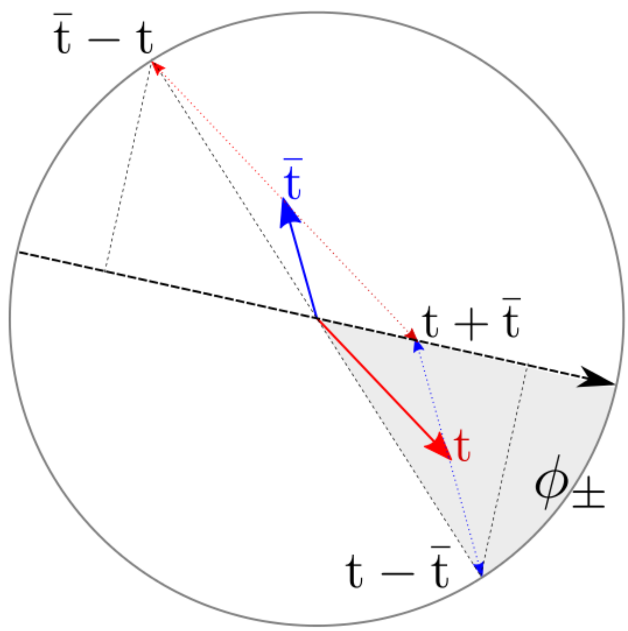

Figure 4.1: The azimuthal angle between the momentum sum and difference of the top and antitop quarks is $\phi_{\pm}$. The projection of the momentum on the transverse plane is shown for top (t) and antitop ($\bar{t}$).

and $q\bar{q}$ initial states. The contributions of each initial state to the total asymmetry A_c^y can be measured by simultaneously fitting their antisymmetric components in the joint distribution of X_L and X_T, given a ratio A_c^ϕ/A_c^y for the qg initial state. The symmetric (+) and antisymmetric (−) components of the joint distribution $\vec{x}$ have values for the i^{th} of N bins in X_T and the j^{th} of M bins in X_L given by

$$x_{ij}^{\pm} = \frac{1}{2}\left(x_{ij} \pm x_{(N-i)(M-j)}\right). \tag{4.14}$$

4.5 Signal and Background Modeling

Simulation samples are used to construct signal and background templates, except for the multijet background, which is modeled dynamically from a control data sample. All simulation samples, listed in Table 4.1, have been prepared by the CMS collaboration for 8 TeV pp collisions.

Event generators are used to calculate kinematic distributions of each process assuming initial state partons with longitudinal momentum parametrized by parton density functions (PDFs) of the proton, and no transverse momentum. The assumption of no transverse momentum is addressed by a Monte Carlo technique based on the PDFs called showering, which is often combined with a simulation of the underlying proton collision. All the simulation samples in this analysis use Pythia [68–70] to calculate initial and final state showering and simulate the underlying event, as well as to calculate hadronization of final state quarks into jets. The detection of particles generated by these calculations is fully simulated with Geant [71] and a detailed model of the CMS detector.

The simulation samples are treated according to CMS collaboration recommendations to better match observed features in the data. Simulation events are reweighted to match the observed distribution of the number of interactions per LHC bunch-crossing (pileup), and the efficiency of the lepton triggers and reconstruction. The energy difference between each reconstructed jet in simulation and

Process	σ (pb)	Events (10^6)	Generator	Order	Note
$pp \to t\bar{t}$	211	28.15	Powheg	NLO	CT10 PDF set
$pp \to W + 1$ jet	5400	23.14	MadGraph	LO	
$pp \to W + 2$ jets	1750	34.04	MadGraph	LO	
$pp \to W + 3$ jets	519	15.54	MadGraph	LO	
$pp \to W + 4$ jets	214	13.38	MadGraph	LO	
$pp \to Z, \gamma^* + 1$ jet	561	24.05	MadGraph	LO	$m_{Z,\gamma^*} > 50\,\mathrm{GeV/c^2}$
$pp \to Z, \gamma^* + 2$ jets	181	21.85	MadGraph	LO	$m_{Z,\gamma^*} > 50\,\mathrm{GeV/c^2}$
$pp \to Z, \gamma^* + 3$ jets	51	11.02	MadGraph	LO	$m_{Z,\gamma^*} > 50\,\mathrm{GeV/c^2}$
$pp \to Z, \gamma^* + 4$ jets	23	6.40	MadGraph	LO	$m_{Z,\gamma^*} > 50\,\mathrm{GeV/c^2}$
$pp \to t$ (s-channel)	3	0.26	Powheg	NLO	
$pp \to t$ (t-channel)	47	3.76	Powheg	NLO	
$pp \to tW$	11	0.50	Powheg	NLO	
$pp \to \bar{t}$ (s-channel)	2	0.14	Powheg	NLO	
$pp \to \bar{t}$ (t-channel)	25	1.94	Powheg	NLO	
$pp \to \bar{t}W$	11	0.49	Powheg	NLO	

Table 4.1: Samples of simulated events. Hadronic showering for all samples is calculated with Pythia.

its corresponding generator jet is scaled to match the observed jet energy resolution in data, according to the jet pseudo-rapidity and transverse momentum. The systematic effects of these treatments on the final results are investigated appropriately.

4.5.1 Signal templates

The $t\bar{t}$ signal templates are constructed from simulation generated with the POWHEG-BOX heavy quark pair production [72], using the CT10 PDF set [73]. This is a calculation of top quark pair production in the Standard Model at next-to-leading order. The initial state composition and their intrinsic charge asymmetries in the POWHEG calculation, using a classification threshold of 20 GeV/c, are listed in Table 4.2. The sensitivity of these values to the choice of threshold is shown by comparison with an alternative classification scheme using a threshold of 30 GeV/c in Table 4.3. A plot of the transverse momentum of the recoiling quark for $t\bar{t}q$ events prior to any selection requirements, in Figure 4.2, shows that internal generator threshold effects are important below about 20 GeV/c. The symmetric and antisymmetric components of the joint probability distribution (X_T, X_L) prior to any selection requirements are shown for each initial state in Figures 4.3 and 4.4.

4.5.2 Background templates

Templates for the important backgrounds of $t\bar{t}$ lepton+jets selection are constructed from simulation and data control samples. Processes contributing to W+jets and Drell-Yan are generated with MADGRAPH [74]. Single Top processes are generated with the POWHEGBOX in the s and t channel [75], and in the tW channel with Diagram Removal rather than Diagram Subtraction [76].

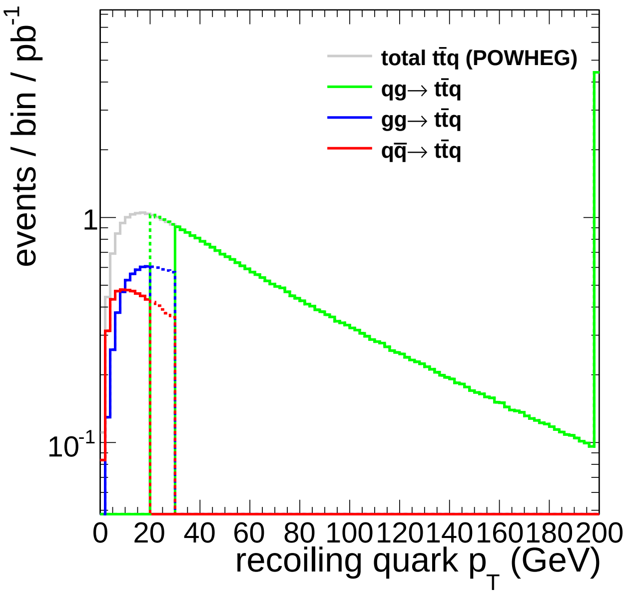

Figure 4.2: Transverse momentum of the recoiling light quark for Powheg generated $t\bar{t}q$ events. Initial state classification depends on the value of this observable. Two possible thresholds, 20 GeV/c and 30 GeV/c, are shown here.

	(%)		
Initial State	Fraction	$\hat{A}_c^{\phi}$	$\hat{A}_c^{y}$
gg	65.186(10)	0.03(3)	-0.06(3)
$q\bar{q}$	13.387(7)	0.31(6)	2.95(6)
qg	18.199(8)	3.77(5)	1.17(5)
$\bar{q}g$	3.226(4)	-4.4(1)	-0.2(1)
pp	100.0	0.60(2)	0.56(2)

Table 4.2: The fractions and intrinsic $t\bar{t}$ charge asymmetries of $t\bar{t}$ production processes, calculated with Powheg using the CT10 PDF set and a classification threshold of 20 GeV/c. Statistical uncertainty on the last digit is in parentheses.

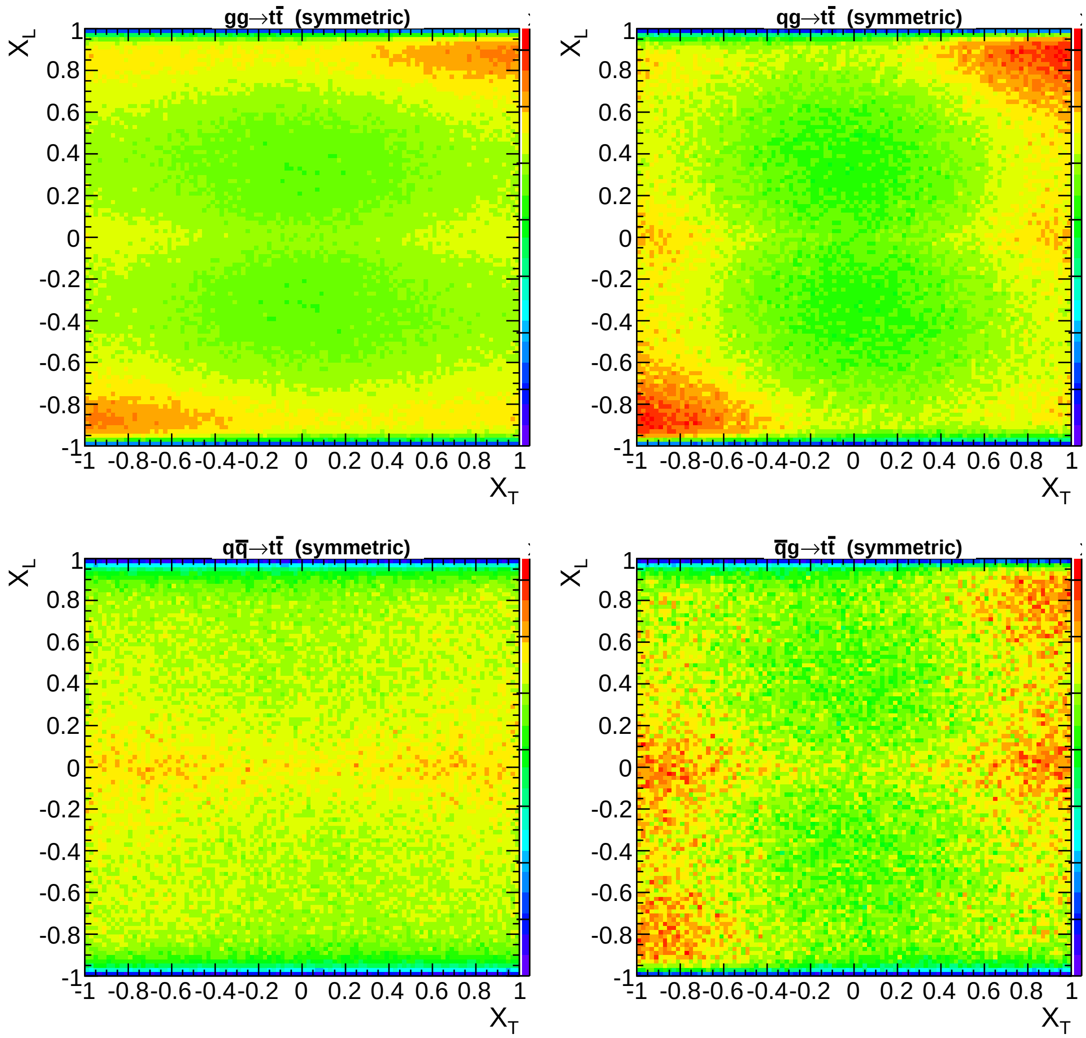

Figure 4.3: Symmetric components of the joint probability distributions in (X_T, X_L), for each initial state classification producing top quark pairs. Scales are linear and of equal range across classifications, starting from zero.

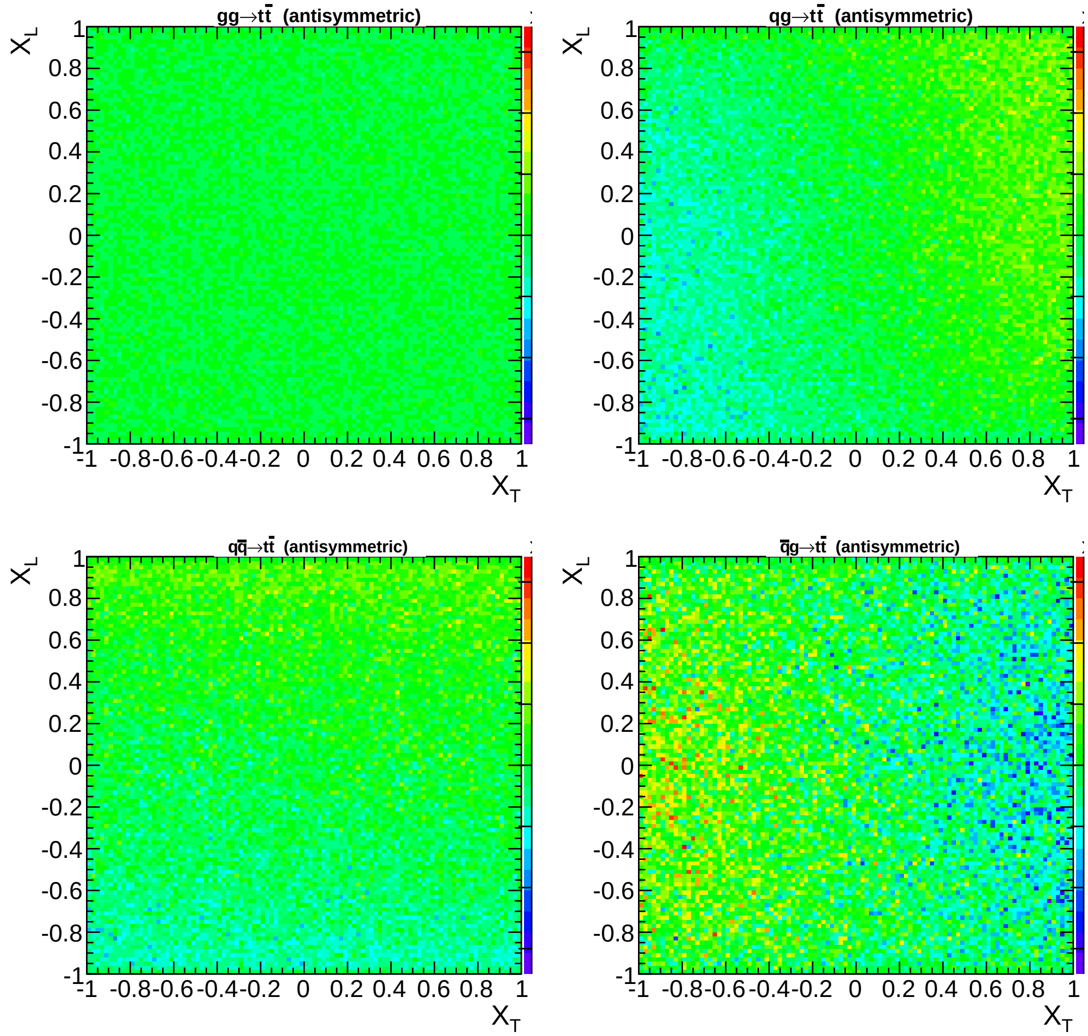

Figure 4.4: Antisymmetric components of the joint probability distributions in (X_T, X_L), for each initial state classification producing top quark pairs. Scales are linear and of equal range across classifications, centered at zero.

Threshold	(%) $\hat{f}_{\mathrm{gg}}$	$\hat{f}_{\mathrm{q\bar{q}}}$	$\hat{f}_{\mathrm{qg}}$	$\hat{f}_{\mathrm{\bar{q}g}}$	$\hat{A}_c^{y[\mathrm{q\bar{q}}]}$	$\hat{A}_c^{y[\mathrm{qg}]}$	$\hat{A}_c^{\phi[\mathrm{q\bar{q}}]}$	$\hat{A}_c^{\phi[\mathrm{qg}]}$
20 GeV/c	65.2	13.4	18.2	3.2	2.95	1.17	0.31	3.77
30 GeV/c	66.9	14.4	15.9	2.8	3.02	1.07	0.55	3.94

Table 4.3: POWHEG fractions and intrinsic $\mathrm{t\bar{t}}$ charge asymmetries in $\mathrm{t\bar{t}}$ production processes under two distinct classification thresholds.

The multijet background has a very low selection efficiency, which makes it expensive to simulate, but a large enough cross section to make it a significant background, so it cannot be ignored. Instead of using simulation, the template is constructed by subtracting the contributions of simulated processes from a data control sample with an inverted lepton isolation requirement, which has a high contribution from multijet events. Since the shape of the multijet background template depends on the estimated contributions from other processes, it varies with model parameters which describe those contributions. For example, an increased cross section for W+jets processes implies both a greater contribution of the W+jets template in the signal region as well as a correspondingly greater amount of W+jets template subtracted from data in the control sample construction of the multijet template.

5 Reconstruction and Selection

Events are selected from $19.6\,\mathrm{fb}^{-1}$ of data collected by the CMS experiment in 2012, from LHC collisions of protons at $8\,\mathrm{TeV}$ center of mass energy. The algorithms used to reconstruct the energy, momentum, and type of the debris particles in each event are discussed in Section 5.1. Selection criteria, enumerated in Section 5.2, are imposed to select as many $\mathrm{t\bar{t}}$ events as possible while limiting the selection of background process events. Section 5.3 describes the construction of top quark and antiquark kinematic hypotheses in selected events. Section 5.4 defines and characterizes a discriminating observable for use in measuring the sample composition.

5.1 Basic Reconstruction

Dedicated CMS collaboration software combines the raw data from the detector into a series of objects with successively increased scope and refinement. In the strip tracker for example, signals from individual channels on each module are combined into clusters with a position. Subsequently, tracks of charged particles are identified from the list of positions. Similar algorithms find tracks independently in the pixel detector and the muon chambers. Tracks are matched across subdetectors to improve the transverse momentum resolution and unify the description of charged particle tracks in the event. Collision vertices are identified as points near the beamline where many tracks intersect, and secondary vertices from the decay of unstable debris particles are identified similarly from tracks intersecting at points displaced from the beamline. Likewise, data from the calorimeters is clustered locally before being combined across subdetectors. Subsequent reconstruction steps combine tracking and calorimeter information to identify basic physics objects, consisting of a type, like electron, muon, or jet; a Lorentz vector, or relativistic description of momentum and energy; and other attributes, like charge and vertex of origin. There are two approaches.

The simpler approach is to define physics objects modularly. This can work well for analyses which primarily use just one type of physics object, like a dijet resonance search, but leads to inconsistencies and complications for analyses like this one which use many types of physics objects. For example, with modular definitions an electron and a jet might intersect on a common energy deposit, resulting in an inconsistent event description.

The alternative approach used for this analysis is known as Particle Flow, the goal of which is to provide a global, consistent event description with improved jet resolution [77, 78]. It proceeds by pooling all tracking and calorimetry information, and removing the corresponding information from the pool as each successive physics object is identified. Muons relevant to the analysis are identified with priority and their corresponding tracks and energy deposits are removed from the pool. Electrons relevant to the analysis are identified secondarily, and their tracks and energy deposits are removed as well. As subsequent particle candidates are identified and their contributions are removed from the pool, each candidate's Lorentz vector is added to a list for later clustering into jets: muon and electron candidates, which have failed relevancy criteria; charged hadron candidates, identified by their tracks and associated energy deposits in the calorimeters; neutral hadron candidates, identified by the residual HCAL deposits; and photons, identified by residual ECAL deposits. The transverse momentum imbalance, $E_{\mathrm{T}}^{\mathrm{miss}}$, is the negative sum of muon, electron, and corrected jet transverse momenta.

A relevant muon is one with a transverse momentum of at least 10 GeV/c and an absolute pseudorapidity less than 2.5, with a good track in the inner tracking system and a consistent energy deposit in the calorimeters. It must also be moderately isolated, which means that it carries at least a moderate fraction of the total momentum in its neighborhood. Signal muons are a subset of relevant muons which have transverse momentum of at least 26 GeV/c and absolute pseudorapidity less than 2.1. Each signal muon must also have a good track in both the inner tracking and muon systems, which crosses within 2 mm transverse (5 mm longitudinally) to the primary collision vertex.

A relevant electron is one with a transverse momentum of at least 20 GeV/c, an absolute pseudorapidity less than 2.5, no missing hits in its track, and moderate relative isolation. It must also have no opposite charged partner track, which is a hallmark of photon conversion, and it must pass a multivariate discriminator which includes information about the quality of the track, the shape of the calorimeter deposits, and the relative fraction of energy deposited in ECAL and HCAL. Signal electrons are a subset of relevant electrons which have transverse momentum of at least 30 GeV/c, and a track that passes within 0.2 mm transverse to the primary collision vertex. Electrons with ECAL deposits in the transition region between the barrel and the endcap cannot be signal electrons.

Jet clustering proceeds in several stages. Usually between 10 and 30 proton collisions occur in a single bunch crossing, so there are many charged particle tracks and energy deposits not associated with the primary vertex of interest. The first step in jet clustering is to correct the list of Lorentz vectors to be clustered by removing items not associated with the primary vertex, which can only be done for candidates with tracks. The remaining particle candidates are clustered into jets using the anti-$\mathrm{K_T}$ algorithm, with a cone parameter of 0.5 [79]. A series of energy corrections are subsequently applied to the jets. In the first correction, energy equal to the product of the jet area and the background energy intensity from extra collisions in the event is subtracted from each jet. The second correction, based on simulation, flattens the jet energy response as a function of pseudorapidity. The third correction, also based on simulation, flattens the jet energy response as a function of transverse momentum, so that the corrected energy is equal to the known energy of the jet being simulated. Residual energy corrections for differences between data and simulation are derived from observations of the Z boson dijet resonance in data [80, 81], and are only applied to jets in data. Defining jets from particle candidates, which incorporate track information, results in a significant advantage in resolution compared to the alternative of defining jets only from calorimeter energy deposits. All jets with transverse momentum greater than 10 GeV/c are used to define $E_{\mathrm{T}}^{\mathrm{miss}}$, but only jets meeting loose quality criteria with transverse momentum greater than 20 GeV/c in a pseudorapidity range $|\eta| < 2.5$ are considered relevant for further analysis.

Jets from b-quarks exhibit characteristics distinct from those of gluon or light quark jets. Since a b-quark must decay through a generation changing weak interaction, it has a long lifetime and is displaced from the primary vertex by the time it decays, leading to a track pattern in the associated jet indicating the secondary vertex. The high mass of the b-quark also leads to higher invariant mass of the associated jet, with a greater constituent multiplicity and greater transverse momentum of the constituents transverse to the jet axis. These characteristics are exploited by CMS to define b-jet discriminators, or b-taggers [82]. This analysis uses the Complex Secondary Vertex (CSV) b-tagger.

5.2 Event Selection

The selection criteria are based on recommendations of the CMS collaborations for $t\bar{t}$ events with a lepton+jets signature. A small number of events with probable fake or mismeasured energy deposits are rejected with a series of filters, due to concern about the reliability of their $E_{\mathrm{T}}^{\mathrm{miss}}$. Selected events contain exactly one signal electron or muon and no other relevant charged leptons, and at least four jets. At least one of the jets must have corrected transverse momentum greater than 45 GeV/c, and at least one other of the jets must have corrected transverse momentum greater than 35 GeV/c. At least one jet must be b-tagged, as defined by the medium working point of the Combined Secondary Vertex b-tagger (CSVM). A more stringent relative isolation is required of the signal lepton for the main selection, and a control sample with a higher contribution of multijet events is selected from the discarded events. Finally, each selected event must have been originally identified by the corresponding single lepton trigger, which has an approximate p_{T} threshold of 27 GeV/c (24 GeV/c) for electrons (muons), and a non-uniform efficiency in pseudorapidity and the relative isolation. A total of 326185 (340911) events are selected in the electron (muon) plus jets channel, and the number of events after each step in the selection are shown respectively in Tables 5.1 and 5.2.

In order to investigate dependence of results on the reconstructed $t\bar{t}$ system rapidity ($y_{t\bar{t}}$) and invariant mass ($m_{t\bar{t}}$), the measurement is repeated on four subsamples, with $m_{t\bar{t}}^{\mathrm{rec}}$ less than or greater than 450 GeV/c^2, or with $\tanh|y_{t\bar{t}}^{\mathrm{rec}}|$ less than or greater than 0.5 ($\tanh^{-1} 0.5 \approx 0.55$). The number of events in each subselection are shown in Tables 5.1 and 5.2.

	Events (10^3)	Selection Efficiency (%) $t\bar{t}$	W	ST	DY
	270308.415				
E_T^{miss} cleaning	268996.118	~100	~100	~100	~100
1 signal e, 0 μ	75484.704	1.37(1)	2.02(1)	0.54(3)	1.44(2)
j0: $p_T > 45\,\mathrm{GeV/c}$	15118.043	97.38(1)	32.81(2)	83.41(6)	45.77(3)
j1: $p_T > 35\,\mathrm{GeV/c}$	4406.851	93.18(2)	27.27(3)	65.86(9)	33.99(3)
j2: $p_T > 20\,\mathrm{GeV/c}$	2771.986	93.74(2)	49.41(4)	69.0(1)	54.63(5)
j3: $p_T > 20\,\mathrm{GeV/c}$	1298.253	76.83(3)	35.31(5)	50.1(2)	38.09(5)
b-tag (CSVM)	438.558	84.95(3)	12.56(5)	77.6(2)	13.64(5)
electron isolation	383.890	96.06(2)	96.24(7)	96.36(9)	96.39(7)
electron trigger	326.185	86.63(3)	84.2(1)	87.2(2)	85.7(1)
$\tanh\lvert y_{t\bar{t}}\rvert > 0.5$	147.026	45.91(5)	44.4(2)	43.5(3)	49.0(2)
$m_{t\bar{t}} > 450\,\mathrm{GeV/c^2}$	184.989	56.40(5)	60.1(2)	57.6(3)	54.7(2)
isolation sideband	42.997	2.87(1)	2.68(6)	2.70(8)	NA
electron trigger	18.792	44.7(3)	45 (1)	46 (1)	
$\tanh\lvert y_{t\bar{t}}\rvert > 0.5$	9.551	50.7(4)	49 (2)	47 (2)	
$m_{t\bar{t}} > 450\,\mathrm{GeV/c^2}$	10.91	51.2(4)	57 (2)	50 (2)	

Table 5.1: Electron plus jets selections and selection efficiencies. The signal and control samples are differentiated by the isolation requirement.

	Events (10^3)	Selection Efficiency (%) $t\bar{t}$	W	ST	DY
	239706.711				
$E_{\mathrm{T}}^{\mathrm{miss}}$ cleaning	233608.706	~100	~100	~100	~100
1 signal μ, 0 e	93983.545	1.59(1)	2.93(1)	0.69(3)	1.12(2)
j0: $p_{\mathrm{T}} > 45\,\mathrm{GeV/c}$	11740.928	97.28(1)	30.15(2)	82.45(6)	39.87(3)
j1: $p_{\mathrm{T}} > 35\,\mathrm{GeV/c}$	3451.877	93.08(2)	26.87(3)	64.96(8)	31.86(4)
j2: $p_{\mathrm{T}} > 20\,\mathrm{GeV/c}$	2035.907	93.68(2)	49.01(4)	68.3(1)	53.10(5)
j3: $p_{\mathrm{T}} > 20\,\mathrm{GeV/c}$	942.565	76.54(3)	35.06(4)	49.2(1)	37.88(6)
b-tag (CSVM)	445.036	84.99(3)	12.59(4)	77.9(2)	14.31(6)
muon isolation	374.967	93.73(2)	94.66(8)	94.2(1)	94.8(1)
muon trigger	340.911	90.54(2)	88.6(1)	90.5(1)	89.7(1)
$\tanh\|y_{t\bar{t}}\| > 0.5$	152.720	46.32(4)	43.9(2)	44.1(2)	48.3(2)
$m_{t\bar{t}} > 450\,\mathrm{GeV/c^2}$	188.498	55.75(4)	58.8(2)	57.1(2)	53.9(2)
isolation sideband	61.195	5.10(2)	4.32(7)	4.8(1)	NA
muon trigger	27.019	74.4(2)	74.5(8)	72.1(9)	
$\tanh\|y_{t\bar{t}}\| > 0.5$	12.542	46.4(2)	47 (1)	46 (1)	
$m_{t\bar{t}} > 450\,\mathrm{GeV/c^2}$	12.646	46.9(2)	48 (1)	46 (1)	

Table 5.2: Muon+jets selections and selection efficiencies. The signal and control samples are differentiated by the isolation requirement.

5.3 Reconstruction of Top Quarks

Reconstruction of the top quark and antiquark energies and momenta involves three stages. First, all possible jet assignments in the role of $t\bar{t}$ decay to lepton plus jets are considered, with the jet energies corrected to the parton level appropriately for each assignment. Second, one particular jet assignment is chosen. Third, the jet energies for the chosen assignment are allowed to float within their resolutions to best match the hypothesis of top decay kinematics. The final top quark and antiquark energies and momenta are found by summing the best fit energies and momenta of the assigned decay products. The charge of the leptonically decaying top is determined by the charge of the associated electron or muon, and the charge of the hadronically decaying top is assumed to be the opposite.

5.3.1 Parton level jet corrections

The relationship of the reconstructed jet energy to the energy of the parton which initiated the jet depends on the type of parton. Since jets from b-quarks tend to be wider than light quark jets, less of their energy falls within the jet cone. The nominal CMS jet energy corrections are derived from a sample containing mostly gluon and light quark jets, at a momentum transfer scale significantly lower than that associated with $t\bar{t}$ production. Consequently, improvement in the kinematic description of $t\bar{t}$ events can be achieved by applying additional jet energy corrections which take into account the expected jet flavors and momentum distributions. The application of flavor dependent jet corrections depends on the jet assignments chosen.

Parton level jet corrections are derived from the $t\bar{t}$ simulation after event selection for b-jets from top decay (B), jets from W boson decay (Q), or extra jets (N). Correction exponents are defined as the median log ratio of parton energy to nominally corrected jet energy, as a function of nominally corrected

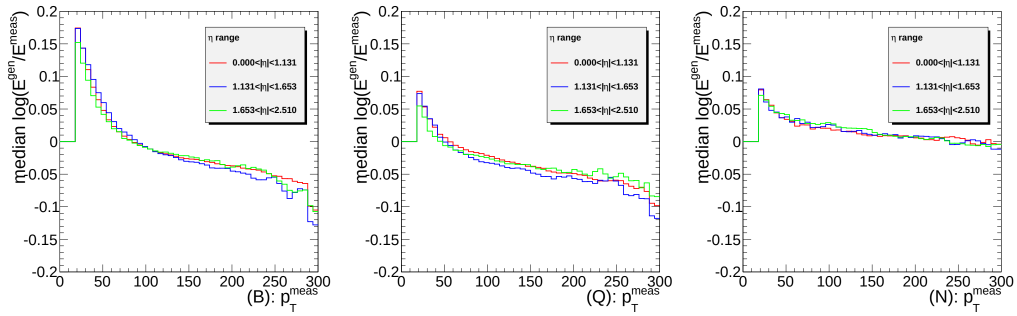

(a) (b) (c)

Figure 5.1: The median value of the log of the ratio of parton energy to nominally corrected jet energy, in selected $t\bar{t}$ events as a function of nominal jet transverse momentum in three bins of absolute pseudo-rapidity, for b-jets from top quark decay (a), for jets from W boson decay (b), and for other jets (c).

jet p_{T} in three bins of absolute pseudorapidity, with upper bin boundaries at $|\eta| \in \{1.131,\ 1.653,\ 2.51\}$ corresponding to transitions in calorimeter characteristics. The exponents are shown in Figure 5.1, and the corresponding corrections are applied to the nominally corrected jet energies according to assignment.

5.3.2 Jet assignments of maximum likelihood

Each event is considered under the hypothesis that a top quark and antiquark each decay to a b-jet and a W boson, and that one W boson subsequently decays to a pair of quarks, while the other decays to a neutrino and either an electron or a muon. The selection ensures that the number of jets in the event N_j is at least 4. There are N_j choices for the b-jet associated with the W decaying to leptons, $N_j - 1$ choices remaining for the b-jet associated with the W decaying to quarks, and $(N_j - 2)(N_j - 3)/2$ more options for the jets from decaying W, for a total number of assignment combinations

$$N_c = \frac{N_j!}{2(N_j - 4)!}. \tag{5.1}$$

There are at least 12 distinct assignment combinations. Let a combination be represented by the tuple (a, b, c, d, x^*), where a is the b-jet associated with leptonic top decay; b is the b-jet associated with hadronic top decay; c, d are the two jets from W boson decay ordered by p_{T}; and x^* are any additional jets in the event ordered by p_{T}. The correct choice of assignments in simulation is distinguished by the tuple with hats on same letters. The likelihood of each jet assignment combination is evaluated based on the value of the CSV b-tagger for each jet, the jet invariant masses m_{bcd} and m_{cd}, and the χ^2_a formed by the Lorentz vectors of the charged lepton, jet a, and $E_{\mathrm{T}}^{\mathrm{miss}}$ under the hypothesis of top decay.

The conditional CSV probability densities $\mathrm{CSVB} = \rho(\mathrm{CSV}|\hat{a}, \hat{b})$, $\mathrm{CSVQ} = \rho(\mathrm{CSV}|\hat{c}, \hat{d})$, $\mathrm{CSVN} = \rho(\mathrm{CSV}|\hat{x}^*)$ are shown in Figure 5.2. The CSV-based likelihood of a jet assignment combination i is

$$L_i^{\mathrm{CSV}} = \mathrm{CSVB}_a \cdot \mathrm{CSVB}_b \cdot \mathrm{CSVQ}_c \cdot \mathrm{CSVQ}_d \cdot \prod_{j \in x^*} \mathrm{CSVN}_j. \tag{5.2}$$

The joint probability distribution of correctly assigned jet invariant masses $(m_{\hat{c}\hat{d}},\ m_{\hat{b}\hat{c}\hat{d}})$ is shown in Figure 5.3. The mean and variance of this distribution are calculated after removing the least valued bins integrating to 1% (tail), in order to approximate it as a two dimensional Gaussian, the standard deviations of which are shown as contours in Figure 5.3. The distance of a point from the center of this Gaussian, expressed in standard deviations, is denoted Mass Standard Deviations (MSD). Probability distributions of MSD for correct $(b = \hat{b}, c = \hat{c}, d = \hat{d})$ and incorrect assignments are shown in Figure 5.4a, and their ratio,

$$LR_i^{\mathrm{MSD}} = \rho(\mathrm{MSD}|b, c, d = \hat{b}, \hat{c}, \hat{d}) / \rho(\mathrm{MSD}|b, c, d \neq \hat{b}, \hat{c}, \hat{d}), \tag{5.3}$$

and is shown in Figure 5.4c.

The most compatible neutrino momentum solution is calculated from the momenta of the selected lepton and jet a, and the measured $E_{\mathrm{T}}^{\mathrm{miss}}$ [83]. The tension

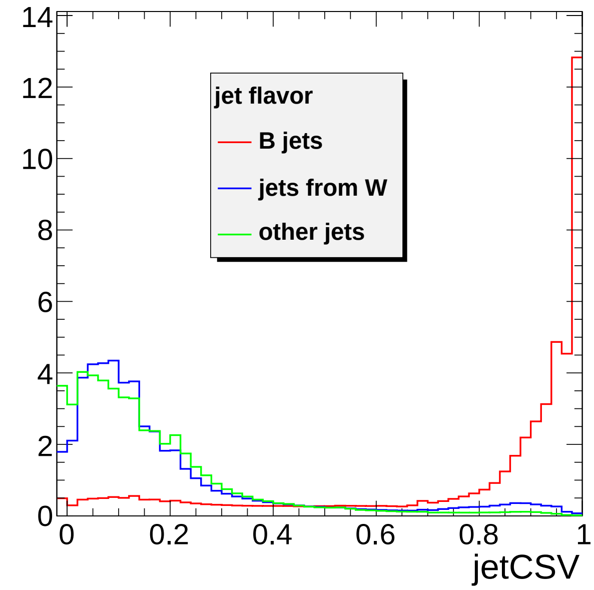

Figure 5.2: The conditional probability densities of the Combined Secondary Vertex b-tagging algorithm, given jets from b-quarks (red), jets from W boson decay (blue), or other jets (green).

between the solution and the measurement is

$$\chi_a^2 = \mathbf{d}^T \sigma^{-2} \mathbf{d}, \tag{5.4}$$

where σ^2 is the uncertainty matrix for $E_{\mathrm{T}}^{\mathrm{miss}}$ and $\mathbf{d}$ is the transverse displacement between $E_{\mathrm{T}}^{\mathrm{miss}}$ and the calculated neutrino momentum. The distribution of the square root of χ_a^2 is shown in Figure 5.4b for the correct jet assignment $a = \hat{a}$ and incorrect assignments $a \neq \hat{a}$, and their ratio LR^{χ} is shown in Figure 5.4d.

The combination of jet assignments chosen for $\mathrm{t\bar{t}}$ reconstruction is that with the maximum value of the likelihood

$$L_i = L_i^{\mathrm{CSV}} \cdot LR_i^{\mathrm{MSD}} \cdot LR_i^{\chi}. \tag{5.5}$$

Of selected $\mathrm{t\bar{t}}$ events, about half contain reconstructed jets corresponding to each of the jets $\hat{a}$, $\hat{b}$, $\hat{c}$, $\hat{d}$. In about 60% of those events, the assignment combination of maximum likelihood is also the correct combination.

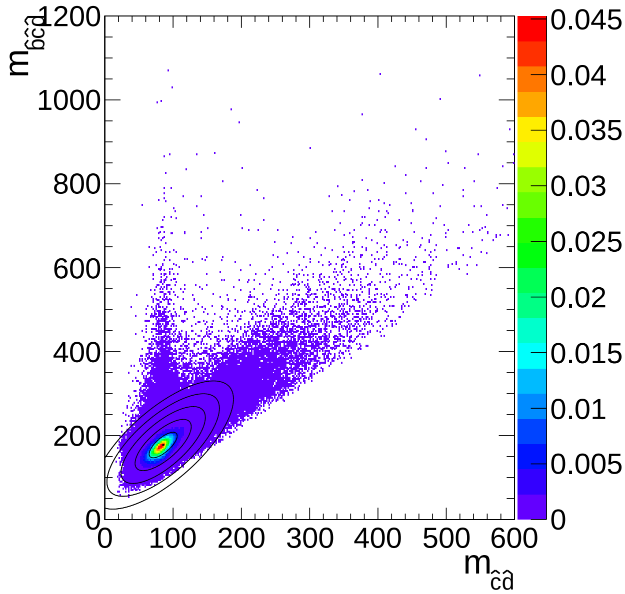

Figure 5.3: The joint probability distribution of correctly assigned jet invariant masses from W boson and top quark decay, along with integral contours of mass standard deviations (MSD) of the corresponding Gaussian approximation.

5.3.3 Kinematic fit

Application of constraints from the top quark mass and W boson mass allows the resolution of jet energies and $E_{\mathrm{T}}^{\mathrm{miss}}$ to be improved beyond the intrinsic resolution of the CMS detector. The constraints are applied in two stages by iterative least squares minimization.

In the first stage, the Lorentz vectors p_i of jets b, c, d are scaled with the free parameters $\vec{\delta}$,

$$\hat{p}_i = (1+\delta_i)p_i, \qquad i \in \{b, c, d\}, \tag{5.6}$$

in order to minimize the test statistic

$$\chi^2_{bcd} = \left(\frac{m_{\mathrm{W}} - \hat{m}_{cd}}{\Gamma_{\mathrm{W}}/2}\right)^2 + \left(\frac{m_{\mathrm{t}} - \hat{m}_{bcd}}{\Gamma_{\mathrm{t}}/2}\right)^2 + \sum_{i=bcd}\left(\frac{\delta_i}{r_i}\right)^2, \tag{5.7}$$

where r_i are the relative jet resolutions σ_E/E, dependent on jet transverse momentum and pseudorapidity. The masses and width parameters of the W boson

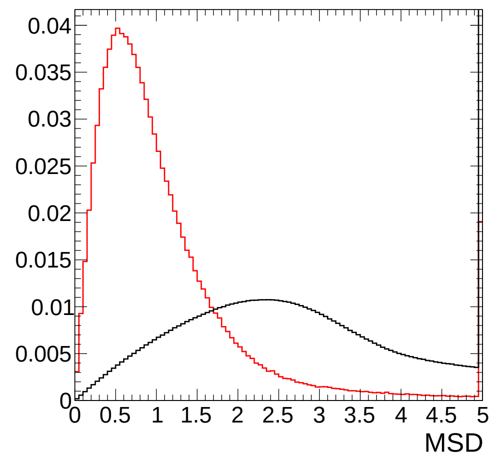

(a)

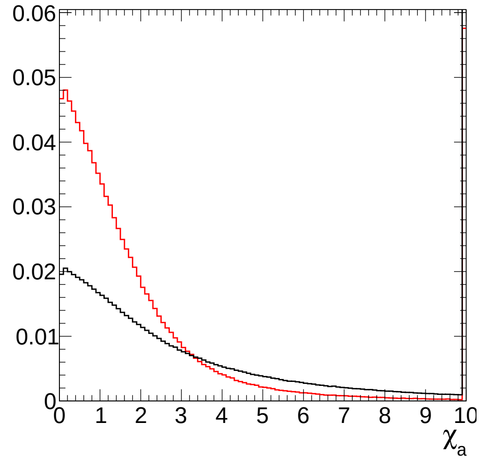

(b)

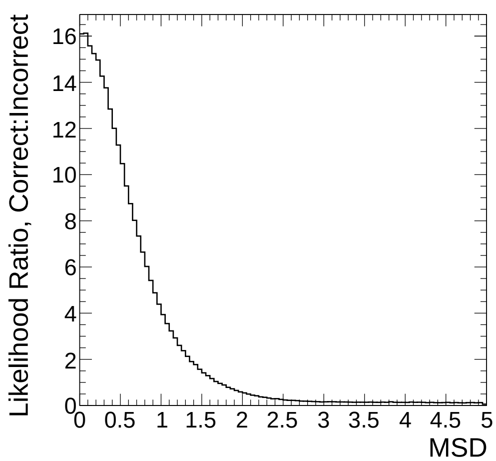

(c)

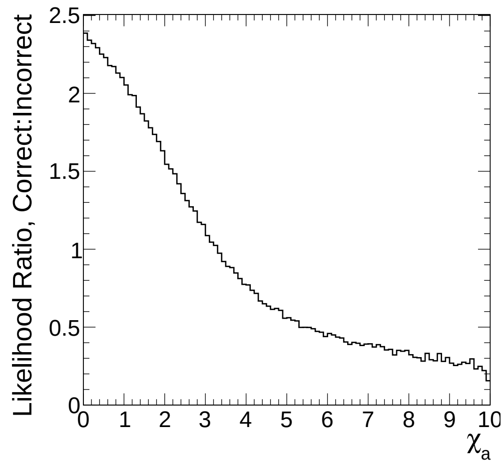

(d)

Figure 5.4: Probability densities for correct (red) and incorrect (black) jet assignments are shown for MSD (a) and for $\sqrt{\chi_a^2}$ of the leptonically decaying top reconstruction (b). The corresponding likelihood ratios are shown in (c) and (d).

and top quark used in the fit are: $m_{\mathrm{W}} = 80.4\,\mathrm{GeV/c^2}$; $m_{\mathrm{t}} = 172.0\,\mathrm{GeV/c^2}$; $\Gamma_{\mathrm{W}} = 2\,\mathrm{GeV/c^2}$; $\Gamma_{\mathrm{t}} = 13\,\mathrm{GeV/c^2}$. The values of Γ_{t} and Γ_W represent the expected resolution on the reconstructed particle masses for a single event, rather than their natural widths, which is why Γ_{t} is considerably greater than the natural width of the top quark. The momentum and energy of the hadronically decaying top (anti)quark are given by $\sum_{\{bcd\}} \hat{p}_i$.

In the second stage, the Lorentz vector p_a of jet a is scaled with the free parameter δ_a,

$$\hat{p}_a = (1 + \delta_a)p_a, \tag{5.8}$$

in order to minimize the test statistic χ^2_a, from Section 5.3.2. At each step of this minimization, χ^2_a is calculated with the charged lepton Lorentz vector, the corrected jet a Lorentz vector $\hat{p}_a$, and $E_{\mathrm{T}}^{\mathrm{miss}}$ corrected for the scaling of jets a, b, c, d. The uncertainty on the corrected $E_{\mathrm{T}}^{\mathrm{miss}}$ is reduced from that of the nominal reconstruction by removing a portion of the uncertainty due to the jets a, b, c, d. It was determined that tuning the factor of uncertainty reduction on $E_{\mathrm{T}}^{\mathrm{miss}}$ between 1 (all fit jet uncertainty removed) and 0 (no uncertainty reduction) does not strongly affect the fit; marginally better resolution was found for a factor of 0.55. The neutrino Lorentz vector associated with the minimized χ^2_a is summed with the corresponding $\hat{p}_a$ and the charged lepton Lorentz vector to find the energy and momentum of the leptonically decaying top (anti)quark.

5.3.4 Resolution

Resolution of the observables X_L and X_T is improved by the kinematic fit procedure. Resolution is determined from distributions of the residual difference between reconstructed and true values, shown in Figures 5.5 and 5.6. Since the residuals are not normally distributed, having wide tails and narrow cores, the quadratic mean (RMS) can be a misleading figure of merit for resolution. Two figures of merit for resolution are quoted: the RMS; and half the length of the shortest interval which covers 68% of the distribution (HSI). The HSI and RMS figures of merit coincide for Gaussian distributions.

5.4 Tridiscriminant

In order to measure the composition of the selected sample, it is necessary to have a discriminating observable. This first part of this section describes the construction of a discriminant between three populations which is a symmetric function of the likelihood ratios between each population pair. The second part specifies the likelihoods of the three event populations {$\mathrm{t\bar{t}}$, W+jets, multijets}, and characterizes the resulting tridiscriminant.

5.4.1 Construction

The likelihood that an event belongs to a population P, for the simple case of independent random variables $\{V_i\}$, is

$$L_P = \prod_i \ell_i^P,$$

where ℓ_i^P is the value of the probability density in V_i of population P. The ratio of the likelihoods of two populations P_1 and P_2 offers better discrimination between them than any V_i [84]. The random variable $\Lambda_0 = (1 + L_{P_2}/L_{P_1})^{-1}$ is a convenient transformation of the likelihood ratio, since it is bounded on $(0, 1)$ and is symmetric around 0.5 under exchange of the two populations $P_1 \leftrightarrow P_2$, with population $P_1(P_2)$ more concentrated towards 0(1). This transformation is not unique. More generally, the normalized principal value (pv) of the argument of $L_{P_1} + e^{i\phi} L_{P_2}$,

$$\Lambda_\phi = \text{pv Arg}(L_{P_1} + e^{i\phi} L_{P_2})/\phi, \tag{5.9}$$

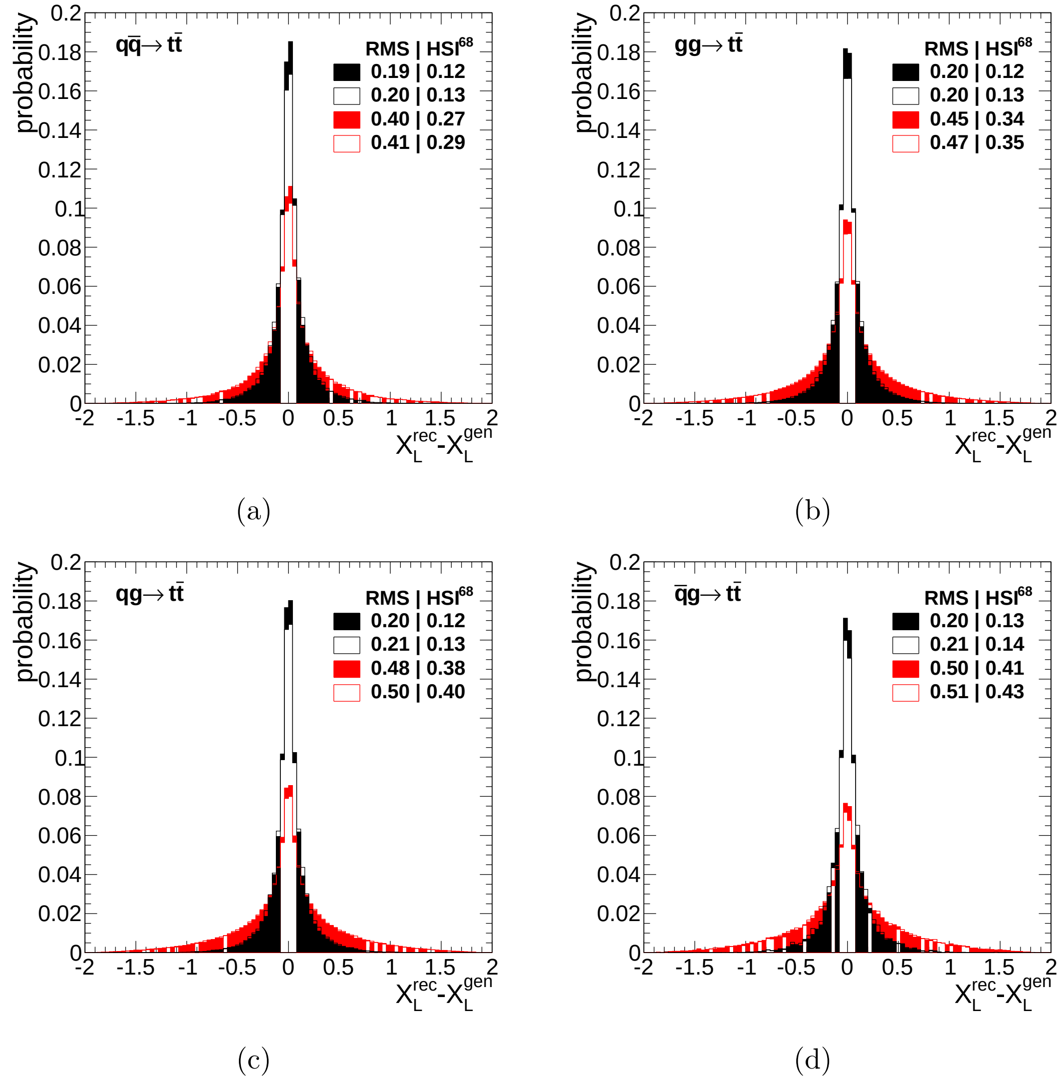

Figure 5.5: Residual distributions of the observable X_L in simulated $t\bar{t}$ events (combined electron and muon channels), for initial states $q\bar{q}$, gg, qg, and $\bar{q}$g. Red histograms show the residuals for the selected jet assignment, while black histograms show residuals for the subselection with correctly assigned jets. Filled (open) histograms show residuals after (before) the kinematic fit procedure. Two figures of merit are shown for each histogram: the quadratic mean (RMS); and half the shortest interval covering 68% probability (HSI).

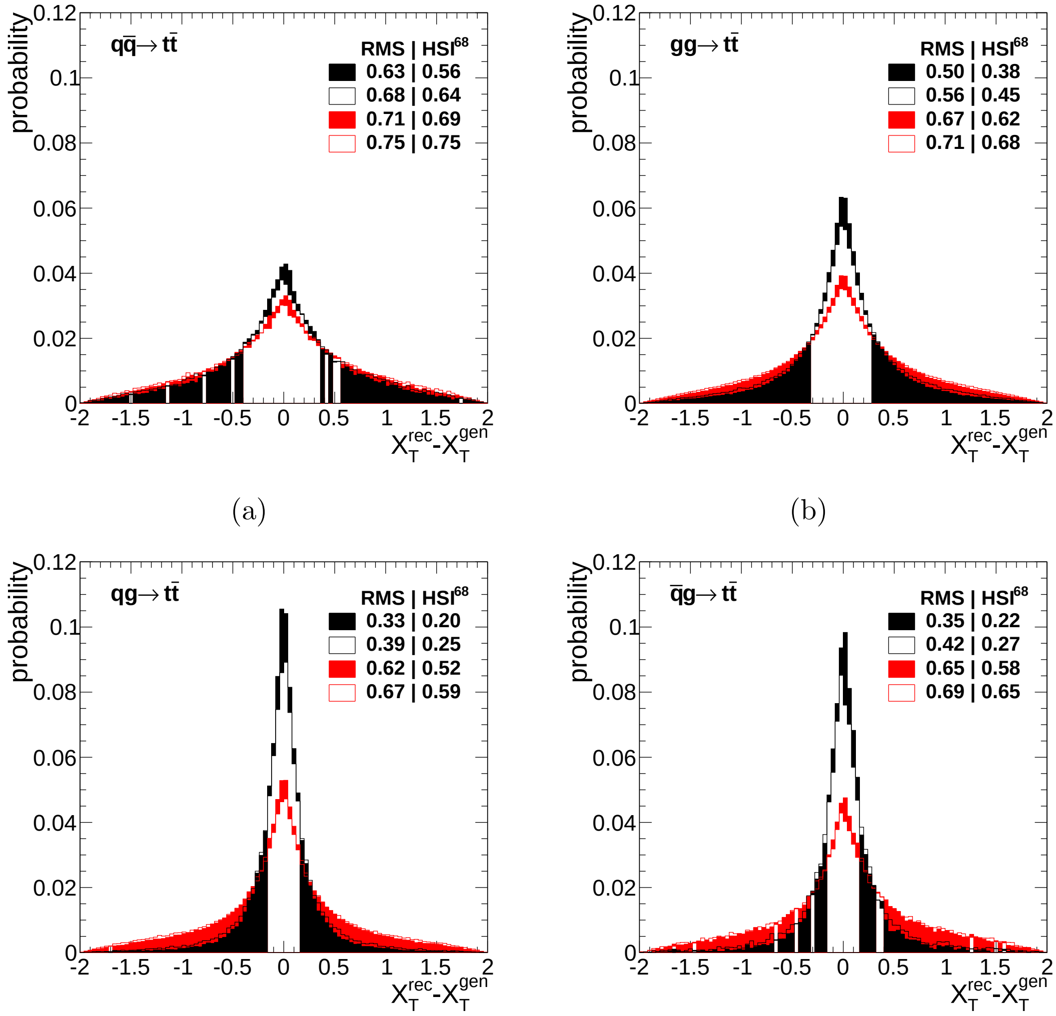

(a) (b) (c) (d)

Figure 5.6: Residual distributions of the observable X_T in simulated $t\bar{t}$ events (combined electron and muon channels), for initial states $q\bar{q}$, gg, qg, and $\bar{q}g$. Red histograms show the residuals for the selected jet assignment, while black histograms show residuals for the subselection with correctly assigned jets. Filled (open) histograms show residuals after (before) the kinematic fit procedure. Two figures of merit are shown for each histogram: the quadratic mean (RMS); and half the shortest interval covering 68% probability (HSI).

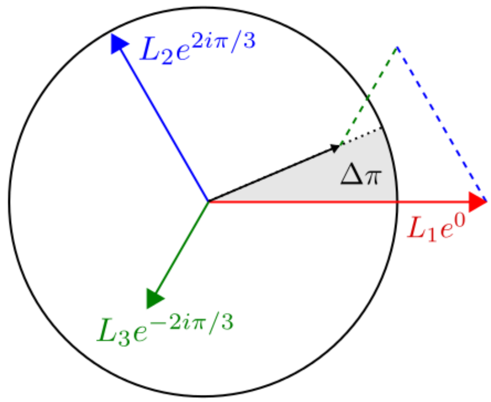

Figure 5.7: The angle $\Delta\pi$ of the resultant sum of three vectors spaced at equal angles. The magnitude of each vector is the likelihood of a corresponding population, and Δ is a likelihood discriminant between the three populations.

for arbitrary ϕ, is bounded on $(0, 1)$ and symmetric around 0.5 under the exchange $P_1 \leftrightarrow P_2$. Note that $\Lambda_0 = \lim_{\phi\to 0}\Lambda_\phi$. The opposite extreme to Λ_0 is Λ_π, which is binary valued on $\{0, 1\}$.

Following the generalization (5.9), it is possible to construct a similar discriminating random variable which is bounded periodically on [-1,1] and is symmetric under exchange of any two of the three populations, P_1, P_2, and P_3,

$$\Delta = \text{pv Arg}\left(L_{P_1} + e^{i\pi 2/3}L_{P_2} + e^{i\pi 4/3}L_{P_3}\right)/\pi. \tag{5.10}$$

In the case that the likelihood of one population is negligible, the tridiscriminant Δ essentially reduces to $\Lambda_{2\pi/3}$ between the other two. In the case that two populations have the same likelihood, Δ reduces to a binary valued discriminant against the third population, similar to Λ_π. Population $(P_1,\ P_2,\ P_3)$ tends to concentrate at $\Delta = (0,\ 2/3,\ -2/3)$. Figure 5.7 illustrates the tridiscriminant construction.

5.4.2 Inputs and performance

A tridiscriminant for the event populations $t\bar{t}$, multijet, W+jets is used in this analysis. Three observables contribute to the population likelihoods. The first is the transverse mass of the charged lepton and the unfit $E_{\mathrm{T}}^{\mathrm{miss}}$, defined as

$$M_{\mathrm{T}} = \sqrt{2p_{\mathrm{T}}^{\ell} E_{\mathrm{T}}^{\mathrm{miss}} \cdot (1 - \cos\phi)}, \tag{5.11}$$

where p_{T}^{ℓ} is the transverse momentum of the charged lepton and ϕ is the azimuthal angle between the charged lepton and $E_{\mathrm{T}}^{\mathrm{miss}}$. The second observable is the probability from Mass Standard Deviations (MSD) that at least one jet assignment is the correct one, defined as

$$P_{\mathrm{MSD}} = \frac{\sum LR_i^{\mathrm{MSD}}}{N_c + \sum LR_i^{\mathrm{MSD}}}, \tag{5.12}$$

where N_c and LR_i^{MSD} are defined in Equations (5.1) and (5.3). The last observable is the probability from the CSV b-tagging algorithm that at least one jet assignment is the correct one, defined as

$$P_{\mathrm{CSV}} = \frac{\epsilon \sum L_i^{\mathrm{CSV}}}{\epsilon \sum L_i^{\mathrm{CSV}} + (1-\epsilon) \prod_{j \in \{jets\}} \mathrm{CSVN}_j}, \tag{5.13}$$

where L_i^{CSV} and CSVN_j are defined in Equation (5.2), the prior probability of at least one correct assignment is ϵ, and only one of each pair of assignments with swapped jets $a \leftrightarrow b$ is included in the sums. A value of $\epsilon = 0.05$ was chosen because it results in a more even distribution of P_{CSV} than, for example, a flat prior with $\epsilon = 0.5$. These observables were chosen because they are highly discriminating and mostly independent of each other.

The probability distribution for each population is shown as a function of the tridiscriminant and of each of its input observables in Figure 5.8. The multijet probability densities are derived statically with Standard Model cross sections, rather than dynamically as in the model of Chapter 6. The power of an observable V to discriminate between two populations is given by the dilution,

$$D_V^{1,2} = \frac{1}{2} \int \frac{(\rho_1 - \rho_2)^2}{\rho_1 + \rho_2} \mathrm{d}V, \tag{5.14}$$

Dilutions (%)

	$\mathrm{t\bar{t}}$:W	$\mathrm{t\bar{t}}$:mj	W:mj
M_{T}	0.1	5.2	6.2
P_{MSD}	7.1	3.5	1.1
P_{CSV}	31.2	18.3	3.0
Δ	31.6	21.8	8.9

(a) e+jets.

	$\mathrm{t\bar{t}}$:W	$\mathrm{t\bar{t}}$:mj	W:mj
M_{T}	0.1	14.4	14.9
P_{MSD}	6.8	2.9	1.4
P_{CSV}	31.6	10.6	9.2
Δ	32.8	23.1	21.6

(b) μ+jets.

Table 5.3: Dilutions between population pairs for the tridiscriminant Δ and each input observable. Higher values of dilution, defined in Equation 5.14, correspond to better discrimination.

where ρ_1 and ρ_2 are the probability densities of V in the respective populations. Table 5.3 compares the discriminating power of the tridiscriminant and each input for each population pair.

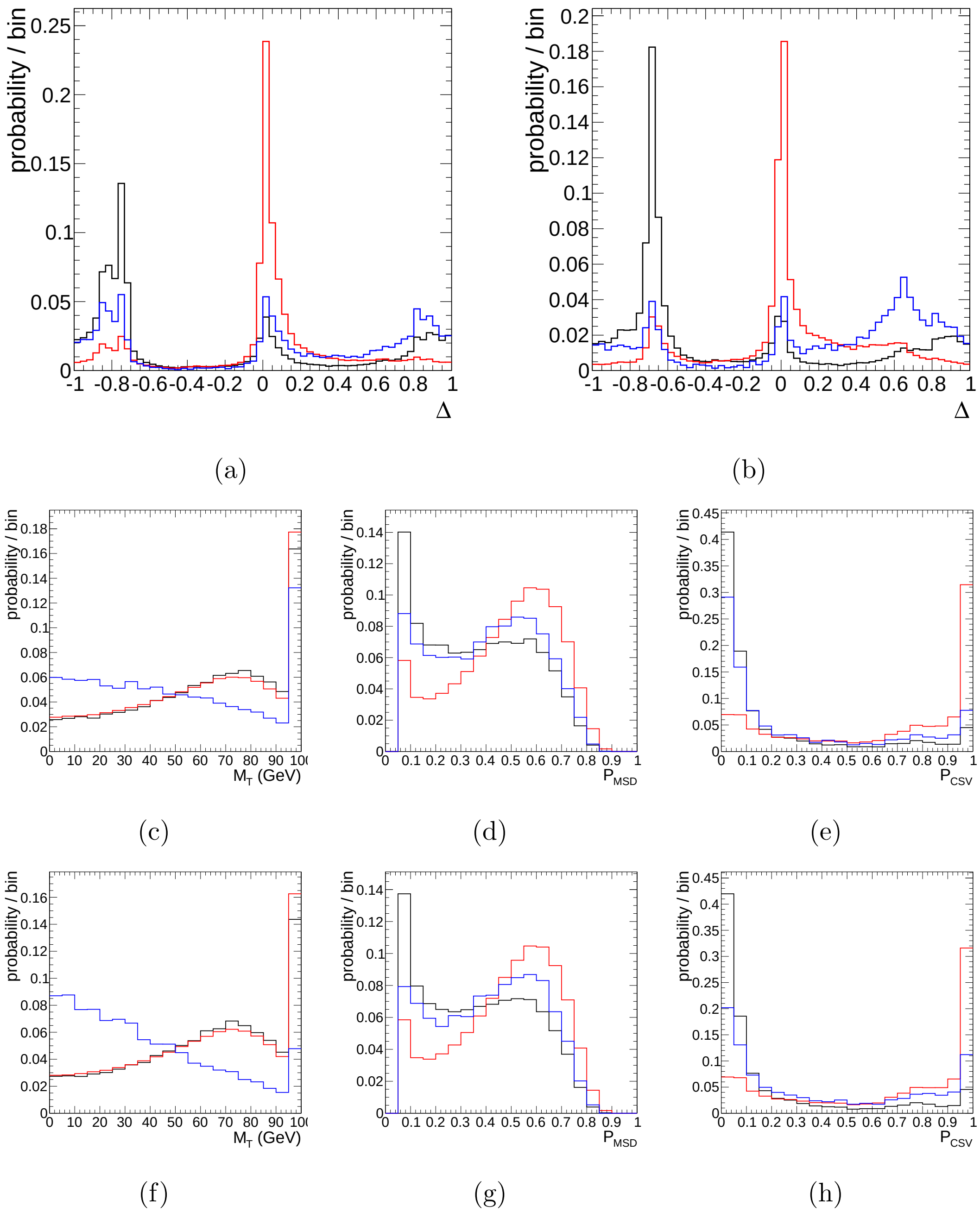

Figure 5.8: The probability distribution of the tridiscriminant Δ in the electron channel (a) and the muon channel (b), from the populations $t\bar{t}$ (red), multijets (blue), and W+jets (black). The probability distributions of each observable used to construct the tridiscriminant are shown for the electron channel (c,d,e) and the muon channel (f,g,h).

6 Measurement

The analysis employs an extended template model to measure the forward-central $\mathrm{t\bar{t}}$ charge asymmetry A_c^y from the contributions $A_c^{y(k)}$ of each $\mathrm{t\bar{t}}$ production process $k \in \{\mathrm{q\bar{q}},\ \mathrm{qg},\ \mathrm{\bar{q}g},\ \mathrm{gg}\}$, given by Equation 4.4. The $\mathrm{t\bar{t}}$ charge asymmetry in the base model is extended with two parameters, one for the antisymmetric component of $\mathrm{q\bar{q}}$ distributions, and one for the antisymmetric components of qg and $\mathrm{\bar{q}g}$ distributions; the gg process has a negligible antisymmetric component. As described in the last paragraph of Section 4.4, the $\mathrm{q\bar{q}}$ and qg initial state processes have distinct antisymmetric component shapes in the joint distribution of X_L and X_T, so a fit to the joint distribution allows discrimination of their contributions. The base model predicts negligible contributions to A_c^y from the gg and $\mathrm{\bar{q}g}$ initial states (Table 4.2). The sample composition is measured simultaneously with the asymmetry contributions by fitting to the joint distribution of the three observables X_L, X_T, and the tridiscriminant Δ. The template fit is performed by maximizing the model likelihood, given observations. The statistical uncertainty and the systematic uncertainties due to several nuisance parameters are found by profiling the likelihood. The remaining systematic uncertainties are estimated by reevaluating the best fit with varied inputs to the model.

6.1 Templates

Observations and template distributions are binned in three dimensions: the tridiscriminant Δ (5 bins); X_T^{rec} (5 bins); and X_L^{rec} (5 bins), for a total of 125 bins. Signal templates for each of the initial state classifications described in Section 4.2 are constructed from the POWHEG $\mathrm{t\bar{t}}$ simulation, described in Section 4.5.1. Templates for the background processes described in Section 4.3 are constructed from simulation and the data control sample, as described in Section 4.5.2. The measurement involves two lepton channels in both signal and control (isolation sideband) selections, for a total of four channels, $\ell \in \{e, \mu, e_{\mathrm{side}}, \mu_{\mathrm{side}}\}$. The normalized templates $\vec{x}_j^{\ell}$ represent the event probability distribution of $(\Delta, X_T^{\mathrm{rec}}, X_L^{\mathrm{rec}})$ for process j in channel ℓ. The probability in the i^{th} bin of $\vec{x}_j^{\ell}$ is x_{ij}^{ℓ}.

Recall from Equation 4.8 that non-zero reconstruction bias can have a constant component (M_0^-) and a component dependent on the fundamental asymmetry (M_1^-). Figures 6.1c and 6.1d show projections on X_L^{rec} and X_T^{rec} of $M^- = M_0^- + M_1^-$ operating on the symmetrized probability distribution of (X_T, X_L), for each of the $\mathrm{t\bar{t}}$ initial state classifications. The gg initial state, which has no intrinsic asymmetry, shows negligible reconstruction bias, consistent with zero. The $\mathrm{\bar{q}g}$ and qg initial states, which have opposite intrinsic A_c^{ϕ}, show opposite reconstruction bias in X_T. This is convincing evidence that the reconstruction has negligible constant bias M_0^-. Projections of the quadratic component of Equation 4.9, M^- operating on the antisymmetrized probability distribution of (X_T, X_L), are shown in Figures 6.1a and 6.1b, and are both clearly negligible. Since the constant reconstruction bias and the quadratic correction are negligible, Equation 4.10 can be used to describe extended models with parametrized asymmetry for each of the initial state classifications,

$$\vec{x}_k^{\ell}(\alpha_k) = \left(\vec{x}_k^{\ell}\right)^+ + \alpha_k \left(\vec{x}_k^{\ell}\right)^-, \qquad k \in \{\mathrm{gg}, \mathrm{q\bar{q}}, \mathrm{qg}, \mathrm{\bar{q}g}\} \tag{6.1}$$

where the templates are constructed simply by (anti)symmetrizing the POWHEG distribution of $(X_T^{\mathrm{rec}}, X_L^{\mathrm{rec}})$ in each bin of the tridiscriminant, according to Equation 4.14. Projections of the templates are shown in Figure 6.2. The template constructions (6.1) represent $(\Delta, X_T^{\mathrm{rec}}, X_L^{\mathrm{rec}})$ in a parametrization of Standard Model top quark pair production according to Powheg.

6.2 Model

The number of observed events in the i^{th} bin in channel ℓ is N_i^ℓ. The corresponding number of events expected from simulated signal or background process j is

$$\lambda_{ij}^\ell = \mathcal{L}^\ell \sigma_j \epsilon_j^\ell x_{ij}^\ell, \tag{6.2}$$

where $\mathcal{L}^\ell$ is the luminosity, σ_j is the cross section, ϵ_j^ℓ is the efficiency of selection, and the extended models (6.1) are used for the signal templates. The shape of the multijet background in each lepton channel is found by subtracting the other modeled processes from the data control sample, but the total multijet contribution to each signal channel is scaled by a positive free parameter $F_{(\mathrm{mj})}^\ell$. The number of expected multijet events in the i^{th} bin of channel $\ell \in \{e, \mu\}$ is

$$\lambda_{i(\mathrm{mj})}^\ell = F_{(\mathrm{mj})}^\ell \cdot \left(N_i^{\ell_{\mathrm{side}}} - \sum_{j \neq (\mathrm{mj})} \lambda_{ij}^{\ell_{\mathrm{side}}} \right). \tag{6.3}$$

The efficiencies of selection ϵ_j^ℓ are taken directly from simulation. The luminosity in the model is a factor $(1 + \delta_{\mathcal{L}})$ different than the central value of the measured luminosity $\hat{\mathcal{L}}$,

$$\mathcal{L}^\ell = (1 + \delta_{\mathcal{L}}) \hat{\mathcal{L}}^\ell. \tag{6.4}$$

The measured luminosities coincide for all channels, with $\hat{\mathcal{L}} = 19.6\,\mathrm{fb}^{-1}$. The cross sections for simulated processes in the model differ from their nominal values $\hat{\sigma}_j$ by a factor $(1 + \delta_j)$,

$$\sigma_j = (1 + \delta_j)\hat{\sigma}_j, \qquad j \in \{\mathrm{t\bar{t}},\ \mathrm{W},\ \mathrm{ST},\ \mathrm{DY}\}. \tag{6.5}$$

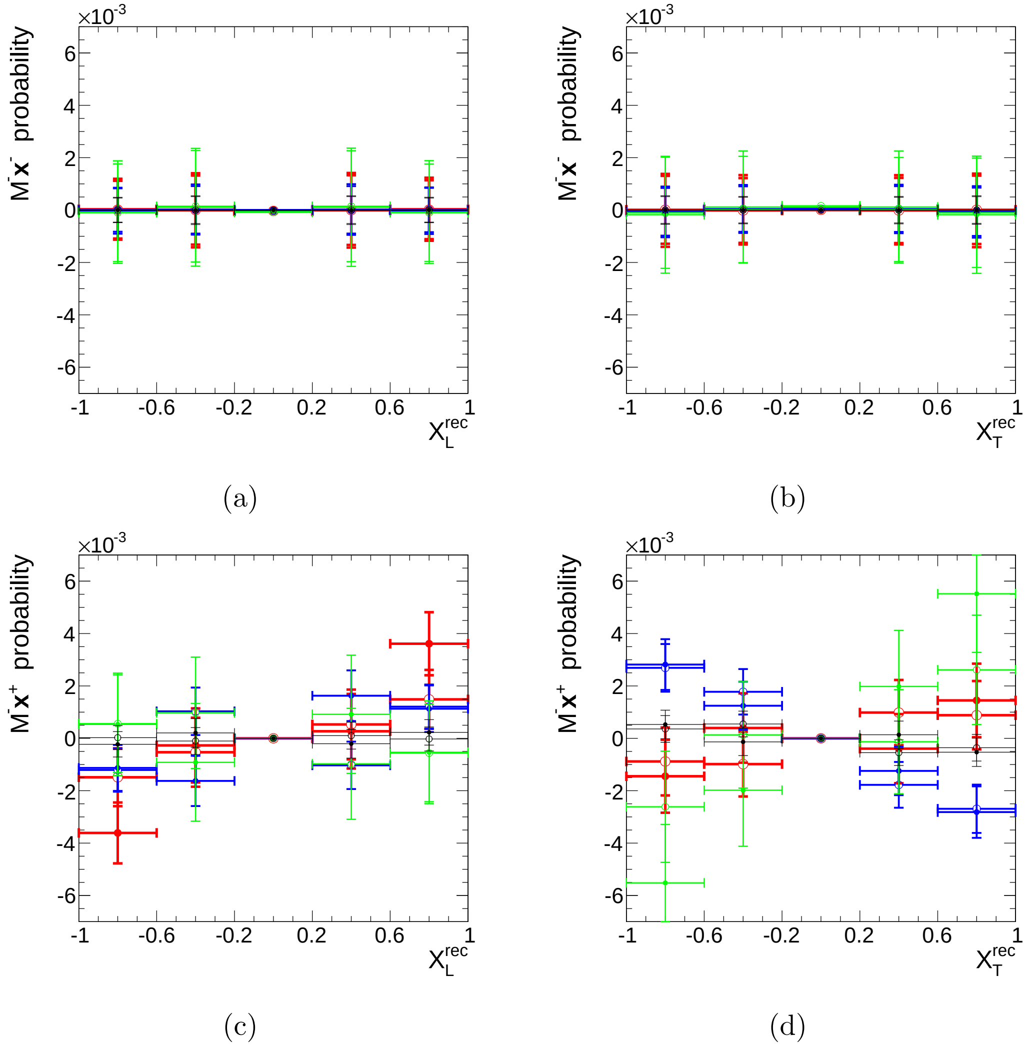

Figure 6.1: Projections on X_L^{rec} and X_T^{rec} of the template quadratic correction and the migration matrix bias, for each $\mathrm{t\bar{t}}$ initial state classification: $\mathrm{q\bar{q}}$ (red), qg (blue), $\mathrm{\bar{q}g}$ (green), and gg (black). Electron(muon)+jets channel is shown with solid(open) markers.

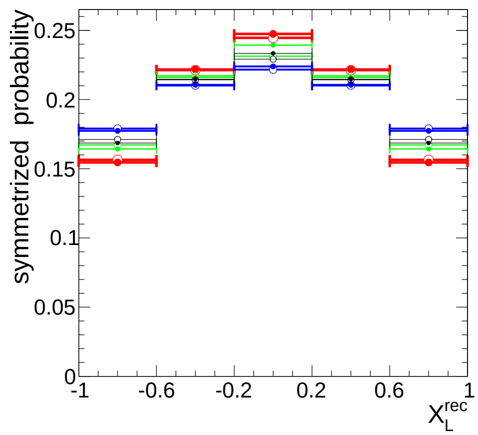

(a)

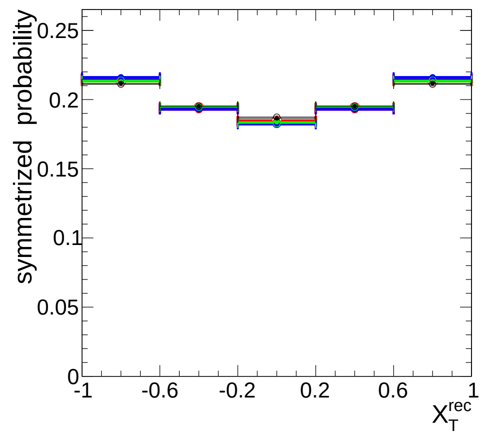

(b)

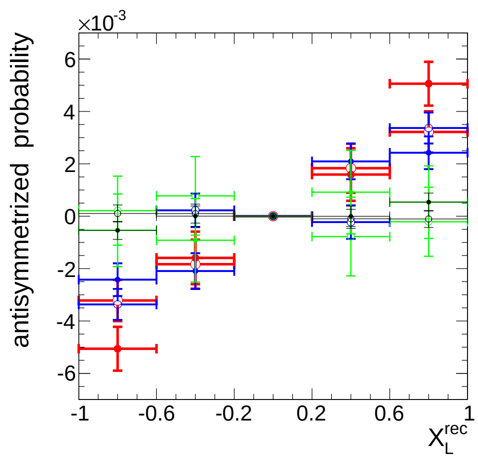

(c)

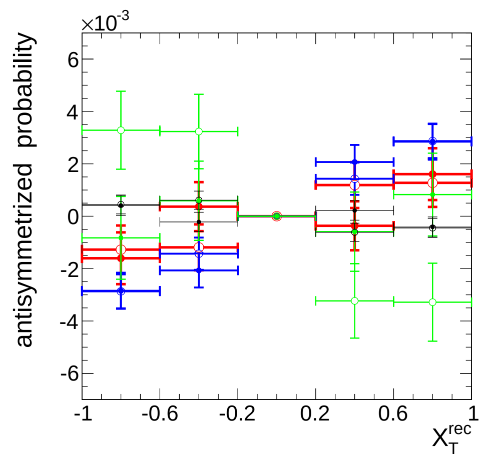

(d)

Figure 6.2: Projections on $X_L^{\rm rec}$ and $X_T^{\rm rec}$ of the (anti)symmetrized templates for each $t\bar{t}$ initial state classification: $q\bar{q}$ (red), qg (blue), $\bar{q}g$ (green), and gg (black). Electron(muon)+jets channel is shown with solid(open) markers.

Refer to Table 4.1 for the nominal cross sections. Expanding on Equation 4.4, the $\mathrm{t\bar{t}}$ initial state processes have cross sections

$$\sigma_{k\to\mathrm{t\bar{t}}} = f_k(1+\delta_{\mathrm{t\bar{t}}})\hat{\sigma}_{\mathrm{t\bar{t}}}, \qquad k \in \{\mathrm{gg}, \mathrm{q\bar{q}}, \mathrm{qg}, \mathrm{\bar{q}g}\}. \tag{6.6}$$

As noted in Section 4.1, the contribution of each $\mathrm{t\bar{t}}$ initial state to the total asymmetry in the extended model is a function of the product of the cross section fraction f_k and the parameter α_k of the extended model. The parameter α_{gg} is assumed to be 1, and the parameters α_{qg} and $\alpha_{\mathrm{\bar{q}g}}$ are assumed to be equal. The two fit parameters of interest are

$$\beta_{\mathrm{q\bar{q}}} = \alpha_{\mathrm{q\bar{q}}} \cdot f_{\mathrm{q\bar{q}}}, \tag{6.7}$$

$$\beta_{\mathrm{qg}} = \alpha_{\mathrm{qg}} \cdot f_{\mathrm{qg}}. \tag{6.8}$$

The four fractions f_k are allowed two degrees of freedom. They are defined with two parameters: $\delta_{\mathrm{q\bar{q}}}$, the percentage difference of $f_{\mathrm{q\bar{q}}}$ from the prediction; R, the ratio of $f_{\mathrm{\bar{q}g}}$ to $f_{\mathrm{q\bar{q}}}$; and two constraints:

$$\sum f_k = 1 \tag{6.9}$$

$$\frac{f_{\mathrm{qg}} f_{\mathrm{\bar{q}g}}}{f_{\mathrm{q\bar{q}}} f_{\mathrm{gg}}} = \frac{\hat{f}_{\mathrm{qg}} \hat{f}_{\mathrm{\bar{q}g}}}{\hat{f}_{\mathrm{q\bar{q}}} \hat{f}_{\mathrm{gg}}}. \tag{6.10}$$

The initial state fractions $\hat{f}_k$ calculated by POWHEG are listed in Table 4.2. The constraint (6.10) is motivated by the observation that it holds for a simplistic model in which all quark initial state densities can be scaled from the simulation by a free parameter, all antiquark initial state densities by another free parameter, and the gluon initial state density by a third free parameter. Note that any impreciseness in this constraint is ameliorated by the size of $f_{\mathrm{\bar{q}g}}$, which remains small; the three significant fractions can be well described by the remaining precise constraint and two degrees of freedom. With these parameters and constraints the fractions f_k can be expressed as

$$f_{\mathrm{q\bar{q}}} = (1+\delta_{\mathrm{q\bar{q}}})\hat{f}_{\mathrm{q\bar{q}}} \tag{6.11}$$

$$f_{\mathrm{\bar{q}g}} = R f_{\mathrm{q\bar{q}}} \tag{6.12}$$

$$f_{\mathrm{qg}} = (1 - f_{\mathrm{q\bar{q}}} - f_{\mathrm{\bar{q}g}})/(1 + R\hat{f}_{\mathrm{gg}}\hat{f}_{\mathrm{q\bar{q}}}/(\hat{f}_{\mathrm{qg}}\hat{f}_{\mathrm{\bar{q}g}})) \tag{6.13}$$

$$f_{\mathrm{gg}} = 1 - f_{\mathrm{q\bar{q}}} - f_{\mathrm{qg}} - f_{\mathrm{\bar{q}g}}. \tag{6.14}$$

The total number of expected events in each bin in each channel is

$$\lambda_i^\ell = \sum_j \lambda_{ij}^\ell, \qquad j \in \left\{ \begin{array}{c} \mathrm{q\bar{q}} \to \mathrm{t\bar{t}}, \quad \mathrm{gg} \to \mathrm{t\bar{t}}, \quad \mathrm{qg} \to \mathrm{t\bar{t}}, \quad \mathrm{\bar{q}g} \to \mathrm{t\bar{t}}, \\ \mathrm{W}, \quad (\mathrm{mj}), \quad \mathrm{ST}, \quad \mathrm{DY} \end{array} \right\}, \tag{6.15}$$

where λ_{ij}^ℓ are defined in Equations (6.2) and (6.3). The parameters of the model are $\beta_{\mathrm{q\bar{q}}}$, β_{qg}, $\delta_{\mathrm{q\bar{q}}}$, R, $F^e_{(\mathrm{mj})}$, $F^\mu_{(\mathrm{mj})}$, $\delta_{\mathrm{t\bar{t}}}$, δ_{W}, δ_{ST}, δ_{DY}, and $\delta_{\mathcal{L}}$. Adapting Equation 4.3, the total forward-central $\mathrm{t\bar{t}}$ charge asymmetry in the model is given by

$$A_c^y = A_c^{y(\mathrm{q\bar{q}})} + A_c^{y(\mathrm{qg})} + f_{\mathrm{gg}}\hat{A}_c^{y[\mathrm{gg}]}, \tag{6.16}$$

where

$$A_c^{y(k)} = \beta_k \hat{A}_c^{y[k]}, \qquad k \in \{\mathrm{q\bar{q}},\ \mathrm{qg}\}. \tag{6.17}$$

The contribution to A_c^y from gg initial states is a small correction, and the contribution from $\mathrm{\bar{q}g}$ is not included since its size is well below the level of sensitivity. The model has been implemented in RooFit [85].

6.3 Likelihood Fit

The likelihood of the model, given observations N_i^ℓ and expectations λ_i^ℓ, is the product of the Poisson likelihoods of each bin in each channel,

$$L = \prod_{\ell \in \{e,\mu\}} \prod_i \mathrm{Pois}\left(N_i^\ell \,\middle|\, \lambda_i^\ell\right). \tag{6.18}$$

Parameters of interest are $\beta_{\mathrm{q\bar{q}}}$ and β_{qg}. Nuisance parameters are $\delta_{\mathrm{q\bar{q}}}$, R, $F^{e}_{\mathrm{(mj)}}$, $F^{\mu}_{\mathrm{(mj)}}$, $\delta_{\mathrm{t\bar{t}}}$, and δ_{W}. Parameters $\delta_{\mathcal{L}}$, δ_{ST}, and δ_{DY} are held fixed, to zero or to a non-zero value when investigating systematic uncertainties.

The parameters of interest and nuisance parameters which minimize the negative log of the likelihood (NLL) are taken as the best fit. The profile of the negative log likelihood is defined as a function of $(\beta_{\mathrm{q\bar{q}}}, \beta_{\mathrm{qg}})$ as the difference between the minimized NLL for fixed $(\beta_{\mathrm{q\bar{q}}}, \beta_{\mathrm{qg}})$ and the globally minimized NLL,

$$\mathrm{PLL}(\beta_{\mathrm{q\bar{q}}}, \beta_{\mathrm{qg}}) = \mathrm{NLL}^{\mathrm{min}}\big|_{(\beta_{\mathrm{q\bar{q}}}, \beta_{\mathrm{qg}})} - \mathrm{NLL}^{\mathrm{min}} \tag{6.19}$$

The uncertainty on $(\beta_{\mathrm{q\bar{q}}}, \beta_{\mathrm{qg}})$ from statistics and uncertainty in the nuisance parameters is described by the contour of PLL equal to 1.14, which is expected to enclose a 68% confidence interval. The PLL contour is nearly elliptical in shape, and is approximated conservatively as the smallest ellipse which encloses it.

6.4 Ensemble Tests

The statistical performance of the model is verified by checking the aggregate properties of measurements of collections of pseudo-experiments. Binned data for one thousand pseudo-experiments is randomly generated according to Poisson probability from the expectations of the full selection model, for each of four ensembles with distinct sets of model parameters. Results for each pseudo-experiment are calculated as described in Section 6.3.

All ensembles use the measured values (see Chapter 7) of parameters $\delta_{\mathrm{t\bar{t}}}$, δ_{W}, $F^{e}_{\mathrm{(mj)}}$, and $F^{\mu}_{\mathrm{(mj)}}$, with δ_{ST}, δ_{DY}, and $\delta_{\mathcal{L}}$ set to zero, but have distinct values of the four parameters $\beta_{\mathrm{q\bar{q}}}$, β_{qg}, $\delta_{\mathrm{q\bar{q}}}$, and R. Pseudo-experiments in Ensemble A are generated with all four parameters identical to those measured in the data. Ensemble B is identical but for negated values of $\beta_{\mathrm{q\bar{q}}}$ and β_{qg}. Ensemble C uses the

Powheg expectation for all four parameters, and Ensemble D uses the Powheg expectation for $\delta_{q\bar{q}}$ and R, but sets $\beta_{q\bar{q}}$ and β_{qg} to zero.

Distributions of the calculated statistical uncertainty (σ), and the ratio of measurement error to uncertainty (δ/σ) are plotted for parameters $A_c^{y(q\bar{q})}$ and $A_c^{y(qg)}$ in Figure 6.3. Each distribution is fit with a Gaussian function, the best fit parameters of which are listed in Table 6.1. Of the 1000 pseudo-experiments, the generating parameter pair ($\beta_{q\bar{q}}, \beta_{qg}$) fell within the contour PLL=1.14 of the pseudo-experiment measurement 733 times for the Ensemble A, 742 times for Ensemble B, 758 times for Ensemble C, and 698 times for Ensemble D. The distributions of minimum negative log likelihood are shown in Figure 6.4a. The dependence of expected uncertainty in Ensemble A on integrated luminosity is shown in Figure 6.4b.

The conservative choice to use the smallest ellipse enclosing the profile likelihood contour explains the moderate overcoverage observed. The otherwise normally distributed values of δ/σ with mean near zero indicate that the measurement is unbiased and that the reported uncertainties are (conservatively) accurate. As shown by the blue arrows in Figures 6.3 and 6.4a, the data measurement has estimated statistical uncertainties and minimum negative log likelihood in bins of high probability for Ensemble A, which suggests that the model describes the data well.

6.5 Systematic Uncertainties

Some of the information upon which the model is built is imprecisely known, which gives rise to systematic uncertainties in the results. Except for simulation statistical uncertainty, each systematic uncertainty is quantified by reevaluating the best fit with each source of uncertainty shifted to the upper and lower bounds of its 68% confidence interval. The uncertainty matrix for each of these systematic

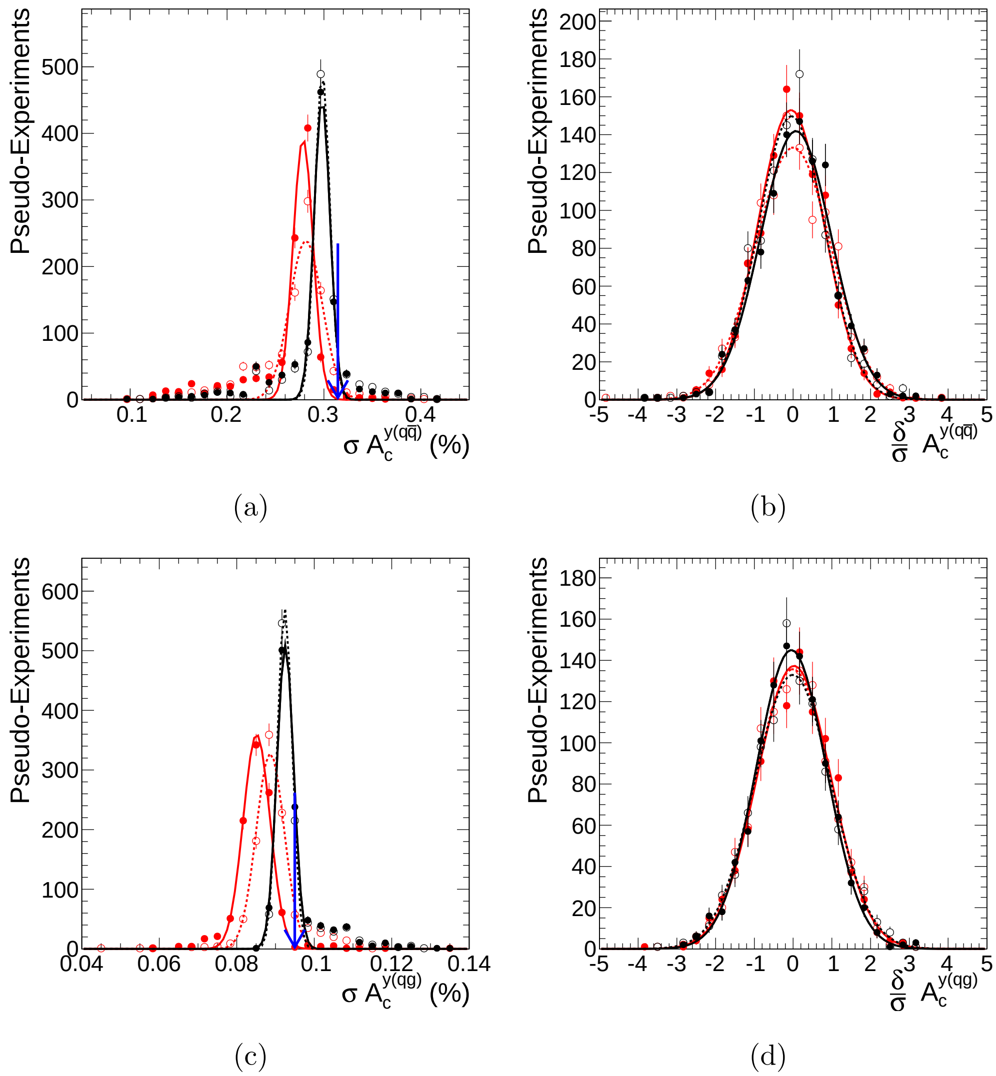

Figure 6.3: Aggregate results from measurements of pseudo-experiments in Ensembles A (solid black), B (open black), C (open red), and D (solid red). Plotted are the estimated statistical uncertainty σ for $A_c^{y(q\bar{q})}$ (a) and $A_c^{y(qg)}$ (c), and the respective ratios of measurement error to uncertainty δ/σ (b,d). The parameters for the best fit Gaussian functions are listed in Table 6.1. The blue arrows in (a,c) indicate the estimated statistical uncertainty in the measurement of the real data.

		$A_c^{y(\mathrm{q\bar{q}})}$		$A_c^{y(\mathrm{qg})}$	
		mean	sigma	mean	sigma
σ (%)	A	0.2980(3)	0.0083(3)	0.09252(8)	0.00216(7)
	B	0.2983(3)	0.0078(2)	0.09238(6)	0.00192(5)
	C	0.2785(4)	0.0103(4)	0.0851(1)	0.00346(8)
	D	0.2813(7)	0.0169(8)	0.0886(1)	0.0036(1)
δ/σ	A	0.07(3)	0.92(2)	-0.05(3)	0.90(2)
	B	-0.04(3)	0.86(2)	-0.01(3)	0.99(3)
	C	-0.06(3)	0.85(2)	0.02(3)	0.96(2)
	D	0.04(3)	0.98(2)	-0.00(3)	0.97(2)

Table 6.1: The best fit Gaussian parameters for Ensembles A, B, C, and D, for components of A_c^y: the difference between the measured value and the generating value, δ; the estimated uncertainty, σ; and their ratio, δ/σ.

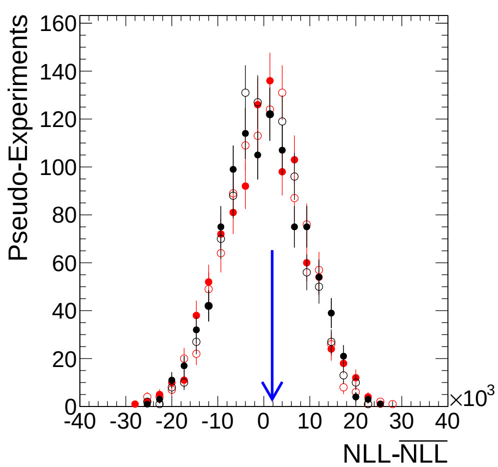

(a)

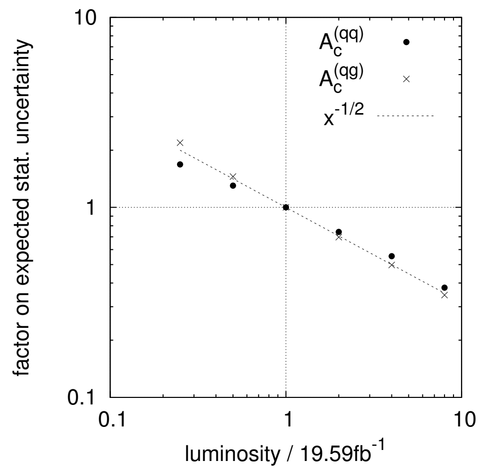

(b)

Figure 6.4: Shown in (a), the distributions of minimum negative log likelihood (difference from ensemble average) for Ensembles A (solid black) B (open black), C (open red), and D (solid red), and the value from the measurement of data in blue. In (b), expected sensitivity of Ensemble A is plotted against integrated luminosity, both relative to an integrated luminosity of 19.6 fb^{-1}.

sources of uncertainty n is

$$\Sigma_n^2 = \frac{1}{2}\left(\Sigma_{n\downarrow}^2 + \Sigma_{n\uparrow}^2\right), \tag{6.20}$$

where

$$\Sigma_{n\updownarrow}^2 = D_{n\updownarrow} \otimes D_{n\updownarrow}^T \tag{6.21}$$

and $D_{n\updownarrow} = \begin{pmatrix} \delta A_c^{y(\mathrm{q\bar{q}})} & \delta A_c^{y(\mathrm{qg})} \end{pmatrix}^T$ is the displacement from the central value of the measurement resulting from a shift up or down in the source n. The total systematic uncertainty including simulation statistics is

$$\Sigma_{sys}^2 = \sum_n \Sigma_n^2. \tag{6.22}$$

Sources of uncertainty in the measurement due to possible systematic errors are described in the following. Magnitudes of each effect are tabulated in Chapter 7.

Simulation Statistics Since the selection efficiency is low, only a limited number of simulated events define the template distributions, with the count in each bin presumably drawn from a Poisson distribution around some expected value. For each simulated distribution used in template construction and the data sidebands, $N = 1000$ alternative distributions are drawn with Poisson fluctuations. The spread of measurements using the alternative sets of template constructions, $\Sigma_{\mathrm{mc}}^2 = \frac{1}{N}\sum_{k=1}^{N} D_k \otimes D_k^T$, represents the systematic uncertainty on the result due to statistical uncertainty of the template shapes.

Luminosity The luminosity used in the model is varied by $\pm 4.4\%$, according to the recommendations of the CMS collaboration, by setting the parameter $\delta_{\mathcal{L}}$ to ± 0.044. This variation represents the level at which the various algorithms used to measure the luminosity agree. Varying the luminosity has essentially the same effect on the model as varying the Single Top and Drell-Yan cross sections simultaneously up or down.

Single Top Cross Section The cross sections of Single Top processes are varied collectively ±10% by setting the parameter δ_{ST} to ±0.1. The single top templates have a negative asymmetry between one and three percent in both X_T^{rec} and X_L^{rec}, and the expected number of events make the contribution to the raw asymmetry non-negligible. Calculations of the NNLO cross sections for single top processes [86] are five to twenty-five percent higher than the NLO cross sections used in the model. Ten percent variations may not cover a 68% confidence interval for this systematic; however, even a factor of 2 scaling of the effect on the results from the 10% variations does not bring this systematic to dominance.

Drell-Yan Cross Section The cross sections of Drell-Yan processes are varied collectively ±10% by setting the parameter δ_{DY} to ±0.1. Calculations of the NNLO cross section for Drell-Yan with $m_{\ell\ell} > 50\,\mathrm{GeV/c^2}$ with FEWZ [87] are about twenty percent higher than the leading order cross section used in the model. Ten percent variations may not cover a 68% confidence interval for this systematic; however, the effect on results with ten percent variations is negligible, as expected. The Drell-Yan templates have near zero asymmetry in X_T^{rec} and X_L^{rec}, and a very small number of expected events.

Jet Energy Scale Jet energy scale is varied only for data in the reconstruction of jets, with total jet energy corrections uncertainty varied up and down, according to the recommendations of the CMS collaboration. Corrections are propagated to $E_{\mathrm{T}}^{\mathrm{miss}}$. These variations change the selected events in data due to jet threshold effects.

Jet Energy Resolution Jet energy resolution in all simulation samples is varied according to CMS collaboration recommendations to match the measured jet energy resolution [80, 81]. Corrections are propagated to $E_{\mathrm{T}}^{\mathrm{miss}}$. These variations change event selection in simulation due to jet threshold effects.

Parton Density Functions, α_s, Q^2 The CT10 set of parton density functions identifies 26 uncertainty eigenvectors, the strong coupling α_s, and the scale Q^2 , each of which can be varied up or down [73]. The $\mathrm{t\bar{t}}$ events are reweighted to see the effect on the measurement for each of these 56 variations. This strategy is a more comprehensive evaluation of PDF systematic uncertainties on asymmetries than the procedure recommended by PDF4LHC [88]. Asymmetry is less sensitive to varying the observable distributions to the maximum and minimum of an envelope, as recommended by PDF4LHC, than to effects for which the observable distribution is decreased in one area and increased in another, as is the case for some of the eigenvectors. The CT10 default 90% confidence interval uncertainties are used for the eigenvectors and α_s rather than scaling them to a 68% confidence interval. The scale Q is varied from the nominal value of $m_\mathrm{t} = 172\,\mathrm{GeV/c^2}$ to $2m_\mathrm{t}$ and $m_\mathrm{t}/2$.

Pileup Distribution The pileup distribution to which the simulation samples are reweighted is recalculated with the minimum bias cross section scaled up or down by 6%, according to CMS collaboration recommendations.

W with Heavy Flavor Jets There is concern that the fraction of heavy flavor jets in the W+jets sample may not be modeled correctly. Heavy flavor events ($\mathrm{b\bar{b}}, \mathrm{c\bar{c}}$) in the W+jets sample tend to fall in the middle bin (bin 3 of 5) of the tridiscriminant Δ. Increased or decreased heavy flavor content is simulated by modifying the shape of the W+jets template, scaling the counts in bin 3 of the tridiscriminant by a factor of 1.5 or 0.5, respectively.

Top Transverse Momentum It is clear that several correlated kinematic distributions in the selection are slightly mismodeled, including top quark (antiquark) transverse momentum, $\mathrm{t\bar{t}}$ system transverse momentum, $\mathrm{t\bar{t}}$ system rapidity, and transverse momenta of top decay products. Allowing the fractional contribution of each initial state process to float as a nuisance parameter in the profile likelihood may partially address this modeling discrepancy. An additional check is made of the effect on the results of reweighting $t\bar{t}$ events according to CMS collaboration recommendations to match the transverse momentum spectra of generated top quarks and antiquarks.

Trigger Efficiency The trigger efficiencies are increased(decreased) for the electron+jets channel and the muon+jets channel independently, according to the uncertainties quoted in the corresponding efficiency measurements of the CMS collaboration.

ID and Isolation Efficiency The identification and isolation efficiency of the lepton is increased(decreased) for the electron+jets channel and the muon+jets channel independently, according to the uncertainties quoted in the corresponding efficiency measurements of the CMS collaboration.

7 Results

Reconstructed joint distributions of the observables X_L^{rec}, X_T^{rec}, and the tridiscriminant Δ for each data selection described in Chapter 5 are evaluated in the context of the model described in Chapter 6. The measured composition of each signal sample is entered in Table 7.1. The corresponding best fit relative adjustments to the cross sections are listed in Table 7.2, along with the best fit fractions of $\mathrm{t\bar{t}}$ production processes. Figures 7.1 and 7.2 show the data distributions for $\mathrm{t\bar{t}}$ system invariant mass and absolute rapidity in each channel, overlaid with the best fit model.

Figure 7.3 shows projections of the joint distributions for each observable for the full selection, overlaid on the best fit model. The corresponding contributions $A_c^{y(\mathrm{q\bar{q}})}$ and $A_c^{y(\mathrm{qg})}$ of $\mathrm{q\bar{q}}$ and qg initial states to the forward-central $\mathrm{t\bar{t}}$ charge asymmetry A_c^y are plotted in Figure 7.4. The elliptical contours in the figure show the total 68% confidence interval, as well as the 68% confidence intervals associated with the statistical uncertainty (the profile likelihood contour), and the systematic uncertainty. The systematic uncertainty due to simulation statistics is reducible, so it is shown separately. Projected one-dimensional 68% confidence intervals are shown for the $\mathrm{q\bar{q}}$ contribution on the top axis and for the qg contribution on the left axis. The total A_c^y is given by Equation 6.16, a sum of the two plotted contributions plus a small correction, so its projected 68% confidence interval is

	Thousands of events						
	$t\bar{t}$	W	MJ	ST	DY	Total	Observed
	Full Selection						
e	210(8)	49(8)	47(10)	14(2)	5.4(6)	325(25)	326.185
μ	246(10)	58(9)	16(6)	17(2)	4.3(5)	341(24)	340.911
	$m_{t\bar{t}} < 450\,\mathrm{GeV/c^2}$						
e	95(4)	18(4)	19(4)	6.0(7)	2.5(3)	141(11)	141.196
μ	112(4)	23(5)	9(3)	7.1(8)	2.0(2)	153(11)	152.413
	$m_{t\bar{t}} > 450\,\mathrm{GeV/c^2}$						
e	118(5)	29(4)	27(6)	8.1(9)	3.0(3)	185(14)	184.989
μ	136(6)	34(5)	7(3)	9.4(1.1)	2.3(3)	189(13)	188.498
	$\tanh\lvert y_{t\bar{t}}\rvert < 0.5$						
e	116(5)	28(4)	25(5)	7.9(9)	2.8(3)	179(14)	179.159
μ	134(6)	34(5)	8(4)	9.2(1.0)	2.2(3)	188(13)	188.191
	$\tanh\lvert y_{t\bar{t}}\rvert > 0.5$						
e	95(4)	21(3)	22(5)	6.1(7)	2.6(3)	146(12)	147.026
μ	112(5)	24(4)	8(3)	7.3(8)	2.0(2)	153(11)	152.720

Table 7.1: Sample composition of the best fit model, for each selection, in thousands of events. Combined statistical and systematic uncertainty on the last digit(s) is indicated in parentheses.

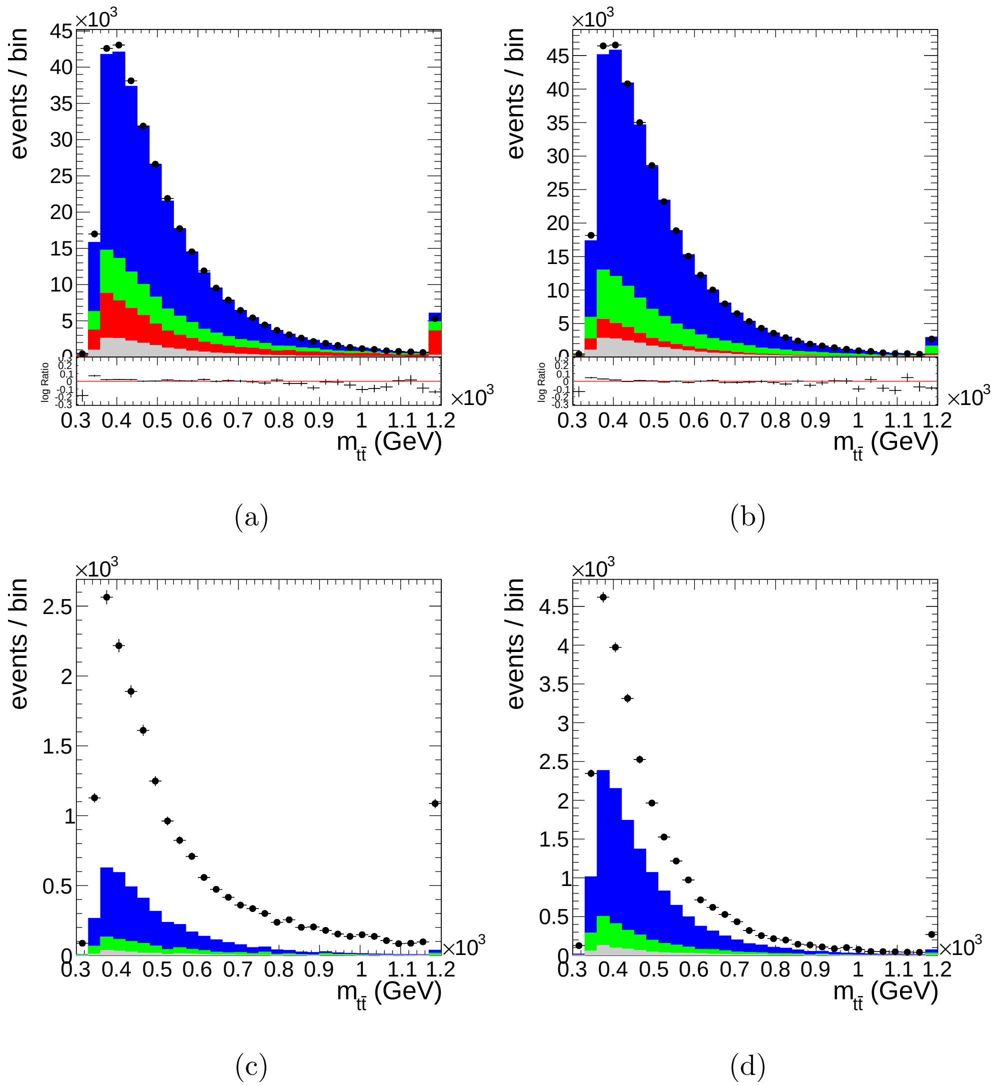

Figure 7.1: The invariant mass of the reconstructed $t\bar{t}$ system, for (a) e+jets signal selection, (b) μ+jets signal selection, (c) e+jets isolation sideband, and (d) μ+jets isolation sideband, overlaid with the best fit model. The model includes the simulated components $t\bar{t}$ (blue), W+jets (green), Single Top (gray) and Drell-Yan (also gray). The shape of the multijet component (red) is taken from the difference of the data and the other model components in the respective sidebands. The log of the ratio of the data and the model is shown for the signal selections.

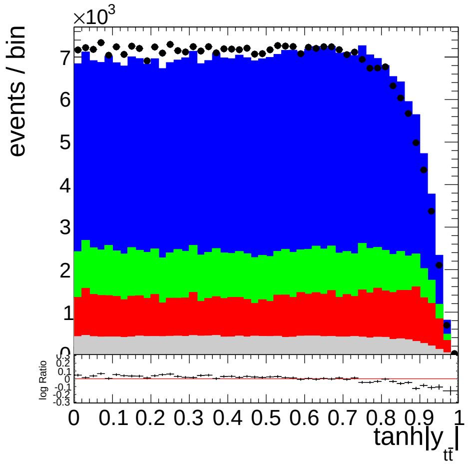

(a)

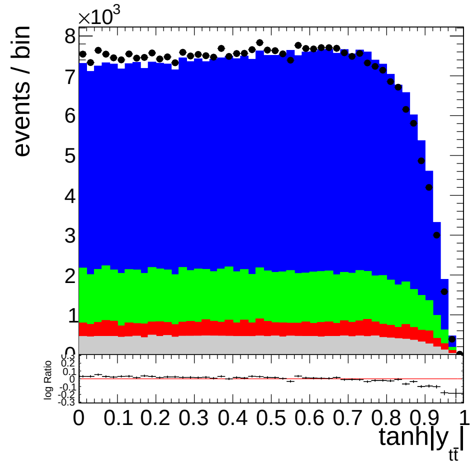

(b)

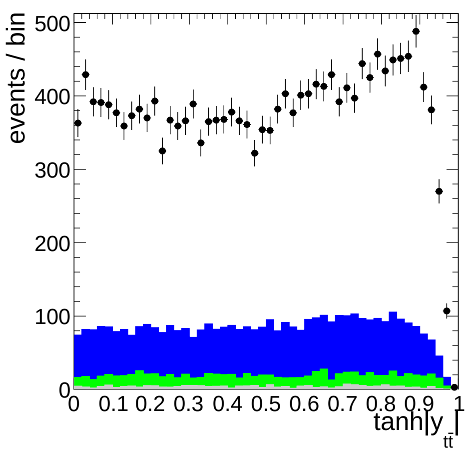

(c)

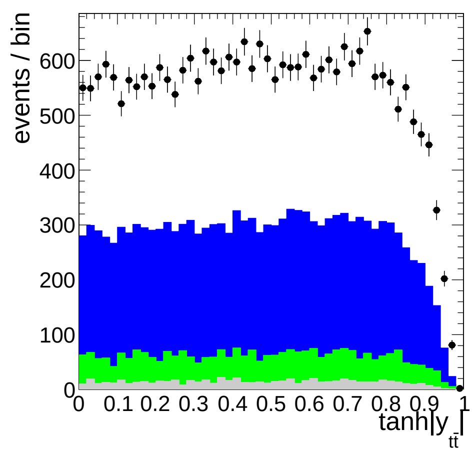

(d)

Figure 7.2: The hyperbolic tangent of absolute rapidity of the reconstructed $t\bar{t}$ system, for (a) e+jets signal selection, (b) μ+jets signal selection, (c) e+jets isolation sideband, and (d) μ+jets isolation sideband, overlaid with the best fit model. The model includes the simulated components $t\bar{t}$ (blue), W+jets (green), Single Top (gray) and Drell-Yan (also gray). The shape of the multijet component (red) is taken from the difference of the data and the other model components in the respective sidebands. The log of the ratio of the data and the model is shown for the signal selections.

	(%)					
	$\delta_{t\bar{t}}$	δ_{W}	f_{gg}	$f_{q\bar{q}}$	f_{qg}	$f_{\bar{q}g}$
POWHEG CT10	0	-	65(3)	13(2)	18(1)	3.2(3)
Full Selection	16(9)	76(30)	51(19)	15(17)	32(9)	1.7(1.7)
$m_{t\bar{t}} < 450\,\mathrm{GeV/c^2}$	19(9)	67(36)	48(15)	7(10)	45(10)	0.5(0.7)
$m_{t\bar{t}} > 450\,\mathrm{GeV/c^2}$	10(8)	74(26)	57(12)	4(12)	39(9)	0.4(1.1)
$\tanh\|y_{t\bar{t}}\| < 0.5$	16(11)	83(31)	70(12)	6(13)	22(15)	1.2(3.2)
$\tanh\|y_{t\bar{t}}\| > 0.5$	11(7)	67(30)	57(10)	7(4)	35(10)	0.8(0.6)

Table 7.2: Best fit values of the cross section adjustment parameters $\delta_{t\bar{t}}$ and δ_{W}, and of the fractions of $t\bar{t}$ production by initial state before selection cuts. Combined statistical and systematic uncertainty on the last digit(s) is indicated in parentheses.

shown on the diagonal axis. Also shown are the 68% confidence intervals for the POWHEG + CT10 calculation, and the 2012 Standard Model calculations by Kühn and Rodrigo [55], and by Bernreuther and Si [56].

The joint distribution projections and the confidence interval plots corresponding to other signal selections are shown in Figures 7.5 through 7.12. Figure 7.13 is a comparative display of the 68% confidence intervals of each selection. The central values of $A_c^{y(q\bar{q})}$, $A_c^{y(qg)}$ and A_c^{y} from the measurement and the predictions are presented in Table 7.3. The magnitudes of each source of systematic uncertainty on A_c^{y} are listed in Table 7.4.

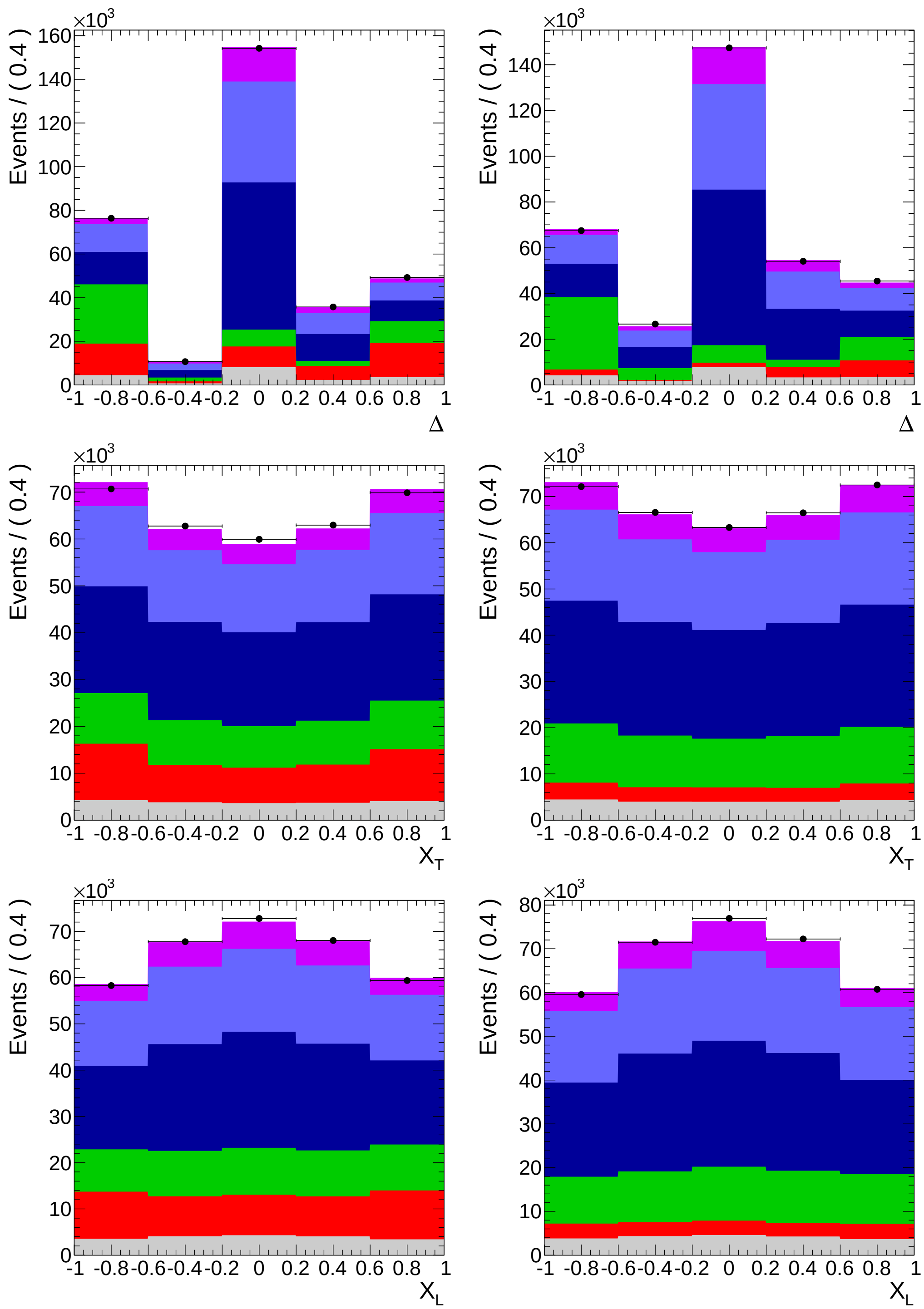

Figure 7.3: Projections of data for the full selection, in the electron (left) and muon (right) channels, are overlaid with the best fit model:

$q\bar{q} \to t\bar{t}$; $\{qg, \bar{q}g\} \to t\bar{t}$; $gg \to t\bar{t}$; W+jets ; multijets; other.

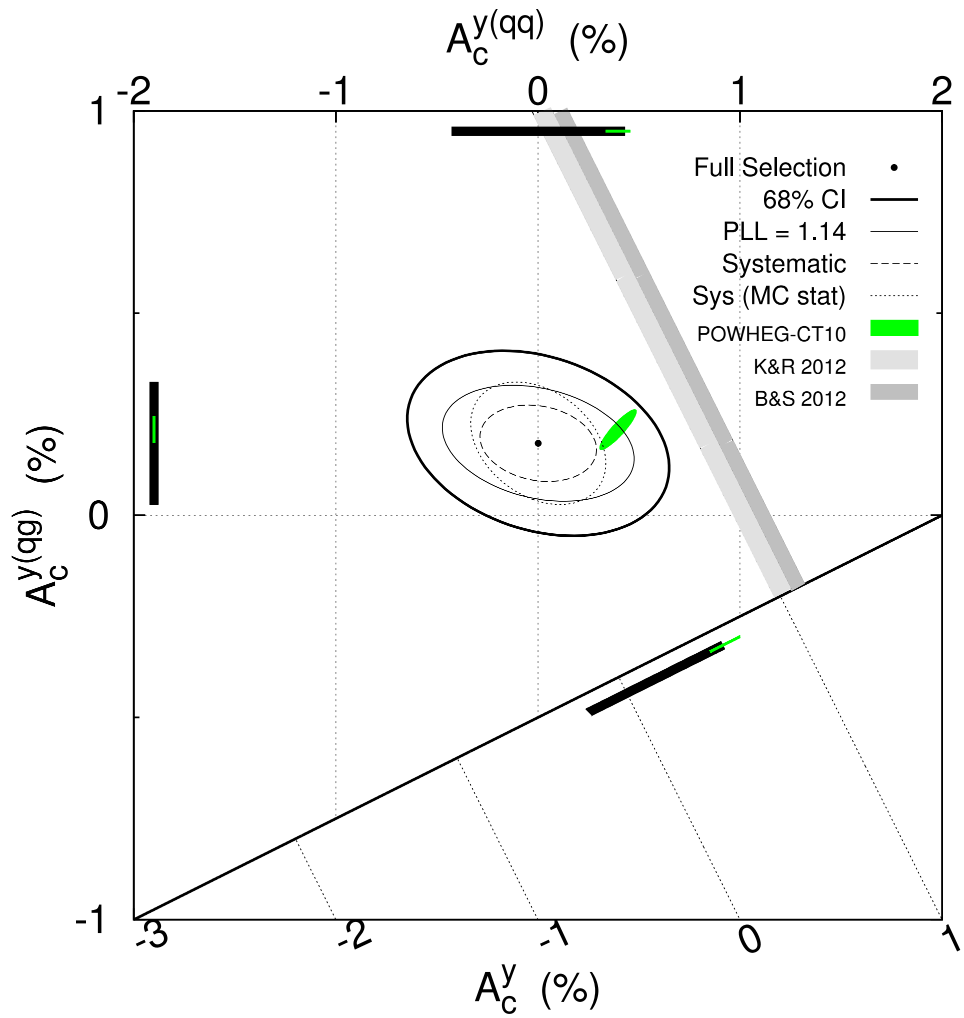

Figure 7.4: Most likely values of $A_c^{y(q\bar{q})}$, $A_c^{y(\mathrm{qg})}$, and A_c^y (gg correction omitted), for the full selection, with projections of the 68% confidence interval for each on the top, left, and diagonal axes, respectively.

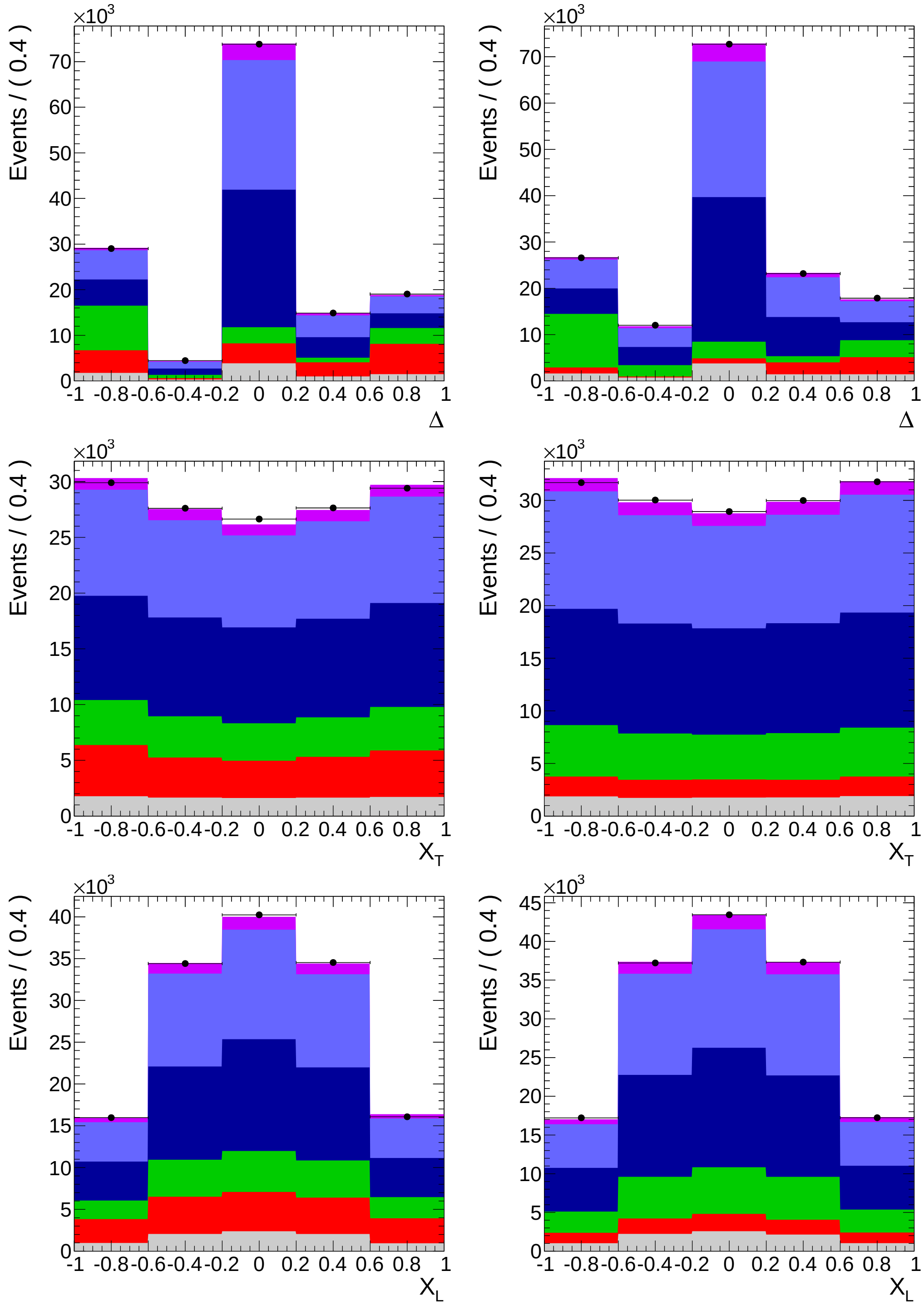

Figure 7.5: Projections of data for the $m_{t\bar{t}} < 450\,\mathrm{GeV}/c^2$ selection, in the electron (left) and muon (right) channels, are overlaid with the best fit model: $q\bar{q} \to t\bar{t}$; $\{qg, \bar{q}g\} \to t\bar{t}$; $gg \to t\bar{t}$; W+jets ; multijets; other.

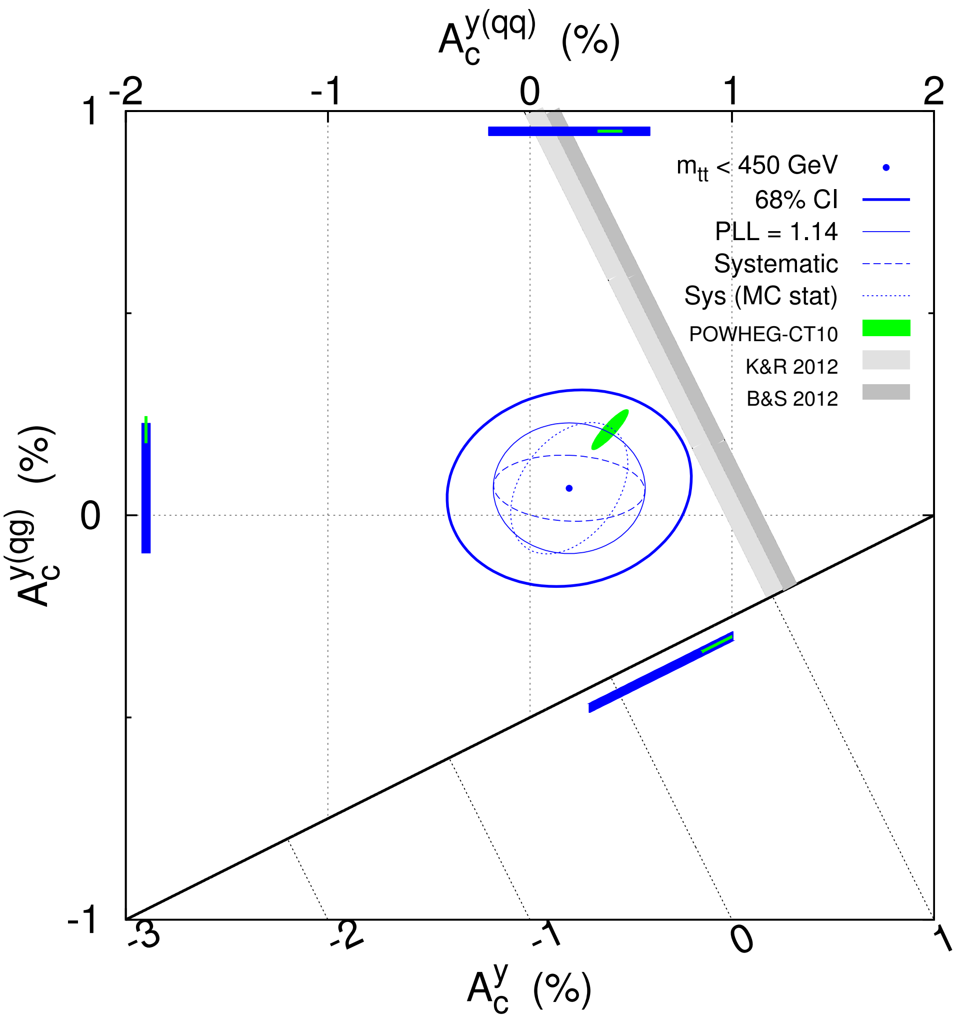

Figure 7.6: Most likely values of $A_c^{y(q\bar{q})}$, $A_c^{y(qg)}$, and A_c^y (gg correction omitted), for the $m_{t\bar{t}} < 450\,\mathrm{GeV/c^2}$ selection, with projections of the 68% confidence interval for each on the top, left, and diagonal axes, respectively.

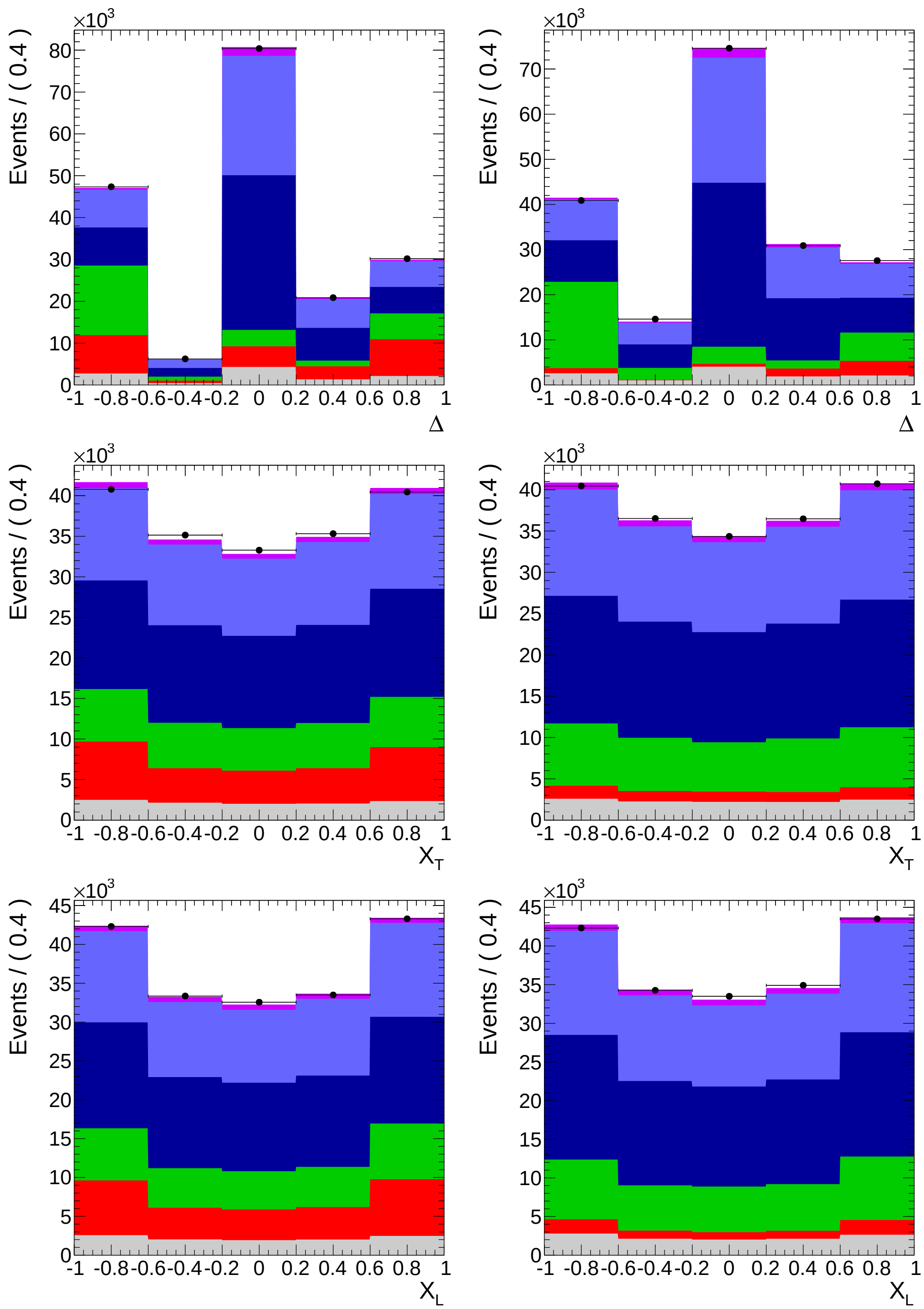

Figure 7.7: Projections of data for the $m_{t\bar{t}} > 450\,\mathrm{GeV}/c^2$ selection, in the electron (left) and muon (right) channels, are overlaid with the best fit model: $q\bar{q} \to t\bar{t}$; $\{qg, \bar{q}g\} \to t\bar{t}$; $gg \to t\bar{t}$; W+jets ; multijets; other.

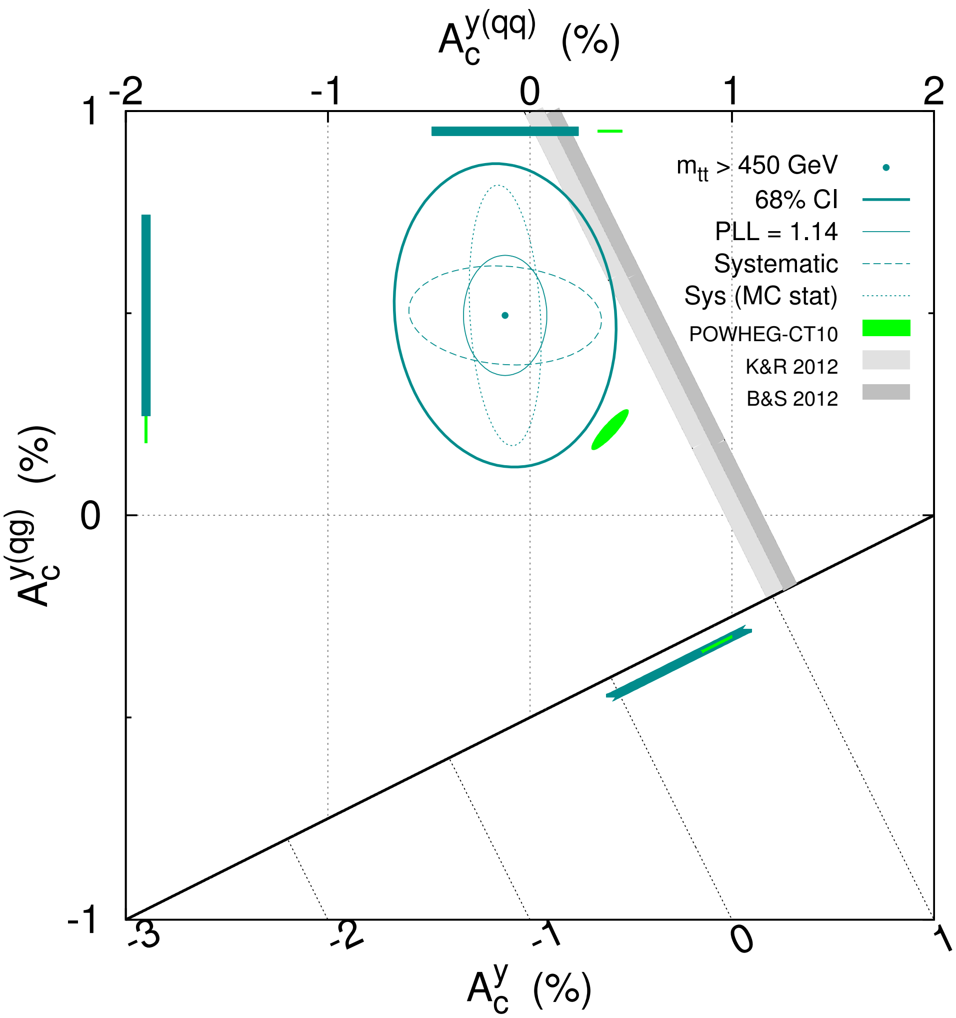

Figure 7.8: Most likely values of $A_c^{y(\mathrm{q\bar{q}})}$, $A_c^{y(\mathrm{qg})}$, and A_c^y (gg correction omitted), for the $m_{\mathrm{t\bar{t}}} > 450\,\mathrm{GeV/c^2}$ selection, with projections of the 68% confidence interval for each on the top, left, and diagonal axes, respectively.

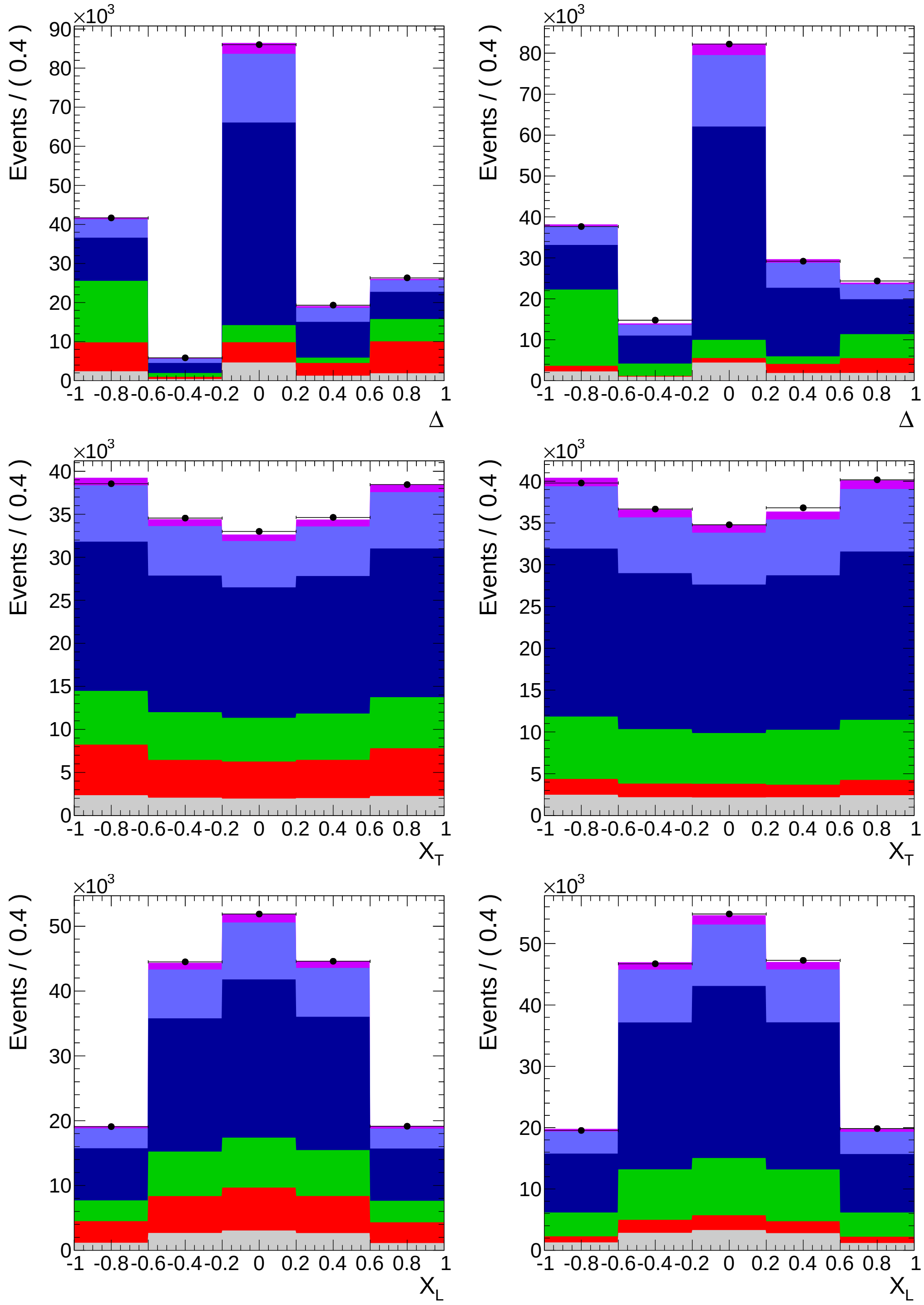

Figure 7.9: Projections of data for the tanh $|y_{t\bar{t}}| < 0.5$ selection, in the electron (left) and muon (right) channels, are overlaid with the best fit model: $q\bar{q} \to t\bar{t}$; $\{qg, \bar{q}g\} \to t\bar{t}$; $gg \to t\bar{t}$; W+jets ; multijets; other.

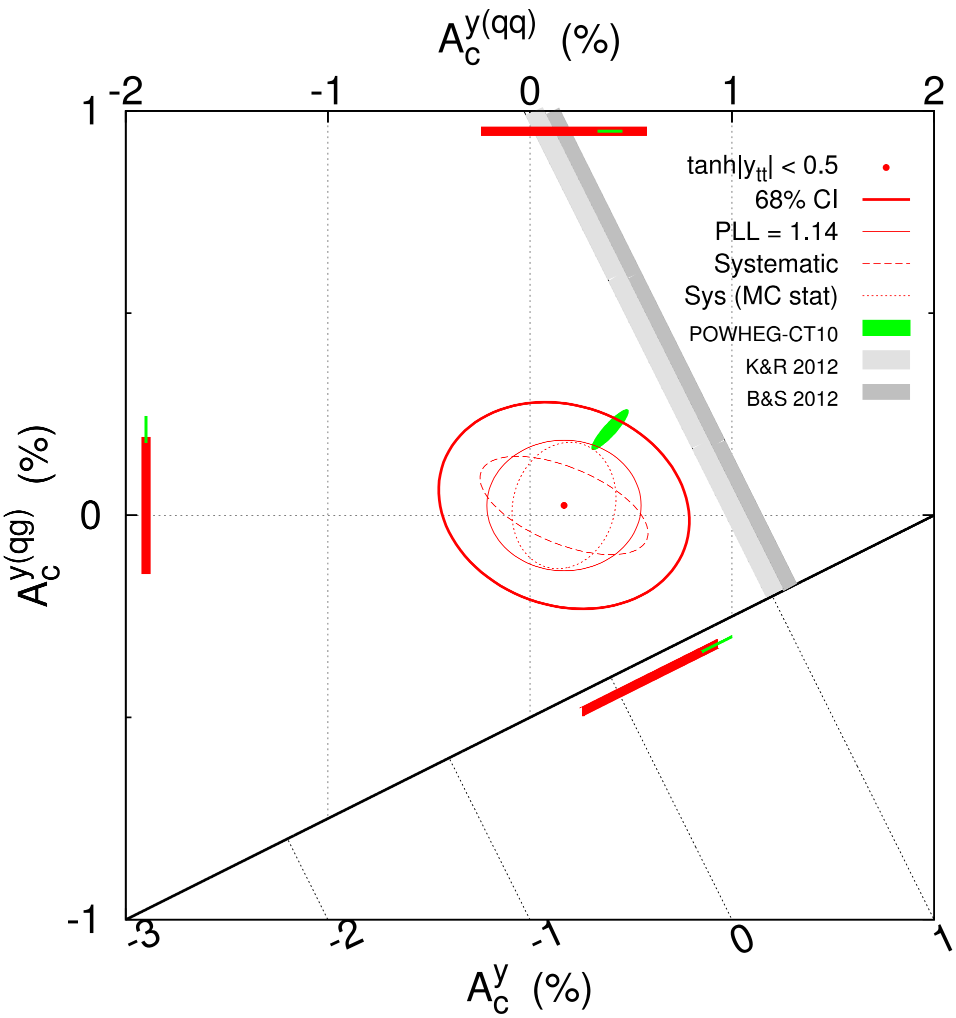

Figure 7.10: Most likely values of $A_c^{y(q\bar{q})}$, $A_c^{y(qg)}$, and A_c^y (gg correction omitted), for the tanh $|y_{t\bar{t}}| < 0.5$ selection, with projections of the 68% confidence interval for each on the top, left, and diagonal axes, respectively.

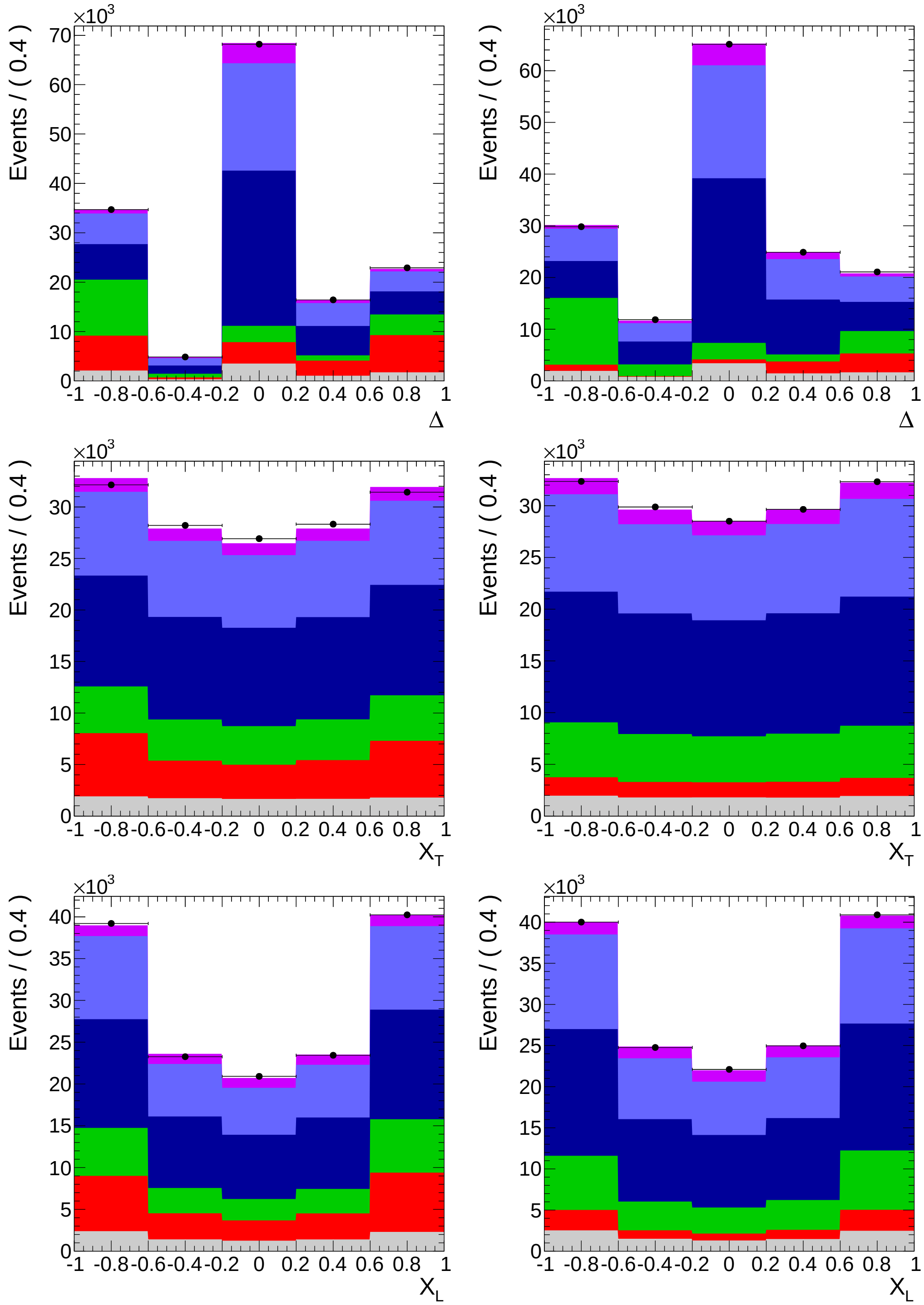

Figure 7.11: Projections of data for the $\tanh|y_{t\bar{t}}| > 0.5$ selection, in the electron (left) and muon (right) channels, are overlaid with the best fit model: $q\bar{q} \to t\bar{t}$; $\{qg, \bar{q}g\} \to t\bar{t}$; $gg \to t\bar{t}$; W+jets ; multijets; other.

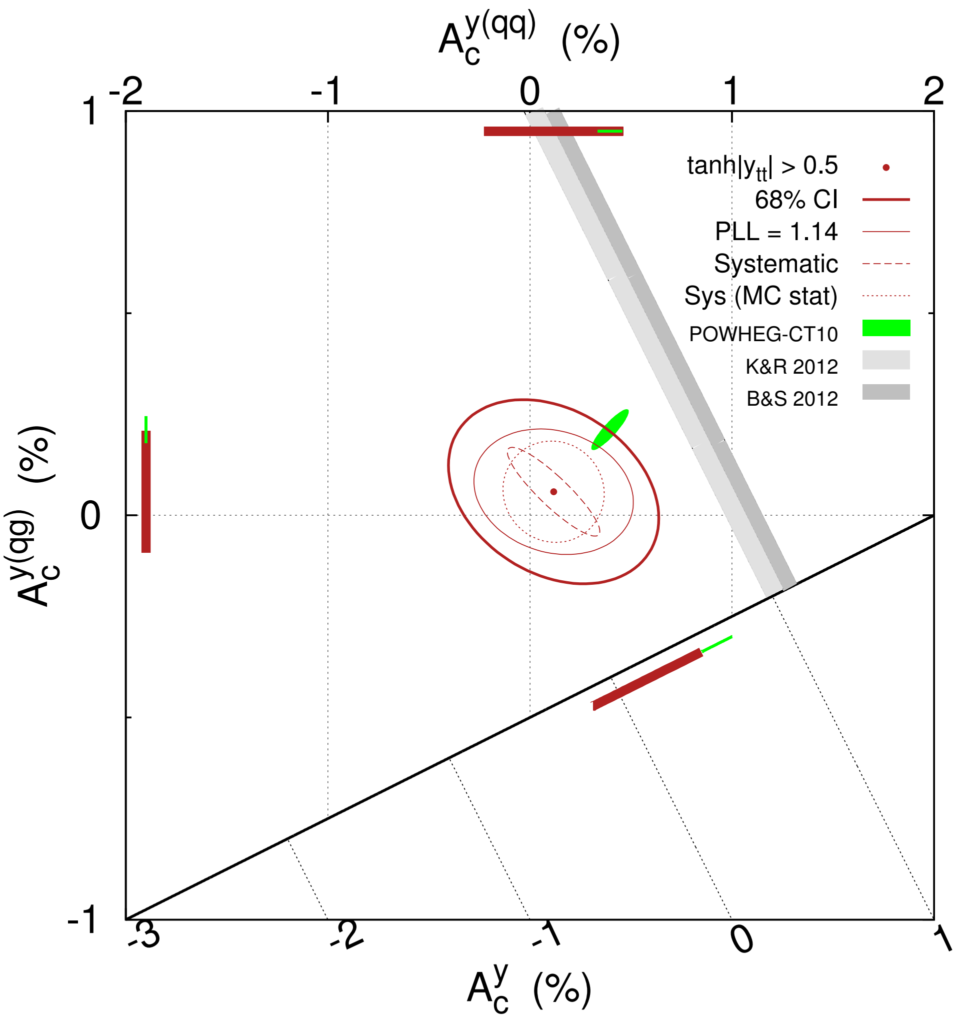

Figure 7.12: Most likely values of $A_c^{y(q\bar{q})}$, $A_c^{y(qg)}$, and A_c^{y} (gg correction omitted), for the $\tanh|y_{t\bar{t}}| > 0.5$ selection, with projections of the 68% confidence interval for each on the top, left, and diagonal axes, respectively.

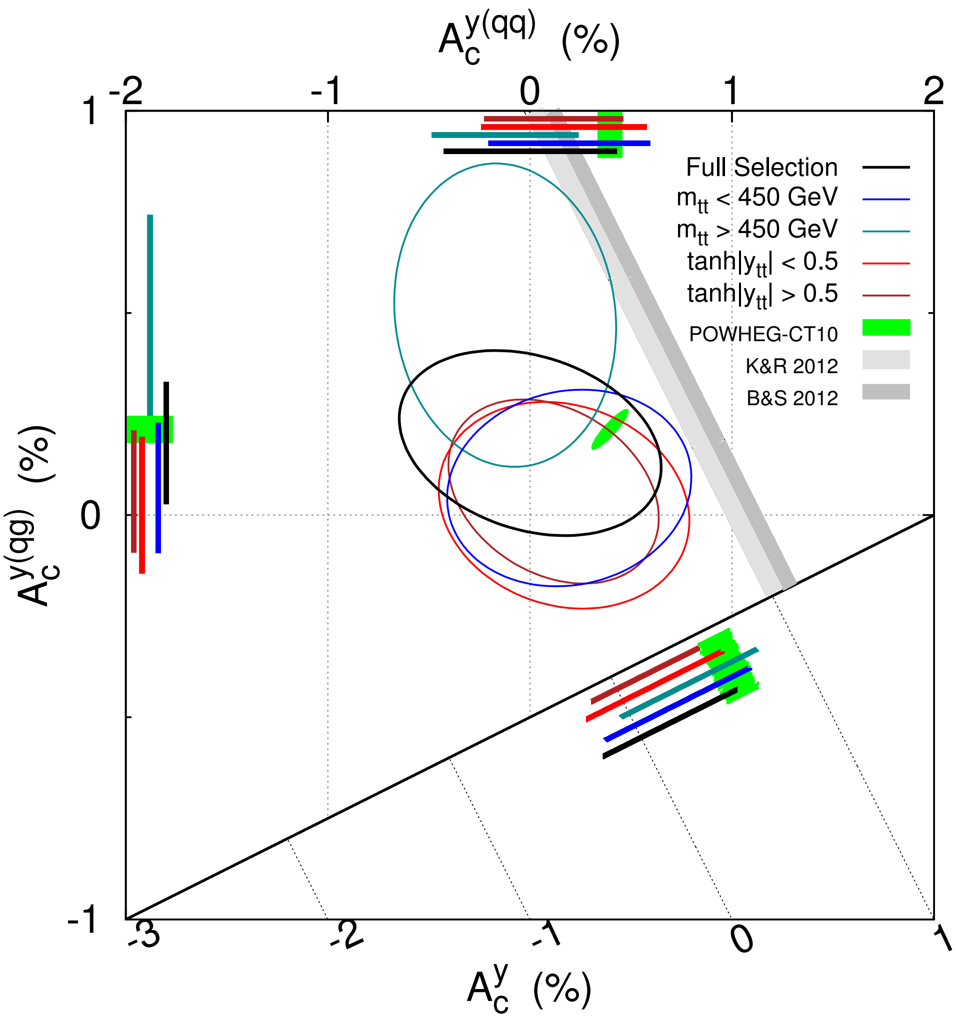

Figure 7.13: Comparison of 68% confidence intervals from each selection.

	(%) $A_c^{y(q\bar{q})}$	$A_c^{y(qg)}$	A_c^y
K&R 2012 [55]	-	-	1.02(5)
B&S 2012 [56]	-	-	1.11(4)
POWHEG CT10	0.40(6)	0.21(3)	0.57(9)
Full Selection	0.00(43)	0.18(15)	0.15(42)
$m_{t\bar{t}} < 450\,\mathrm{GeV/c^2}$	0.19(40)	0.07(16)	0.23(45)
$m_{t\bar{t}} > 450\,\mathrm{GeV/c^2}$	-0.12(36)	0.49(25)	0.34(42)
$\tanh\lvert y_{t\bar{t}}\rvert < 0.5$	0.17(41)	0.02(17)	0.15(42)
$\tanh\lvert y_{t\bar{t}}\rvert > 0.5$	0.12(34)	0.06(15)	0.14(33)

Table 7.3: Comparison of predicted and measured charge asymmetries. Uncertainty on the last digit(s) of each number are in parentheses, and indicate 68% confidence intervals.

(%)					
	Full Selection	$m_{t\bar{t}}$ :: 450 GeV/c^2 <	$m_{t\bar{t}}$ :: 450 GeV/c^2 >	$\tanh\|y_{t\bar{t}}\|$ :: 0.5 <	$\tanh\|y_{t\bar{t}}\|$ :: 0.5 >
MC stat.	**0.211**	**0.253**	**0.222**	**0.209**	**0.182**
JES	**0.144**	**0.093**	0.028	**0.034**	**0.072**
$Wb\bar{b}$	**0.072**	**0.146**	0.034	0.026	**0.009**
JER	**0.065**	**0.082**	**0.071**	**0.077**	**0.043**
PDF	**0.065**	**0.134**	**0.290**	**0.200**	**0.037**
pileup	0.036	0.020	**0.060**	0.012	0.006
σ_{ST}	0.018	0.013	0.012	0.005	0.003
Q^2 scale	0.017	0.065	0.039	**0.090**	0.001
α_s	0.008	0.019	0.052	0.033	0.002
μ trig	0.004	0.034	0.003	0.001	0.003
p_T^t	0.003	0.007	**0.053**	0.007	0.002
$\mathcal{L}$	0.003	0.007	0.006	0.003	0.008
σ_{DY}	0.003	0.007	0.001	0.003	0.003
e id	0.002	0.015	0.002	0.001	0.001
μ id	0.001	0.003	0.001	0.002	0.001
e trig	0.001	0.028	0.005	0.004	0.003
Total	0.285	0.355	0.390	0.318	0.204

Table 7.4: Uncertainty on A_c^y due to sources of systematic variations, ordered by decreasing magnitude in the full selection. The five greatest sources of systematic uncertainty in each selection are in bold.

7.1 Discussion

The measurement of the $\mathrm{t\bar{t}}$ charge asymmetry A_c^y from the full event selection is compatible with the Powheg prediction, but does not unambiguously determine the sign. The uncertainty in the measurement due to statistics and profiled parameters and the total systematic uncertainty are comparable in size. Since the dominant systematic uncertainty is due to statistical uncertainty in the templates, it can be reduced with increased simulation statistics. Uncertainty in the Powheg prediction is due to systematic uncertainty in parton distribution functions, renormalization and factorization scales, and strong coupling.

It is important to recognize that even when a $\mathrm{t\bar{t}}$ kinematic selection is used, the measured $\mathrm{t\bar{t}}$ charge asymmetry is inclusive. The predictions for the inclusive $\mathrm{t\bar{t}}$ charge asymmetry do not depend on the particular selection or subselection used to make the measurement. However, differences in the measured inclusive asymmetry between selections of neighboring kinematic regions may indicate a differential $\mathrm{t\bar{t}}$ charge asymmetry different from that of the base model, Powheg. The results suggest that the relative $\mathrm{t\bar{t}}$ charge asymmetries in various kinematic regions are well modeled by Powheg.

The measurement in the kinematic region $\tanh|y_{\mathrm{t\bar{t}}}| > 0.5$ has the least total uncertainty, with a difference from the Powheg, K&R, and B&S predictions equivalent to 1.3, 2.6, and 2.9 standard deviations, respectively. Lower statistical uncertainty at high absolute system rapidity can be expected since the relative contribution from the gg initial state is smaller and the asymmetry of the $\mathrm{q\bar{q}}$ and qg initial states is greater. The relatively lower systematic uncertainty of the measurement in this kinematic region may be physical, or may be an artifact of dependence on the statistical uncertainty.

It is interesting to note that the $\mathrm{q\bar{q}}$ and qg contributions to A_c^y correspond with fixed factors to respective contributions to A_c^ϕ. These factors are taken from the base model, Powheg, and can be read from the ratio of column entries in the appropriate row of Table 4.2: 0.1 for $q\bar{q}$ and 3.22 for qg. The measured components of A_c^{ϕ} with the full selection are thus $A_c^{\phi(q\bar{q})} = 0.00(4)\%$ and $A_c^{\phi(qg)} = 0.58(48)\%$. The contribution from $\bar{q}g$ is predicted by Powheg to be $\hat{A}_c^{\phi(\bar{q}g)} = -0.14\%$, which can be included both as an expected contribution and conservatively as an additional systematic uncertainty in estimating $A_c^{\phi} = 0.44(50)\%$. The result is in good agreement with the Powheg prediction listed in Table 4.2.

7.2 Sensitivity to Classification Threshold

It is informative to discuss the sensitivity of the results to the choice of the initial state classification threshold for the recoiling quark transverse momentum, described in Section 4.2. Measurement results were evaluated under the alternative classification threshold of 30 GeV/c, rather than the 20 GeV/c threshold used for the main analysis. It must be emphasized that the choice of threshold is a matter of definition, and is not a source of systematic uncertainty.

Increasing the threshold from 20 GeV/c to 30 GeV/c reclassifies events with recoiling quark transverse momentum between these values from the qg and $\bar{q}g$ categories into the $q\bar{q}$ and gg categories. The expected fractions and intrinsic asymmetries of each category differ for the two classification schemes, as detailed in Table 4.3. The total inclusive charge asymmetry is independent of the initial state classification scheme, so the change of threshold is not expected to affect the measurement results for A_c^y. Figure 7.14 shows that the expectation of a threshold-independent result for the total inclusive charge asymmetry is well met by the measurements with the full selection and all the subselections.

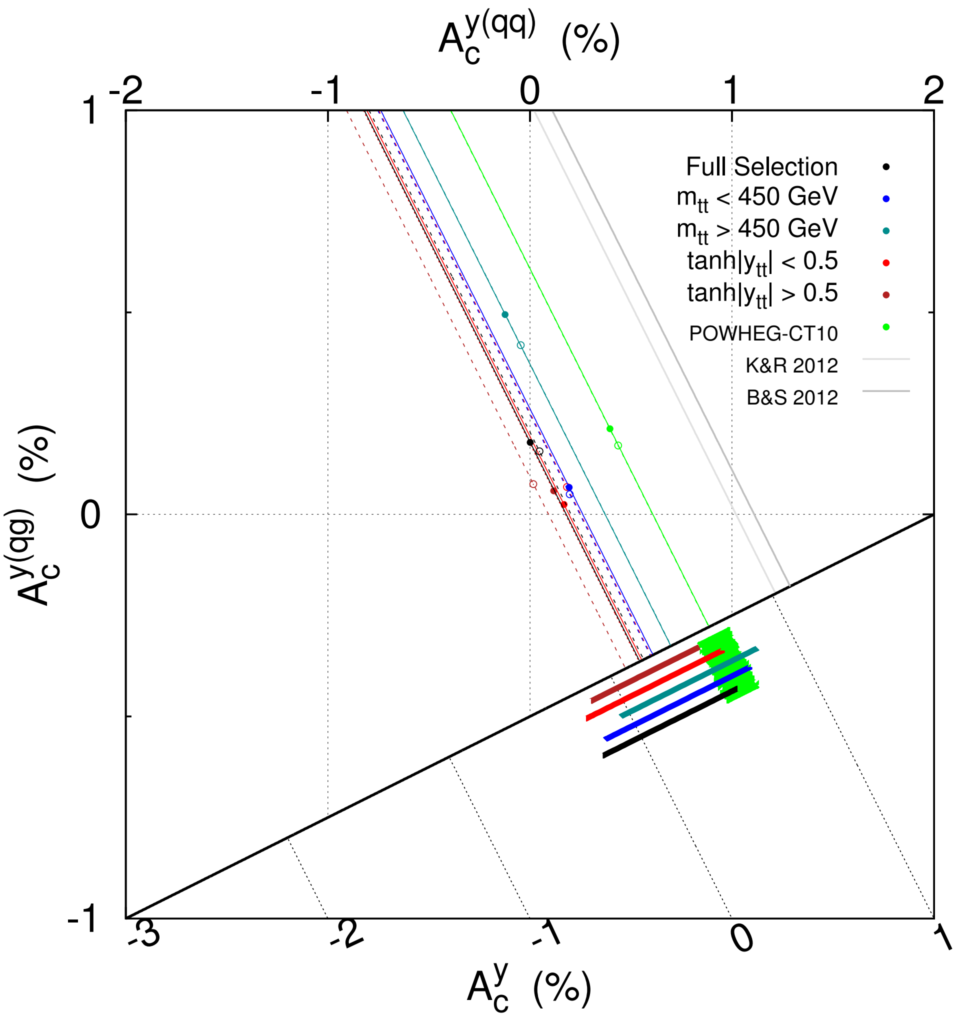

Figure 7.14: Charge asymmetry results under two distinct definitions of $t\bar{t}$ initial states. Filled circles indicate the measured values in the normal 20 GeV/c classification scheme, and open circles indicate the measured values in the 30 GeV/c classification scheme. Lines of constant inclusive asymmetry are drawn through the points to aid the comparison, and the 68% confidence intervals of the 20 GeV/c results are also shown.

7.3 Comparison to Other Measurements

A measurement of the forward-central $t\bar{t}$ charge asymmetry in 8 TeV proton collisions using the unfolding technique has been made public by the CMS collaboration [89], finding $A_c^y = 0.5\% \pm 0.7\%(\text{stat.}) \pm 0.6\%(\text{sys.})$. The result found by the present analysis, using the template method to measure A_c^y on the same data set, is compatible with the CMS unfolding result, but the statistical ($\pm 0.31\%$) and systematic ($\pm 0.29\%$) uncertainties are notably smaller.

Several effects reduce the statistical uncertainty for this analysis. Fifty percent more $t\bar{t}$ events are selected due to looser jet p_T requirements, which reduces the uncertainty with a factor of 0.8. This analysis makes use of a more sensitive background discriminant, reducing uncertainty on sample composition. Since the same discriminant is incorporated into the joint distribution in the measurement, the effective signal purity is comparable or slightly better. In contrast to the $t\bar{t}$ reconstruction presented here, the unfolding analysis does not make use of parton-level jet corrections or adjust jet energies based on kinematic constraints to improve the resolution of the observables. Finally, the template method may be more sensitive than the unfolding method, since it takes as a prior the antisymmetric component of the differential cross section shape.

The manner of evaluating systematic uncertainties in both analyses by observing the shift caused by varying parameters by one standard deviation is likely to result in the overestimation of systematic uncertainties since the statistical uncertainty is significant . The estimation of larger systematic uncertainties for the unfolding analysis may be a reflection of the larger statistical uncertainty.

It is interesting to consider the present forward-central $t\bar{t}$ charge asymmetry results in the context of the Tevatron forward-backward $t\bar{t}$ charge asymmetry measurements [42, 43]. Although the observables are necessarily different for LHC pp collisions and for Tevatron $p\bar{p}$ collisions, and although the parton densities

	(%)	
	$A_c^{y[\mathrm{q\bar{q}}]}$	$A_c^{y[\mathrm{qg}]}$
Powheg ct10	2.96(19)	1.16(11)
Full Selection	0.0(3.3)	1.00(83)
$m_{\mathrm{t\bar{t}}} < 450\,\mathrm{GeV/c^2}$	1.5(3.1)	0.39(89)
$m_{\mathrm{t\bar{t}}} > 450\,\mathrm{GeV/c^2}$	-0.9(2.8)	2.7(1.4)
$\tanh\lvert y_{\mathrm{t\bar{t}}}\rvert < 0.5$	1.3(3.2)	0.11(94)
$\tanh\lvert y_{\mathrm{t\bar{t}}}\rvert > 0.5$	0.9(2.6)	0.33(83)

Table 7.5: Comparison of predicted and measured intrinsic charge asymmetries, based on Table 7.3 and the fractional contributions to the $\mathrm{pp} \to \mathrm{t\bar{t}}$ cross section predicted by Powheg with CT10 parton density functions, listed in Table 4.2.

at the corresponding 8 TeV and 2 TeV collision energies are quite different, the Standard Model processes underlying the respective asymmetries are identical, and occur at an energy scale largely dependent on the same production threshold at twice the top quark mass. Both systems would presumably be affected similarly by new physics. Three effects must be considered.

First, Tevatron $\mathrm{t\bar{t}}$ production occurs predominantly via the $\mathrm{q\bar{q}}$ process [51], while the gg process is dominant at the LHC, and the qg process is also relevant. In principle, the present analysis allows this difference to be controlled by constraining the contributions to the inclusive A_c^y from the $\mathrm{q\bar{q}}$ and qg processes individually. The intrinsic asymmetry from each process can be found by dividing its contribution to the asymmetry by its fractional contribution to the $\mathrm{t\bar{t}}$ production cross section. These fractions have not been measured for the LHC, but as shown in Table 7.2, the predicted values have small systematic uncertainty. Intrinsic $\mathrm{t\bar{t}}$ forward-central charge asymmetries for $\mathrm{q\bar{q}}$ and qg processes, calculated from the measurements and the predicted fractions, are given in Table 7.5.

Second, the forward-central asymmetry is diluted compared to the equivalent forward-backward asymmetry, even for the intrinsic $q\bar{q}$ process. In contrast to $p\bar{p}$ collisions, in which the directional asymmetry of the colliding quark and antiquark is nearly 100%, the momentum asymmetry of the colliding quark and antiquark in pp collisions is just under 50%, rising from zero as a function of absolute $t\bar{t}$ system rapidity. With the Monte Carlo calculation, one can ask what the forward-backward asymmetry would be at the LHC if the quark direction could be ascertained with 100% efficiency; POWHEG indicates an LHC equivalent $q\bar{q} \to t\bar{t}$ forward-backward asymmetry of $\hat{A}_{FB}^{[q\bar{q}]} = 4.794\%$. Since the extended model fixes the shape of the $t\bar{t}$ antisymmetric component of the $q\bar{q} \to t\bar{t}$ differential cross section, values of $A_{FB}^{[q\bar{q}]}$ corresponding to $A_c^{y[q\bar{q}]}$ in Table 7.5 can be found by applying the ratio $\hat{A}_{FB}^{[q\bar{q}]}/\hat{A}_c^{y[q\bar{q}]} \approx 1.6$.

The last effect is the asymmetry dependence on energy scale. The Tevatron and LHC have similar $t\bar{t}$ system invariant mass distributions, both falling rapidly from the production threshold of twice the top quark mass, so the effect can be ignored for a rough comparison.

Considering these three effects, the full selection result for $A_c^{y(q\bar{q})}$ corresponds to an equivalent LHC $q\bar{q} \to t\bar{t}$ forward-backward asymmetry of $A_{FB}^{[q\bar{q}]} = (0.0 \pm 5.3)\%$. The DØ and CDF collaborations have measured A_{FB} equal to $(19.6 \pm 6.5)\%$ and $(15.8 \pm 7.5)\%$, respectively, at the Tevatron. Supposing that the fraction of the $t\bar{t}$ cross section due to $q\bar{q}$ at the Tevatron is about 0.9, the difference between the LHC template measurement and the Tevatron measurements corresponds to 2.4 and 1.8 standard deviations, respectively.

8 Conclusions

The goal of this work is to check whether the significant deviations from Standard Model predictions measured for $\mathrm{t\bar{t}}$ forward-backward asymmetry in $\mathrm{p\bar{p}}$ collisions at the Tevatron are also observed at the Large Hadron Collider in 8 TeV proton-proton collisions. Interest is great because these deviations may be a clue to the mechanism by which matter came to be so much more prevalent in the universe than antimatter. To accomplish this goal, a template technique based on a parametrization of the Standard Model was developed, and used to measure the $\mathrm{t\bar{t}}$ forward-central asymmetry in a lepton+jets selection of pp collision events observed by the CMS experiment in 2012, with $19.6\,\mathrm{fb}^{-1}$ integrated luminosity. Advantages of this new template technique over the unfolding technique used in previous analyses include better sensitivity and the possibility of measuring the contributions to the inclusive asymmetry from distinct $\mathrm{t\bar{t}}$ production processes.

The forward-central $\mathrm{t\bar{t}}$ charge asymmetry was found to be $A_c^y = (0.15 \pm 0.42)\%$, less than but consistent with the Powheg heavy quark generator Standard Model prediction and the CMS measurement using the unfolding technique. The result has a tension of about 2 standard deviations with the larger Standard Model predictions calculated by Kühn & Rodrigo, and by Bernreuther & Si. Of the total measured asymmetry, a contribution $A_c^{y(\mathrm{q\bar{q}})} = (0.00 \pm 0.43)\%$ is attributable to $\mathrm{t\bar{t}}$ production from quark-antiquark annihilation, and a contribution $A_c^{y(\mathrm{qg})} =$

$(0.18 \pm 0.15)\%$ is attributable to $\mathrm{t\bar{t}}$ production from quark-gluon scattering. Measurements on subsets of the data, with $m_{\mathrm{t\bar{t}}}$ greater or less than $450\,\mathrm{GeV/c^2}$, or $\tanh|y_{\mathrm{t\bar{t}}}|$ greater or less than 0.5, are consistent with the main result. The first measurement of the transverse $\mathrm{t\bar{t}}$ charge asymmetry, $A_c^\phi = (0.44 \pm 0.50)\%$, is in good agreement with the Powheg prediction.

By attributing a particular amount of the forward-central $\mathrm{t\bar{t}}$ asymmetry to the process $\mathrm{q\bar{q}} \to \mathrm{t\bar{t}}$, this analysis introduces the possibility of a more direct comparison between Tevatron and LHC results than was previously possible. The rough comparison made in Section 7.3, based on predictions of the relative cross section of $\mathrm{q\bar{q}} \to \mathrm{t\bar{t}}$ and of the correspondence between forward-backward asymmetry and forward-central asymmetry, demonstrates that LHC measurements are already competitive in sensitivity to those of the Tevatron. Work remains to measure the relative cross sections of the processes contributing to $\mathrm{t\bar{t}}$ production, and to understand and reduce systematic uncertainties associated with the comparison.

The sensitivity of this analysis is still statistically limited, and the principle source of systematic uncertainty is insufficient simulation statistics. Significant reductions in uncertainty can be expected, first with the incorporation of more simulation statistics, and in the coming years with the availability of higher luminosity LHC data sets. In the meantime, it will be interesting to investigate the response of the template method to pseudo-data from simulations of Standard Model extensions like chiral color, which could explain the large asymmetry observed at the Tevatron. Beyond these improvements to the present analysis, other analyses involving top quarks may benefit by adopting the novel techniques developed for top quark reconstruction and background discrimination.

The progress of science relies on the interplay between advances in theoretical understanding and advances in experimental techniques. The author hopes that the measurements presented in this work will guide the former, and that the analysis methods will contribute to the latter.

Bibliography

[1] J. Mehra and H. Rechenberg. *The Historical Development of Quantum Theory*. English. 6 vols. New York: Springer, 2001.

[2] L.M. Brown and L. Hoddeson. *The Birth of Particle Physics*. Cambridge University Press, 1986. ISBN: 9780521338370.

[3] L.M. Brown, M. Dresden, and L. Hoddeson. *Pions to Quarks: Particle Physics in the 1950s*. Cambridge University Press, 2009. ISBN: 9780521100731.

[4] L. Hoddeson et al. *The Rise of the Standard Model: A History of Particle Physics from 1964 to 1979*. Cambridge University Press, 1997. ISBN: 9780521578165.

[5] C. N. Yang and R. L. Mills. "Conservation of Isotopic Spin and Isotopic Gauge Invariance". In: *Phys. Rev.* 96 (1 1954), pp. 191–195. DOI: `10.1103/PhysRev.96.191`.

[6] Murray Gell-Mann. "A Schematic Model of Baryons and Mesons". In: *Phys.Lett.* 8 (1964), pp. 214–215. DOI: `10.1016/S0031-9163(64)92001-3`.

[7] Susumu Okubo. "Note on unitary symmetry in strong interactions". In: *Prog.Theor.Phys.* 27 (1962), pp. 949–966. DOI: `10.1143/PTP.27.949`.

[8] V. E. Barnes et al. "Observation of a Hyperon with Strangeness Minus Three". In: *Phys. Rev. Lett.* 12 (8 1964), pp. 204–206. DOI: `10.1103/PhysRevLett.12.204`.

[9] D.J. Gross and Frank Wilczek. “Ultraviolet Behavior of Nonabelian Gauge Theories”. In: *Phys.Rev.Lett.* 30 (1973), pp. 1343–1346. DOI: 10.1103/PhysRevLett.30.1343.

[10] D.J. Gross and Frank Wilczek. “Asymptotically Free Gauge Theories. 1”. In: *Phys.Rev.* D8 (1973), pp. 3633–3652. DOI: 10.1103/PhysRevD.8.3633.

[11] H. David Politzer. “Reliable Perturbative Results for Strong Interactions?” In: *Phys.Rev.Lett.* 30 (1973), pp. 1346–1349. DOI: 10.1103/PhysRevLett.30.1346.

[12] H. Fritzsch, Murray Gell-Mann, and H. Leutwyler. “Advantages of the Color Octet Gluon Picture”. In: *Phys.Lett.* B47 (1973), pp. 365–368. DOI: 10.1016/0370-2693(73)90625-4.

[13] H. David Politzer. “Asymptotic Freedom: An Approach to Strong Interactions”. In: *Phys.Rept.* 14 (1974), pp. 129–180. DOI: 10.1016/0370-1573(74)90014-3.

[14] F. Englert and R. Brout. “Broken Symmetry and the Mass of Gauge Vector Mesons”. In: *Phys. Rev. Lett.* 13 (9 1964), pp. 321–323. DOI: 10.1103/PhysRevLett.13.321.

[15] Peter W. Higgs. “Broken Symmetries and the Masses of Gauge Bosons”. In: *Phys. Rev. Lett.* 13 (16 1964), pp. 508–509. DOI: 10.1103/PhysRevLett.13.508.

[16] G. S. Guralnik, C. R. Hagen, and T. W. B. Kibble. “Global Conservation Laws and Massless Particles”. In: *Phys. Rev. Lett.* 13 (20 1964), pp. 585–587. DOI: 10.1103/PhysRevLett.13.585.

[17] Steven Weinberg. “A Model of Leptons”. In: *Phys.Rev.Lett.* 19 (1967), pp. 1264–1266. DOI: 10.1103/PhysRevLett.19.1264.

[18] Abdus Salam. “Weak and Electromagnetic Interactions”. In: *Conf.Proc.* C680519 (1968), pp. 367–377.

[19] S.L. Glashow. “Partial Symmetries of Weak Interactions”. In: *Nucl.Phys.* 22 (1961), pp. 579–588. DOI: 10.1016/0029-5582(61)90469-2.

[20] G. Arnison et al. “Experimental Observation of Isolated Large Transverse Energy Electrons with Associated Missing Energy at s**(1/2) = 540-GeV”. In: *Phys.Lett.* B122 (1983), pp. 103–116. DOI: 10.1016/0370-2693(83)91177-2.

[21] G. Arnison et al. “Experimental Observation of Lepton Pairs of Invariant Mass Around 95-GeV/c**2 at the CERN SPS Collider”. In: *Phys.Lett.* B126 (1983), pp. 398–410. DOI: 10.1016/0370-2693(83)90188-0.

[22] S.W. Herb et al. “Observation of a Dimuon Resonance at 9.5-GeV in 400-GeV Proton-Nucleus Collisions”. In: *Phys.Rev.Lett.* 39 (1977), pp. 252–255. DOI: 10.1103/PhysRevLett.39.252.

[23] S. Abachi et al. “Observation of the top quark”. In: *Phys.Rev.Lett.* 74 (1995), pp. 2632–2637. DOI: 10.1103/PhysRevLett.74.2632. arXiv: hep-ex/9503003 [hep-ex].

[24] F. Abe et al. “Observation of top quark production in $\bar{p}p$ collisions”. In: *Phys.Rev.Lett.* 74 (1995), pp. 2626–2631. DOI: 10.1103/PhysRevLett.74.2626. arXiv: hep-ex/9503002 [hep-ex].

[25] M.Z. Akrawy et al. “A Direct measurement of the Z0 invisible width by single photon counting”. In: *Z.Phys.* C50 (1991), pp. 373–384. DOI: 10.1007/BF01551449.

[26] D. Buskulic et al. “A Direct measurement of the invisible width of the Z from single photon counting”. In: *Phys.Lett.* B313 (1993), pp. 520–534. DOI: 10.1016/0370-2693(93)90027-F.

[27] Serguei Chatrchyan et al. “Observation of a new boson at a mass of 125 GeV with the CMS experiment at the LHC”. In: *Phys.Lett.* B716 (2012),

pp. 30–61. DOI: 10.1016/j.physletb.2012.08.021. arXiv: 1207.7235 [hep-ex].

[28] Georges Aad et al. "Observation of a new particle in the search for the Standard Model Higgs boson with the ATLAS detector at the LHC". In: *Phys.Lett.* B716 (2012), pp. 1–29. DOI: 10.1016/j.physletb.2012.08.020. arXiv: 1207.7214 [hep-ex].

[29] Hans Dehmelt. "A Single Atomic Particle Forever Floating at Rest in Free Space: New Value for Electron Radius". In: *Physica Scripta* 1988.T22 (1988), p. 102. URL: http://stacks.iop.org/1402-4896/1988/i=T22/a=016.

[30] J. Beringer et al. "Review of Particle Physics (RPP)". In: *Phys.Rev.* D86 (2012), p. 010001. DOI: 10.1103/PhysRevD.86.010001.

[31] Y. Fukuda et al. "Evidence for oscillation of atmospheric neutrinos". In: *Phys.Rev.Lett.* 81 (1998), pp. 1562–1567. DOI: 10.1103/PhysRevLett.81.1562. arXiv: hep-ex/9807003 [hep-ex].

[32] K. Eguchi et al. "First results from KamLAND: Evidence for reactor anti-neutrino disappearance". In: *Phys.Rev.Lett.* 90 (2003), p. 021802. DOI: 10.1103/PhysRevLett.90.021802. arXiv: hep-ex/0212021 [hep-ex].

[33] Q.R. Ahmad et al. "Direct evidence for neutrino flavor transformation from neutral current interactions in the Sudbury Neutrino Observatory". In: *Phys.Rev.Lett.* 89 (2002), p. 011301. DOI: 10.1103/PhysRevLett.89.011301. arXiv: nucl-ex/0204008 [nucl-ex].

[34] Antonio Pich. "The Standard model of electroweak interactions". In: (2007). arXiv: 0705.4264 [hep-ph].

[35] R. P. Feynman. "Space-Time Approach to Non-Relativistic Quantum Mechanics". In: *Rev. Mod. Phys.* 20 (2 1948), pp. 367–387. DOI: 10.1103/RevModPhys.20.367.

[36] M. Srednicki. *Quantum Field Theory*. Cambridge University Press, 2007. ISBN: 9780521864497.

[37] D.H. Perkins. *Introduction to High Energy Physics*. Cambridge University Press, 2000. ISBN: 9780521621960.

[38] F. Halzen and A.D. Martin. *Quarks & Leptons: An Introductory Course In Modern Particle Physics*. Wiley India Pvt. Limited, 2008. ISBN: 9788126516568.

[39] Nicholas Metropolis and S. Ulam. "The Monte Carlo Method". In: *Journal of the American Statistical Association* 44.247 (1949), pp. 335–341. DOI: 10.1080/01621459.1949.10483310.

[40] Makoto Kobayashi and Toshihide Maskawa. "CP Violation in the Renormalizable Theory of Weak Interaction". In: *Prog.Theor.Phys.* 49 (1973), pp. 652–657. DOI: 10.1143/PTP.49.652.

[41] Andreas Hocker and Zoltan Ligeti. "CP violation and the CKM matrix". In: *Ann.Rev.Nucl.Part.Sci.* 56 (2006), pp. 501–567. DOI: 10.1146/annurev.nucl.56.080805.140456. arXiv: hep-ph/0605217 [hep-ph].

[42] V. M. Abazov et al. "Forward-backward asymmetry in top quark-antiquark production". In: *Phys.Rev.* D84 (2011), p. 112005. DOI: 10.1103/PhysRevD.84.112005. arXiv: 1107.4995 [hep-ex].

[43] T. Aaltonen et al. "Evidence for a Mass Dependent Forward-Backward Asymmetry in Top Quark Pair Production". In: *Phys.Rev.* D83 (2011), p. 112003. DOI: 10.1103/PhysRevD.83.112003. arXiv: 1101.0034 [hep-ex].

[44] R.K. Ellis and J.C. Sexton. "Explicit formulae for heavy flavour production". In: *Nuclear Physics B* 282.0 (1987), pp. 642 –652. ISSN: 0550-3213. DOI: http://dx.doi.org/10.1016/0550-3213(87)90702-4.

[45] Leandro G. Almeida, George F. Sterman, and Werner Vogelsang. "Threshold Resummation for the Top Quark Charge Asymmetry". In: *Phys.Rev.* D78 (2008), p. 014008. DOI: 10.1103/PhysRevD.78.014008. arXiv: 0805.1885 [hep-ph].

[46] Nikolaos Kidonakis. "The top quark rapidity distribution and forward-backward asymmetry". In: *Phys.Rev.* D84 (2011), p. 011504. DOI: 10.1103/PhysRevD.84.011504. arXiv: 1105.5167 [hep-ph].

[47] Stanley J. Brodsky and Xing-Gang Wu. "Application of the Principle of Maximum Conformality to the Top-Quark Forward-Backward Asymmetry at the Tevatron". In: *Phys.Rev.* D85 (2012), p. 114040. DOI: 10.1103/PhysRevD.85.114040. arXiv: 1205.1232 [hep-ph].

[48] Peter Skands, Bryan Webber, and Jan Winter. "QCD Coherence and the Top Quark Asymmetry". In: *JHEP* 1207 (2012), p. 151. DOI: 10.1007/JHEP07(2012)151. arXiv: 1205.1466 [hep-ph].

[49] Jan Winter, Peter Z. Skands, and Bryan R. Webber. "Monte Carlo event generators and the top quark forward–backward asymmetry". In: *EPJ Web Conf.* 49 (2013), p. 17001. DOI: 10.1051/epjconf/20134917001. arXiv: 1302.3164 [hep-ph].

[50] J. H. Kuhn and G. Rodrigo. "Charge asymmetry of heavy quarks at hadron colliders". In: *Phys.Rev.* D59 (1999), p. 054017. DOI: 10.1103/PhysRevD.59.054017. arXiv: hep-ph/9807420 [hep-ph].

[51] T. Aaltonen et al. "Measurement of the fraction of $t\bar{t}$ production via gluon-gluon fusion in $p\bar{p}$ collisions at $\sqrt{s} = 1.96$-TeV". In: *Phys.Rev.* D79 (2009), p. 031101. DOI: 10.1103/PhysRevD.79.031101. arXiv: 0807.4262 [hep-ex].

[52] S. Chatrchyan et. al. "Measurement of the charge asymmetry in top-quark pair production in proton-proton collisions at $\sqrt{s} = 7\,\mathrm{TeV}$". In: *Physics*

Letters B 709.1-2 (2012), pp. 28 –49. ISSN: 0370-2693. DOI: http://dx.doi.org/10.1016/j.physletb.2012.01.078.

[53] S. Chatrchyan et. al. "Inclusive and differential measurements of the charge asymmetry in proton-proton collisions at $\sqrt{s} = 7\,\text{TeV}$". In: *Physics Letters B* 717.1-3 (2012), pp. 129 –150. ISSN: 0370-2693. DOI: http://dx.doi.org/10.1016/j.physletb.2012.09.028.

[54] G. Aad et al. "Measurement of the charge asymmetry in top quark pair production in pp collisions at $\sqrt{s} = 7$ TeV using the ATLAS detector". English. In: *The European Physical Journal C* 72.6 (2012), pp. 1–27. ISSN: 1434-6044. DOI: 10.1140/epjc/s10052-012-2039-5.

[55] J. H. Kuhn and G. Rodrigo. "Charge asymmetries of top quarks at hadron colliders revisited". In: *JHEP* 1201 (2012), p. 063. DOI: 10.1007/JHEP01(2012)063. arXiv: 1109.6830 [hep-ph].

[56] Werner Bernreuther and Zong-Guo Si. "Top quark and leptonic charge asymmetries for the Tevatron and LHC". In: *Phys. Rev. D* 86 (3 2012), p. 034026. DOI: 10.1103/PhysRevD.86.034026.

[57] Paul H. Frampton and Sheldon L. Glashow. "Chiral color: An alternative to the standard model". In: *Physics Letters B* 190.12 (1987), pp. 157 –161. ISSN: 0370-2693. DOI: http://dx.doi.org/10.1016/0370-2693(87)90859-8.

[58] Vardan Khachatryan et al. "Search for Dijet Resonances in 7 TeV pp Collisions at CMS". In: *Phys.Rev.Lett.* 105 (2010), p. 211801. DOI: 10.1103/PhysRevLett.105.211801, 10.1103/PhysRevLett.106.029902. arXiv: 1010.0203 [hep-ex].

[59] Georges Aad et al. "Search for Massive Colored Scalars in Four-Jet Final States in $\sqrt{s} = 7$ TeV proton-proton collisions with the ATLAS Detector". In: *Eur.Phys.J.* C71 (2011), p. 1828. DOI: 10.1140/epjc/s10052-011-1828-6. arXiv: 1110.2693 [hep-ex].

[60] Georges Aad et al. “Search for pair-produced massive coloured scalars in four-jet final states with the ATLAS detector in proton-proton collisions at $\sqrt{s} = 7$ TeV”. In: *Eur.Phys.J.* C73 (2013), p. 2263. DOI: 10.1140/epjc/s10052-012-2263-z. arXiv: 1210.4826 [hep-ex].

[61] Serguei Chatrchyan et al. “Search for pair-produced dijet resonances in four-jet final states in pp collisions at $\sqrt{s} = 7$ TeV”. In: *Phys.Rev.Lett.* 110 (2013), p. 141802. DOI: 10.1103/PhysRevLett.110.141802. arXiv: 1302.0531 [hep-ex].

[62] Ulrich Haisch and Susanne Westhoff. “Massive Color-Octet Bosons: Bounds on Effects in Top-Quark Pair Production”. In: *JHEP* 1108 (2011), p. 088. DOI: 10.1007/JHEP08(2011)088. arXiv: 1106.0529 [hep-ph].

[63] Christian Gross et al. “Light axigluon explanation of the Tevatron ttbar asymmetry and multijet signals at the LHC”. In: *Phys.Rev.* D87 (2013), p. 014004. DOI: 10.1103/PhysRevD.87.014004. arXiv: 1209.6375 [hep-ph].

[64] Lyndon Evans and Philip Bryant. “LHC Machine”. In: *JINST* 3 (2008). Ed. by Lyndon Evans, S08001. DOI: 10.1088/1748-0221/3/08/S08001.

[65] Serguei Chatrchyan et al. “Search for Supersymmetry at the LHC in Events with Jets and Missing Transverse Energy”. In: *Phys.Rev.Lett.* 107 (2011), p. 221804. DOI: 10.1103/PhysRevLett.107.221804. arXiv: 1109.2352 [hep-ex].

[66] Vardan Khachatryan et al. “Search for Supersymmetry in pp Collisions at 7 TeV in Events with Jets and Missing Transverse Energy”. In: *Phys.Lett.* B698 (2011), pp. 196–218. DOI: 10.1016/j.physletb.2011.03.021. arXiv: 1101.1628 [hep-ex].

[67] S Chatrchyan et al. “The CMS experiment at the CERN LHC. The Compact Muon Solenoid experiment”. In: *J. Instrum.* 3 (2008). Also published by CERN Geneva in 2010, S08004. 361 p.

[68] Torbjörn Sjöstrand, Stephen Mrenna, and Peter Skands. "PYTHIA 6.4 physics and manual". In: *JHEP* 05 (2006), p. 026. DOI: 10.1088/1126-6708/2006/05/026. arXiv: hep-ph/0603175 [hep-ph].

[69] Torbjorn Sjöstrand, Stephen Mrenna, and Peter Z. Skands. "A Brief Introduction to PYTHIA 8.1". In: *Comput.Phys.Commun.* 178 (2008), pp. 852–867. DOI: 10.1016/j.cpc.2008.01.036. arXiv: 0710.3820 [hep-ph].

[70] R. Corke and T. Sjostrand. "Improved Parton Showers at Large Transverse Momenta". In: *Eur.Phys.J.* C69 (2010), pp. 1–18. DOI: 10.1140/epjc/s10052-010-1409-0. arXiv: 1003.2384 [hep-ph].

[71] S. Agostinelli et al. "GEANT4: A Simulation toolkit". In: *Nucl.Instrum.Meth.* A506 (2003), pp. 250–303. DOI: 10.1016/S0168-9002(03)01368-8.

[72] Stefano Frixione, Paolo Nason, and Giovanni Ridolfi. "A Positive-weight next-to-leading-order Monte Carlo for heavy flavour hadroproduction". In: *JHEP* 0709 (2007), p. 126. DOI: 10.1088/1126-6708/2007/09/126. arXiv: 0707.3088 [hep-ph].

[73] Hung-Liang Lai et al. "New parton distributions for collider physics". In: *Phys.Rev.* D82 (2010), p. 074024. DOI: 10.1103/PhysRevD.82.074024. arXiv: 1007.2241 [hep-ph].

[74] J. Alwall et al. "MadGraph 5 : Going Beyond". In: *JHEP* 1106 (2011), p. 128. DOI: 10.1007/JHEP06(2011)128. arXiv: 1106.0522 [hep-ph].

[75] Simone Alioli et al. "NLO single-top production matched with shower in POWHEG: s- and t-channel contributions". In: *JHEP* 0909 (2009), p. 111. DOI: 10.1007/JHEP02(2010)011, 10.1088/1126-6708/2009/09/111. arXiv: 0907.4076 [hep-ph].

[76] Emanuele Re. "Single-top Wt-channel production matched with parton showers using the POWHEG method". In: *Eur.Phys.J.* C71 (2011), p. 1547. DOI: 10.1140/epjc/s10052-011-1547-z. arXiv: 1009.2450 [hep-ph].

[77] *Particle-Flow Event Reconstruction in CMS and Performance for Jets, Taus, and MET*. Tech. rep. CMS-PAS-PFT-09-001. 2009. Geneva: CERN, 2009.

[78] *Commissioning of the Particle-flow Event Reconstruction with the first LHC collisions recorded in the CMS detector*. Tech. rep. CMS-PAS-PFT-10-001. 2010.

[79] Matteo Cacciari, Gavin P. Salam, and Gregory Soyez. "The anti-k_t jet clustering algorithm". In: *JHEP* 04 (2008), p. 063. DOI: 10.1088/1126-6708/2008/04/063. arXiv: 0802.1189 [hep-ex].

[80] The CMS collaboration. "Determination of jet energy calibration and transverse momentum resolution in CMS". In: *Journal of Instrumentation* 6.11 (2011), P11002. URL: http://stacks.iop.org/1748-0221/6/i=11/a=P11002.

[81] The CMS collaboration). "Determination of the Jet Energy Scale in CMS". In: *Journal of Physics: Conference Series* 404.1 (2012), p. 012013. URL: http://stacks.iop.org/1742-6596/404/i=1/a=012013.

[82] The CMS collaboration. "Identification of b-quark jets with the CMS experiment". In: *Journal of Instrumentation* 8.04 (2013), P04013. URL: http://stacks.iop.org/1748-0221/8/i=04/a=P04013.

[83] Burton A. Betchart, Regina Demina, and Amnon Harel. "Analytic solutions for neutrino momenta in decay of top quarks". In: *Nucl.Instrum.Meth* 736.0 (2014), pp. 169 –178. ISSN: 0168-9002. DOI: 10.1016/j.nima.2013.10.039.

[84] N. E. Day and D. F. Kerridge. "A General Maximum Likelihood Discriminant". English. In: *Biometrics* 23.2 (1967), pp. 313–323. ISSN: 0006341X. URL: http://www.jstor.org/stable/2528164.

[85] Wouter Verkerke and David P. Kirkby. "The RooFit toolkit for data modeling". In: *eConf* C0303241 (2003), MOLT007. arXiv: physics/0306116 [physics].

[86] Nikolaos Kidonakis. “Differential and total cross sections for top pair and single top production”. In: (2012), pp. 831–834. DOI: 10.3204/DESY-PROC-2012-02/251. arXiv: 1205.3453 [hep-ph].

[87] Ryan Gavin et al. “FEWZ 2.0: A code for hadronic Z production at next-to-next-to-leading order”. In: *Comput.Phys.Commun.* 182 (2011), pp. 2388–2403. DOI: 10.1016/j.cpc.2011.06.008. arXiv: 1011.3540 [hep-ph].

[88] Michiel Botje et al. “The PDF4LHC Working Group Interim Recommendations”. In: (2011). arXiv: 1101.0538 [hep-ph].

[89] *Measurement of the ttbar charge asymmetry with lepton+jets events at 8 TeV*. Tech. rep. CMS-PAS-TOP-12-033. Geneva: CERN, 2013. URL: https://cds.cern.ch/record/1600839.